Modelling Peak Shifts not Resulting from Lattice Strain in Anisotropic and Inhomogeneous Materials using Monte-Carlo Simulation of Neutron Diffraction

Thesis

Modelling Peak Shifts not Resulting from Lattice Strain in Anisotropic and Inhomogeneous Materials using Monte-Carlo Simulation of Neutron Diffraction

John Brokx

B.Sc.(Hons), M.Sc

A thesis submitted for the degree of Doctor of Philosophy

September 2019

School of Engineering and Innovation

The Open University

Milton Keynes

MK7 6AA

United Kingdom

Abstract

Neutron diffraction has been used by the nuclear industry for measuring residual stresses in structures for which integrity safety cases must be made. However measurement of stresses in materials containing large grains, or in anisotropic weld metal, or approaching air-metal interfaces, or metal-metal interfaces using neutron diffraction is particularly challenging. These types of measurements can give rise to errors (often termed “pseudo-strains”) that can be significantly larger than the residual stress actually present. Such errors arise when the gauge volume is partially filled (e.g. air to metal interface for measuring near-surface stresses), or when the gauge volume composition is inhomogeneous (metal to metal interface), or the gauge volume material is anisotropic (welds with bundles of elongated grains). To mitigate such errors several approaches have been proposed using numerical and analytical methods to calculate the magnitude of pseudo-strain. Whether these methods can be applied depends on the instrument used and the type of sample being measured. In this context a different approach based on the Monte-Carlo method, as embedded in the neutron ray tracing software package McStas is proposed.

The aim is to validate by neutron measurements the ability of McStas to simulate pseudo strains associated with a gauge volume that is partially filled, or a gauge volume that samples inhomogeneous and anisotropic material. The instrument modelled for this research project is ENGINX a time-of-flight instrument located at ISIS (RAL). To understand and isolate the effects of traversing an interface made up of different materials a stepwise approach was taken. The initial phase involved building a new model of ENGINX in McStas and to validate its correctness by analysing the characteristics of the beam and gauge volume by simulating a steel pin scan. The subsequent phase focussed on virtual experiments to study the pseudo strain arising when measuring strain in an air-to-material interface, a material-to-material interface and when large grains or pores are present as in the vicinity of welds. The results presented are not intended to be used as a quantitative prediction of pseudo strain but to demonstrate how McStas can be used to model virtual experiments to study the pseudo strains occurring. Several virtual sample models have been built to demonstrate how this could be useful/interesting for beamline scientists and users of neutron diffraction. One such virtual sample model is used to demonstrate that the mitigation technique of rotating the sample 180° works when the detector is in transmission but not in reflection, and that it is strongly dependent on the attenuation of the investigated material. Another virtual sample model is used to demonstrate that when the ratio of a cavity (hole, pore, etc) to the gauge volume is more than 2%, then significant pseudo strains can arise. Moreover, this work delivers a new model for ENGINX.

Acknowledgement

I like to thank Dr. Richard Moat(OU), Dr. Joe Kelleher(ISIS), Prof. John Bouchard(OU), Prof. Bill Nuttall(OU) and Dr. Jon James(OU) for their guidance, support and encouragement.

A special thanks to Mushfiq Rahman who was the lead researcher in the experiments I attended and for the use of the experimental data in my thesis. I also like to take this opportunity to thank Joe Kelleher and Saurabh Kabra for their assistance with the experiments done at ISIS(RAL).

Many thanks to all the PhD researchers, post docs and staff of the OU Materials Engineering department for their kind support.

1. Contents

List of Figures

List of Tables

List of Abbreviations

TOF	Time of flight
RC	Radial Collimator
IGV	Instrument Gauge Volume
SGV	Sample Gauge Volume
RAL	Rutherford Appleton Laboratories
PSD	Position Sensitive Detector
NPP	Nuclear Power Plant
NCOG	Neutron Weight Centre Of Gravity
HPC	High Performance Computer
CIF	Crystallographic Information File
ICSD	Inorganic Crystallographic Structures Database
ILL	Institut Laue Langevin
DMW	Dissimilar Metal Weld

Nomenclature

hkl	Miller indices
λ	Neutron wavelength
h	Planck's constant
v	Velocity of neutron
a_0	Lattice parameter constant for strain free sample
d^0_{hkl}	Lattice plane spacing in strain free sample
d_{hkl}	Lattice plane spacing in a strained sample
ϑ^0_{hkl}	Scattering angle strain free sample
ϑ_{hkl}	Scattering angle strained sample
τ^0_{hkl}	Time-of-flight for strain free sample
τ_{hkl}	Time-of-flight for strained sample
ε^0_{hkl}	Strain for lattice plane in hkl direction, strain free sample
ε_{hkl}	Strain for lattice plane in hkl direction, strained

1 Introduction

In the UK[1] about 20% of the electricity in 2018 was generated using nuclear power plants. Many existing nuclear power plants are reaching the end of economic life and will be shut down in the next 10 to 15 years. As part of the overall energy policy[2]the UK government has decided to keep nuclear energy as a strategic source in the energy mix. This means that the existing nuclear power plants will need to be replaced with new ones. The plants to be built in the next 20 years are most likely to be based on improved designs of proven technology, such as the Pressurized Water Reactor (PWR) and the Boiling Water Reactor (BWR). Recently the UK government gave the go ahead for the build of a new nuclear power plant at HinckleyC[3]. This plant will be based on the European Pressurized Water Reactor, a design from EDF/AREVA a schematic of this reactor is shown in Figure 1.1. This reactor is an evolutionary design[4], [5][6] based on existing PWRs currently operational in Germany and France. The focus of the EPR design has been on safety aspects using concepts that do not require human intervention particularly in the event of loss of cooling. In the longer term it is envisaged that new reactor types referred to as generation IV reactors[7] will emerge that can operate at much higher temperatures to improve efficiency and will burn more efficiently the nuclear fuel thereby reducing the radioactive waste over the lifetime of the reactor. To achieve these benefits both new materials as well as enhancement of existing materials used in reactors will be required[8] due to the aggressive operating environment.

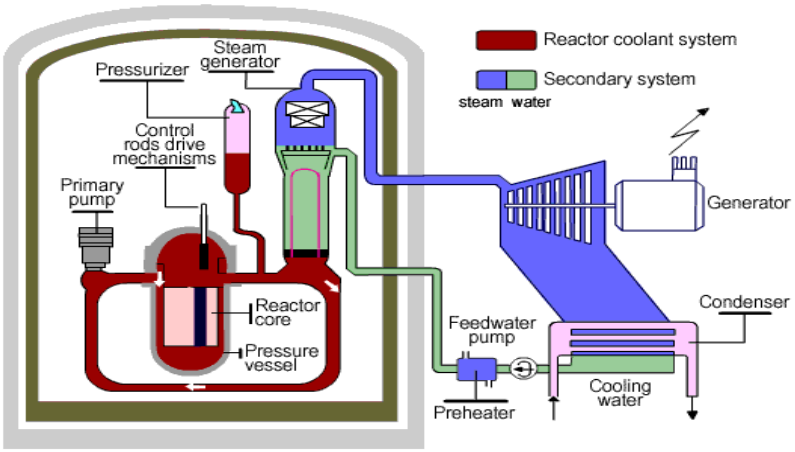

Figure 1.1: Schematic of European Pressurized Water Reactor (Source: Areva-NP)

Both existing and new nuclear power plants consist of many components notwithstanding the drive for simplification. The manufacturing processes used to make these components can lead to a build up of residual stresses in these components which add to any primary stresses present in the system. The economic life of current nuclear power plants is about 40 years and for future plants this is expected to go up to at least 60 years[][9]. This puts a very high demand on the components used.

Over time the residual stresses can lead to an acceleration of fatigue and creep, both weakening the components and resulting in a potential component failure. Safety is one of the most important aspects of designing and building nuclear power plants. It is therefore very important to measure these residual stresses and account for them in lifetime prediction.

The methods to determine the residual stress in a component can be divided in destructive and non-destructive. One of the non-destructive methods is neutron diffraction and improvement of the understanding of this technique forms the basis of this dissertation. Neutron diffraction is an established method in the nuclear industry and in the wider engineering community. Due to the complexity and costs of the infrastructure and instruments used to perform neutron diffraction measurements only a limited number of locations are available globally. The experiments done in the context of this research took place at ISIS (Rutherford Appleton Laboratories) in UK, using a time-of-flight neutron diffraction instrument, ENGINX. Many of the components in a nuclear power plant are joined with other components using welding. The heating and cooling during the welding process are an important source for residual stress and measuring the stress in such a weld using neutron diffraction poses a challenging problem and can result in errors in the strain measured. Of special interest are welds of components made of different materials and the added complexity adds to the difficulties in making reliable measurements. More broadly measurement errors, referred to in the literature as pseudo strains or spurious strains, arise when the gauge volume is not uniformly filled by an isotropic diffracting medium. For instance, measuring strain at air to metal interfaces, at dissimilar metal interfaces and in the vicinity of uncharacteristically large grains, all features that can occur in welds.

The purpose of this research is to validate if Monte-Carlo simulation of neutron diffraction as embedded in McStas[10] a neutron ray tracing software package, can be used to investigate the errors that can arise in certain type of strain measurements that might occur in welds present in nuclear plant and to obtain a better understanding of it. In this thesis the term experiment is used when referring to an experiment using the real physical instrument and the term virtual experiment[11] is used when referring to a simulation in McStas using a virtual model of the instrument. Although the emphasis of this research is on exploring the capabilities and benefits of virtual experiments to simulate strain measurements using neutron diffraction, comparison to data from experiments is done where possible to validate the correctness of the virtual model and the accuracy of the data generated by the simulations. The virtual modelling efforts are divided in three blocks. The first block focusing on the design and build of a virtual model of the ENGIN-X instrument in McStas. To assess the correctness of the model the neutron beam characteristics of the virtual instrument and the ability to predict diffraction peak position are verified. The simulation results are compared against data from

experiments using nominally identical instrument settings. The emphasis in the second block is on how to model samples and more complicated scanning scenarios in McStas, more specifically the modelling of an air-to-material interface and material-to-material interface. Two different virtual models in McStas are presented, one model made use of the powder sample component type, while the other model made use of the union component type. The specifics of these two models can be found in Chapter 2 and 3. To assess the correctness of the sample models the results of the simulations were compared against each other as well as against results from experiments. The samples and scenarios modelled in the second block aimed to give an insight in to what extend McStas can be used to model samples and strain measurement scenarios where the gauge volume is only partially immersed in the sample or is made up of two different materials. The third block presents the design and build of a virtual sample model to study the effect of uncharacteristically large grains, as are present in the vicinity of many welds on the errors in strain. The results of the simulations were compared against the results from experiments done using a physical sample with the same features. In anticipation of future work using virtual modelling techniques several other sample models and scan scenarios have been explored. These are briefly explained to demonstrate what may be possible.

2 General principles

The research performed for this thesis draws on a range of disciplines to a various degree of detail. Without being exhaustive, an attempt is made to provide a comprehensive background in the theory behind the research, work done by others in this field of research and the techniques used to design and build virtual experiments.

2.1 Residual stress

Stresses that exist within a component or assembly in the absence of any external applied load or self-load are called residual stresses[12][13][14]. Residual stress arises from shape misfits between different regions. Misfits in shape can arise from differences in thermal expansion or contraction (as in welds), differences in mechanical properties of different phases (as in composites or alloys) and through the accommodation of local plastic deformation (as in peening)[13]. Residual stress can also arise in engineering components due to interaction between misfitting parts within an assembly. A particular important area in this context is formed by welding because the final residual stress state is often formed as a consequence of the combination of all of the above. When joining two parts using welding large thermal stress gradients build up close to the welded joints due to the localised heating and subsequent cooling of the weld zone. The contraction resulting from these localised temperature variations can cause weld cracking or distortion during welding. This can lead to rejection of the weld for not meeting conformance or reduced service life[14]. Furthermore, the cooling rates experienced during welding can be severe enough to induce phase transformation and local plastic deformation [15][16][17]. Residual stress measurements are therefore important in joining processes like welding because computational modelling of such complex scenarios is very complicated [18][19]–[21]. The measurements help with extending the economic life of components using post weld heat treatments but also because they are integral in validating the finite element process modelling that is used to model new components in order to minimise unwanted residual stress and distortion. Residual stresses can also be beneficial. This could be through generation of compressive residual stresses in a particular region of a component which can increase a component's external resistance to an externally applied load (prestressed concrete) or through peening to extend its service life by retarding the growth of fatigue cracks [22].

2.1.1 Types of residual stresses

Residual stresses can be classified according to the scale over which the forces balance that cause the stress. A classification defined by Macherauch & Kloss[23] distinguishes three different types of residual stress.

Type I residual stresses are homogeneous over a very large number of crystal domains of the material. The internal forces related to this stress are balanced on all planes. The moments related to these forces are equal to zero around all axes.

Residual stresses of type II

Type II residual stresses are homogeneous within small crystal domains of the material (a single grain or phase). The internal forces related to these stresses are in balance between the different grains or phases.

Residual stresses of type III

Type III residual stresses are homogeneous on the smallest crystal domains of the material (over a few interatomic distances). The internal forces coupled to these stresses are in balance in very small domains (such as around dislocations or point defects).

The various types of residual stresses are illustrated in Figure 2.1.

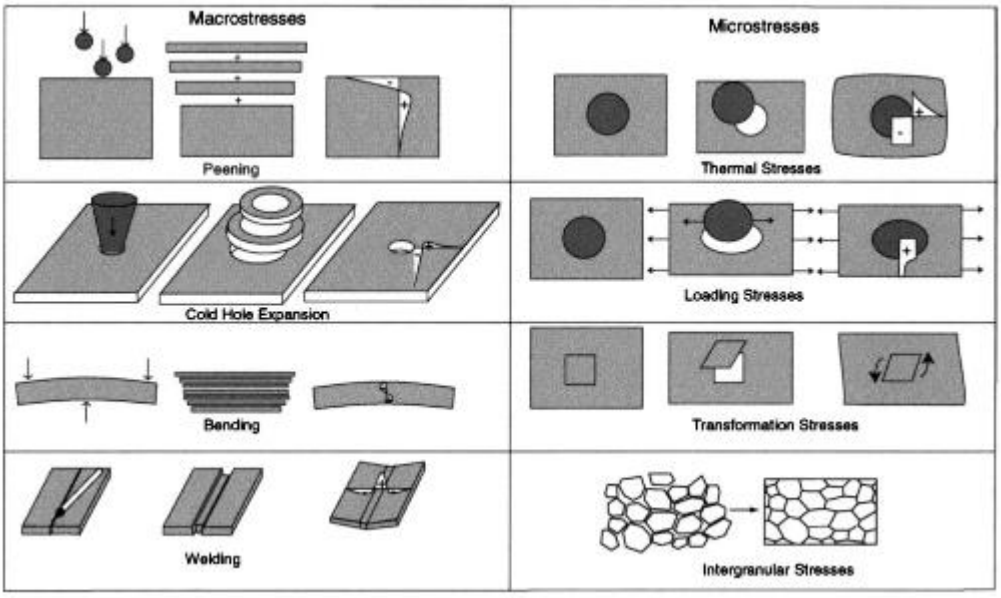

Figure 2.1: Residual stresses are caused by misfits in the material. A number of different types of residual macro- and micro residual stresses are shown[13].

Type I residual stresses are referred to as macro-stresses, while Type II and III stresses are collectively referred to as micro-stresses. In the case of real materials, the actual residual stress state at a point comes from the superposition of all three types of stress. The focus in this research project is predominantly on micro-stresses of type I.

2.1.2 Stress and strain – Hooke's law

In practise the residual stress is arrived at in an indirect manner by first determining the strain and then deriving the stress from the strain using the generalised version of Hooke's law.

If F [N] is the force acting on an area A [m^{-2}] of a component then the residual stress σ [MPa] can be expressed as

$$\sigma = F/A \tag{2.1.1}$$

To take this into account a more generalised form of equation (2.1.1) can be given using σ_{ij} ,a second-order tensor representing the mechanical stress state at a point in the component which can be expressed as

$$\sigma_{ij} = \frac{\partial F_i}{\partial A_j} \tag{2.1.2}$$

where F_i represents the component of force in a direction x_i that acts on the element of volume characterized by surface dA_j, whose normal is in the direction x_i.

Primary stress results from an applied external force. Residual stress is the stress that remains once the external force is removed. The resulting displacements can be represented through a strain field. The state of strain of a small element of volume is defined by the second-order tensor ε_{ij}. For small strains the expression can be written as:

$$\varepsilon_{ij} = \frac{1}{2}\left[\frac{\partial u_i}{\partial x_j} + \frac{\partial u_j}{\partial x_i}\right] \tag{2.1.3}$$

In which u is the vector of displacements. Both the stress as well as the strain tensor are symmetrical, that is, $\sigma_{ij} = \sigma_{ji}$ and $\varepsilon_{ij} = \varepsilon_{ji}$. The microscopic relation between the strain and the stress tensor is given by the generalized Hooke's law[24]

$$\varepsilon_{ij} = S_{ijkl}\sigma_{kl} \tag{2.1.4}$$

or by expressing the stress according to the strain as

$$\sigma_{ij} = C_{ijkl}\varepsilon_{kl} \tag{2.1.5}$$

C_{ijkl} and S_{ijkl} are coefficients of compliance and stiffness of the material, respectively. The materials used for this research have a crystal structure that is either body centred cubic (BCC) or face entered cubic (FCC) and are mostly in the form of powder or a polycrystalline sample which can be approximated as a fully dense powder, resulting in only two independent C-coefficients , corresponding with Young's modulus and Poisson's ratio, resp.

2.1.3 Strain measurement

The methods to determine the strain in a component can be divided in destructive and non-destructive. These methods do not measure the strain directly but measure a geometric change of the component that can be used to derive the strain. Destructive methods such as hole drilling [25] take a cut of the component and measure the change in dimensions that result of relaxation. The strain can be calculated from these dimensional changes. Non-destructive methods do not physically alter the component but derive the strain by measuring the lattice spacing of the material and compare this against the lattice spacing in a stress-free sample of the same type of material. The lattice spacing can be determined using diffraction. The vector strain field can then be determined from the lattice spacing. These methods assume that all other physical properties of the sample and the applied load stay the same.

In this dissertation the focus is on neutron diffraction. At no point is any comparison or recommendation made that any method is more suitable than any other for characterising the residual stress in welds. It is apparent from literature that Neutron diffraction is a valuable tool for characterising the residual stress in welds [26]–[28], and even though in some cases other methods may be more appropriate or less susceptible to errors resulting from welding features, improvement in the understanding of where such errors arise in Neutron diffraction is key to quantifying the error in measurements and for designing experiments potentially free from these errors. Therefore, for this point on, the focus will be solely on Neutron diffraction as a means of residual stress characterisation.

2.2 Diffraction

Diffraction has been used by scientists of various disciplines for many years to investigate the structure and composition of materials. The underlying theory how diffraction works uses elements of wave theory and quantum mechanics.

2.2.1 Wave theory

The behaviour of waves was first described by Huygens (1678) [29] when studying waves in water. Huygens principle states that each point on a wave front may be regarded as a source of waves expanding from that point. This principle is illustrated in Figure 2.2 where the wave pattern is shown that arises when a drop of water hits the water surface and how new waves are spreading from points (secondary sources) on preceding waves.

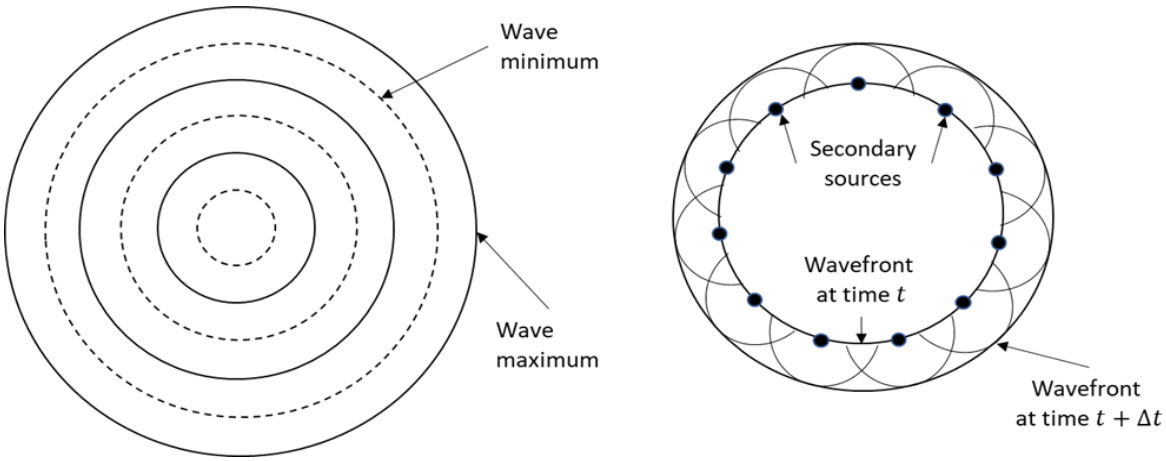

Figure 2.2: Huygen's principle

This principle is not only valid for plane waves in water but also for three dimensional waves like light waves. Huygen 's principle can be used to derive the laws of reflection and refraction for light waves but is not sufficient by itself to explain the wave diffraction pattern that occurs when waves pass through an aperture or around an object as illustrated in Figure 2.3.

Figure 2.3: Diffraction beach

Fresnel[30] provided an explanation of diffraction of light waves using his principle of interference and Huygens principle for waves. Interference occurs when two are more waves overlap each other. The superposition of the waves, results in constructive interference if all the waves have the same wavelength and are in phase and destructive interference when they are out of phase as illustrated in Figure 2.4 . If the waves have a different wavelength and amplitude and/or out of phase the resulting wave may show partial constructive interference.

Figure 2.4: Constructive interference when wavelength is the same and waves are in phase, destructive interference when wavelength is the same and waves are out of phase

Diffraction occurs when a wave passes through an opening or encounters an object provided the wavelength is smaller than the size of the opening or the object. This is illustrated in Figure 2.5 where a plane wave is shown passing through a slit. When the wavelength is much smaller than the slit then the waves pass through the slit unchanged however when the wavelength is of the same magnitude or larger than the slit, then the waves emanating from the slit become circular or spherical in shape and will bend around the corners of the slit.

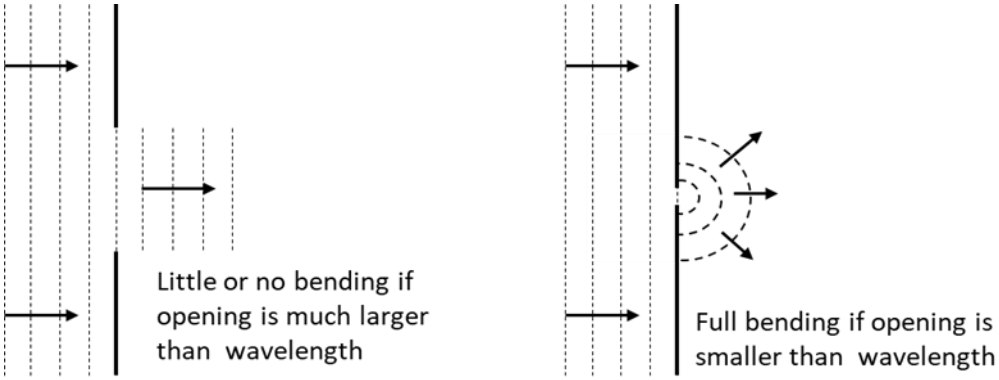

Figure 2.5: Bending of waves passing through an opening only occurs if the wavelength is smaller than the size of the opening

If the slit is replaced with multiple slits then waves will emanate from each slit similar to the case of a single slit but now those waves will interfere with each other. The result of the interference can be made visible by placing a screen behind the slits as is illustrated in Figure 2.6. The dark lines are the result of destructive interference and the light lines are the result of constructive interference. This pattern is referred to as diffraction pattern. If more than one wavelength is used than the pattern will have a similar shape but there will be more dark and light areas with the central area on the screen the brightest.

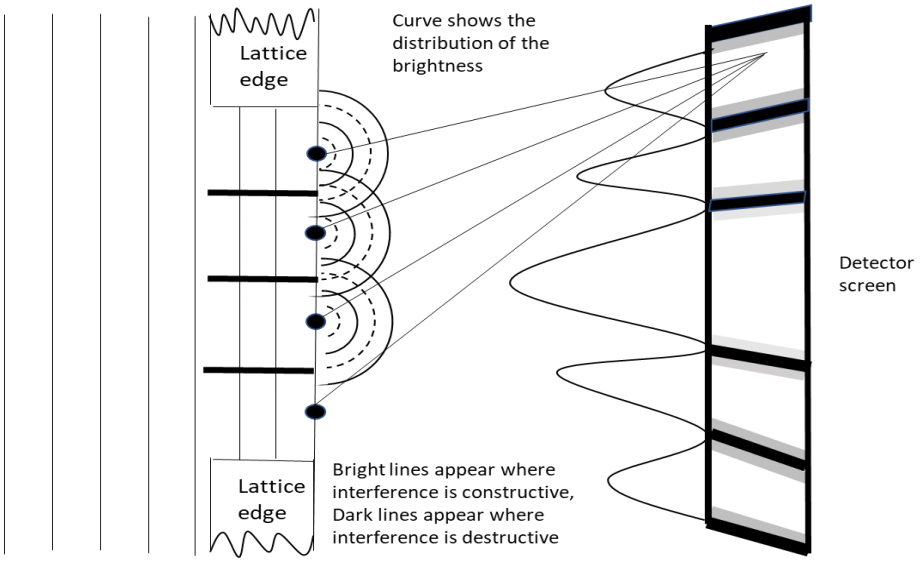

Figure 2.6: Diffraction pattern arising when waves pass through a lattice.

A rigorous mathematical formulation of diffraction based on the wave equation was given by Kirchoff. The Fresnel-Huygens explanation of diffraction appears as the near field limit case in this formulation.

2.2.2 Determination of lattice spacing

The possibility that X-rays might be diffracted by a crystal lattice was proposed by Max von Laue (1912). The wave nature of X-rays was observed by Friedrich and Knipping (1913). This work was extended by Lawrence Bragg (1912). In Bragg's view a material can be considered as being made up of an array of parallel planes referred to as lattice planes. The orientation of a lattice plane is defined by its Miller indices hkl, where (hkl) refers to the lattice plane and $[hkl]$ to the normal direction of the lattice plane. In an ideal crystal structure, each plane contains rows of atoms, distributed in a regular pattern over the plane as shown in Figure 2.7. The structure of an ideal lattice structure repeats itself periodically. The periodicity is defined by the unit cell.

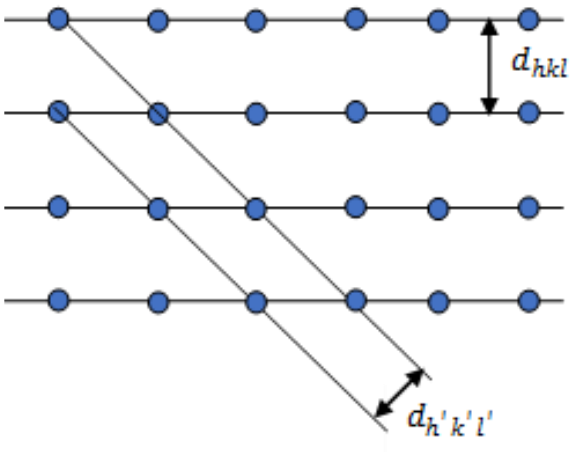

Figure 2.7: Simple crystal lattice structure

The dimensions of the unit cell in a 3-dimensional lattice are defined by the lattice parameters commonly referred to as a, b and c. The magnitude of these lattice parameters is usually different, however in a cubic lattice structure they have the same magnitude. Lattice planes typical for a cubic lattice structure are shown in Figure 2.8.

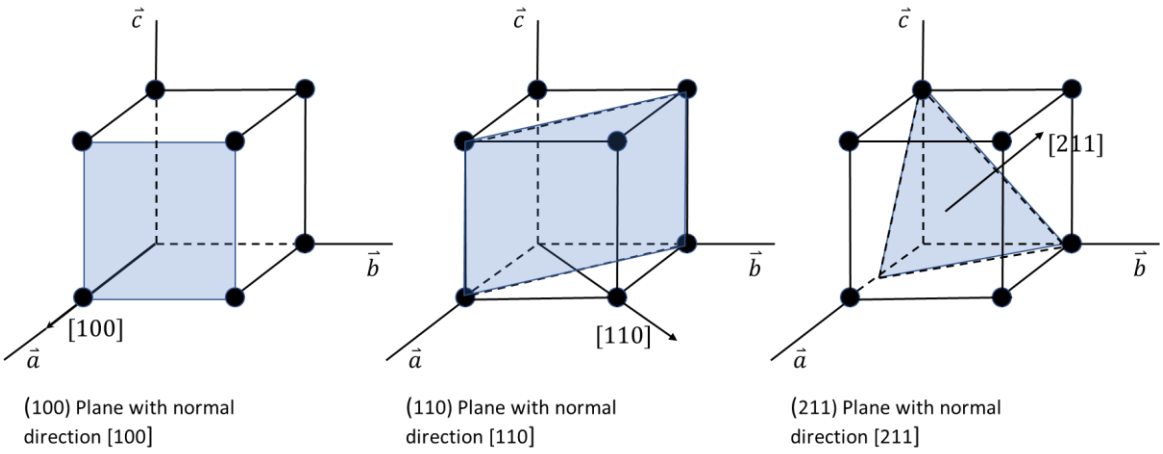

Figure 2.8: Lattice planes typical for a cubic lattice structure.

The lattice spacing $d_{hkl}[\text{Å}]$ is the distance between adjacent planes. For a cubic lattice equation (2.2.1) can be used to derive the lattice spacing d_{hkl} from the lattice parameter. If the magnitude of the lattice parameter is $\|a\|[\text{Å}]$, then the lattice spacing for a plane (hkl) in a cubic lattice is

$$d_{hkl} = \|a\|/\sqrt{h^2 + k^2 + l^2} \tag{2.2.1}$$

The wavelength of the incident wave can be related to the lattice spacing when they meet Bragg's law(reference). Bragg's law requires constructive interference to occur between all the scattered waves. For this to happen the following conditions need to be met:

(1) The incident angle φ of the incoming wave must be equal to the diffraction angle ϑ of the outgoing wave as illustrated in Figure 2.9, this gives a scattering angle of 2ϑ

(2) The difference in the length of path ΔL travelled by waves reflected from adjacent planes as shown Figure 2.10, is

$$\Delta L = 2d \sin\vartheta \tag{2.2.2}$$

(3) For constructive interference to occur between all the outgoing waves this path difference must be a whole number of wavelengths, $\lambda[\text{Å}]$

$$\Delta L = n\lambda \tag{2.2.3}$$

Combining equations (2.2.2) and (2.2.3) gives Bragg's law:

$$n\lambda = 2d \sin\vartheta \tag{2.2.4}$$

The integer n is the order of reflection. The angle ϑ is dependent on the orientation hkl of the plane hence equation (2.2.4) can be written as:

$$n\lambda = 2d_{hkl}\sin\vartheta_{hkl} \tag{2.2.5}$$

Bragg's law assumes the crystal lattice structure is ideal.. A real material will contain impurities, dislocations and interstitials. These need to be comparatively small for the material to be treated as an ideal crystal lattice structure.

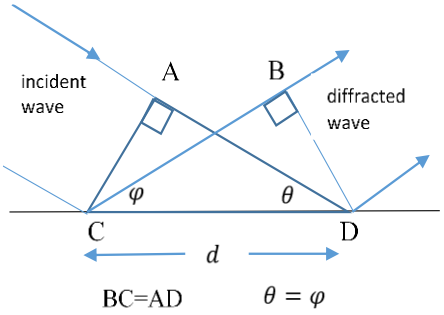

Figure 2.9: Incident wave diffracting from plane with φ≠ϑ

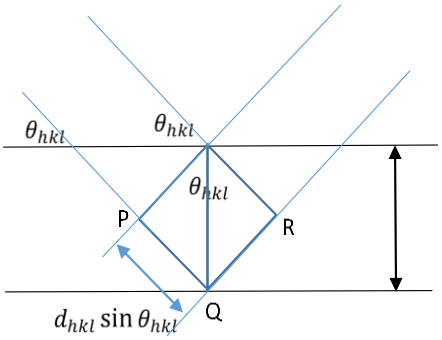

Figure 2.10: Incident wave and diffracted wave with φ=ϑ

For the diffraction experiments described in this thesis only contributions from reflections of order 1 are considered.

2.2.3 Type of waves

X-rays are just one example of waves that can be used for diffraction. There are many other types of waves that can be used for diffraction and in general any type of particle can behave as a wave. This was first postulated by Louis de Broglie (1928) [31]. Based on this the impulse of a particle can be related to its wavelength. The impulse $p[kgm/s]$ of a particle of mass m with a velocity $v[m/s]$ is:

$$p = mv \tag{2.2.6}$$

If the corresponding wavelength for this particle is $\lambda[\text{Å}]$ then the impulse of this wave is:

$$p = h/\lambda \tag{2.2.7}$$

where $h[Js]$ is Planck's constant. Combining equations (2.2.6) and (2.2.7) relates the velocity of the particle to its wavelength:

$$mv = h/\lambda \tag{2.2.8}$$

This means that not only X-rays but also particles like electrons, muons, protons and neutrons can behave as waves and be used for diffraction. What type of waves to use for a particular diffraction measurement depends on the characteristics of the particle.

2.3 Neutrons and neutron diffraction

The nuclei of atoms are made up of protons and neutrons. Neutrons are particles that can behave as waves. To determine what makes neutrons interesting in the context of diffraction it is necessary to understand their characteristics, how neutrons can be obtained and their behaviour when penetrating matter.

2.3.1 Characteristics

Neutrons have no charge and hence there is no electrostatic interaction with charged particles like electrons in atoms and protons in nuclei. Only a weak magnetic interaction takes place between neutrons and electrons. How far a particle can penetrate in a material depends on the material and the type of particle. This is characterised by the mass attenuation coefficient. The chart in Figure 2.11 shows the mass attenuation coefficient as a function of the atomic number for X-rays and thermal neutrons. Multiplying the mass attenuation coefficient by the density ρ gives the linear attenuation coefficient $\mu[1/cm]$. For X-rays the mass attenuation coefficient increases with atomic number while for thermal neutrons it fluctuates but tends to be lower than for X-rays. The increased attenuation makes X-rays less suitable for probing deep (> 1mm) into the material.

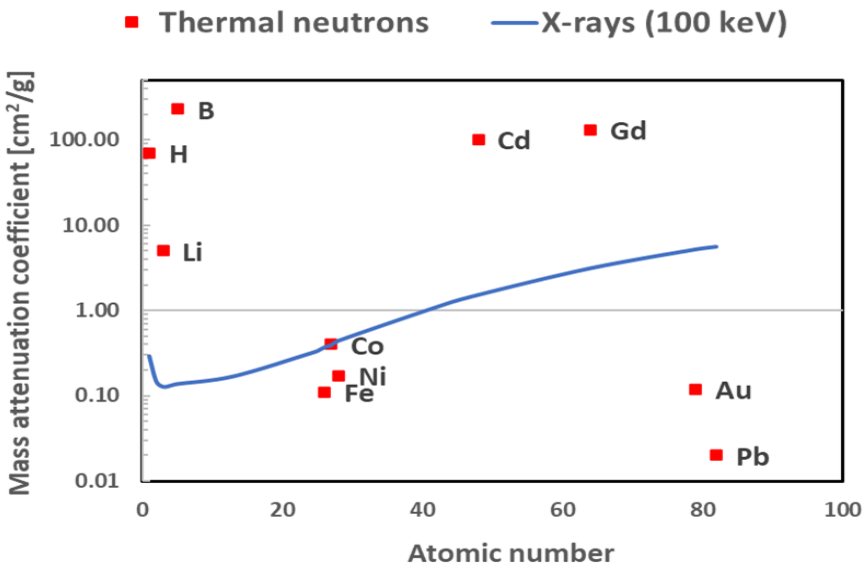

Figure 2.11: Mass attenuation coefficient for X-rays and thermal neutrons as a function of atomic number (copyright John Banhart Oxford Press)

Neutrons can be useful when investigating materials with higher atomic number or when probing deeper into the material up to ~ 1cm.

2.3.2 Neutron sources

Neutrons can originate from different sources. They can be produced using a nuclear reactor or by using a pulsed spallation source.

The neutrons produced by a nuclear reactor are a result of fission. Fission is a process where a heavy atom is split in different lighter highly radioactive atoms and releasing neutrons in the process. In subsequent decay processes these lighter atoms can release neutrons, electrons, neutrinos and photons. When a ${}^{235}_{92}U$ atom absorbs a neutron, it can split into a ${}^{141}_{56}Ba$ and ${}^{91}_{36}Kr$ atom releasing 3 neutrons in the process. These neutrons are referred to as prompt neutrons as they are produced directly as result of the fission process. The Barium and Krypton atoms are radioactive and decay into more stable atoms releasing neutrons, electrons, neutrinos and photons in the process. The neutrons produced in this decay process are referred to as delayed neutrons and play a crucial role in keeping the chain reaction going. During the process neutrons can be absorbed, they can escape the reactor and new ones can be produced. When this process is in balance then the reactor is said to be in a critical state. A reactor is a continuous source and produces a constant stream of neutrons.

In the spallation process, a synchrotron is used to accelerate protons using a magnetic field. Once the protons have reached a sufficiently high energy they are collided into a suitable block of material, in the case of the ISIS facility, Tungsten. The collision of the protons results in atoms breaking up in lighter atoms and other products including neutrons. A neutron spallation source is a pulsed source hence neutrons are produced on an intermittent basis.

To obtain a beam of thermal neutrons a moderator is used for both sources to slow down the neutrons, so that their wavelength is within a usable range, in most cases this should be comparable with the lattice spacing of the samples being characterised. Neutron beams produced with a nuclear reactor tend to have a larger flux than beams produced with a synchrotron at a spallation resource. This will change with the arrival of the ESS (European Spallation Source) beam at Lund in Sweden which will be the most brilliant source when operational.

2.3.3 Neutron diffraction

Neutrons can be described as behaving as waves; hence they can be diffracted by a crystal lattice. For neutron diffraction to happen, the Bragg criterion must be upheld. Hence, the wavelength of the neutrons needs to be of the same order of magnitude as the lattice spacing. The neutron wavelength for various energies is shown in Table 1.

Table 2.1: Neutron wavelengths for various energies

Type of neutron	Energy range (meV)	Temperature range (K)	Velocity (ms^{-1})	Wavelength (Å)
Cold	0.1 – 5	1 – 60	150 – 1200	10 – 80
Thermal	5 – 100	60 – 1000	1200 – 4800	2.5 – 10
Hot	100 -500	1000 – 6000	4800 – 12000	1 – 2.5

The magnitude of a typical lattice spacing is in the order of several Angstroms (Å). Thermal neutrons have a wavelength that is of comparable magnitude. Therefore, Bragg's law can be used to relate the wavelength of a neutron to the lattice spacing.

2.3.4 Scattering of neutrons

To this point, diffraction has been treated as a macroscopic wave phenomenon using the laws of classical physics. At the atomic level of the material these laws do no longer hold true and a quantum mechanical description of the scattering process is required. Scattering has proven to be a very useful tool in physics to determine a wide range of structures. In high energy physics it is used to determine the composition of sub-atomic particles and in low energy physics it is used to determine the crystallographic structure of materials. The simplest collision processes are scattering of a particle A by a potential field $U(r)$ and the elastic scattering of a particle A with a given momentum by a target particle B . Both classical and quantum mechanical scattering are characterized by the scattering cross-section σ. The SI unit for the scattering cross section is $[m^2]$, in nuclear and particle physics the conventional unit used for the scattering cross-section is the barn $[b]$, where $[1b = 10^{-28}m^2]$. The cross-section is calculated from the differential cross-section shown in Figure 2.12.

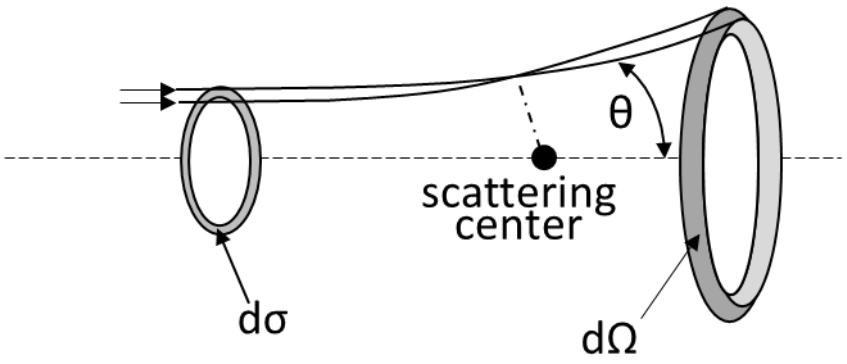

Figure 2.12: Differential cross-section [32]

The differential cross-section $\left({}^{d\sigma}/_{d\Omega}\right)$ is defined as the ratio of the number of particles scattered N in the direction (θ, φ) per unit time per unit solid angle divided by incident flux $|\mathbf{j}|$.

$$\frac{d\sigma}{d\Omega} = \frac{N}{|\mathbf{j}|} \tag{2.3.1}$$

The total cross-section is obtained by integrating the differential cross-section over all solid angles Ω. The cross-section depends on the energy of the incoming particles and can be separated in $\sigma_{elastic}$, $\sigma_{inelastic}$ and $\sigma_{absorption}$. In the case of elastic scattering the energy of the particle before and after scattering is the same, in the case of inelastic scattering the particle gains or loses energy and in the case of absorption the particle will be absorbed by the target nucleus. Different type of particles can be used to perform scattering experiments. The scattering process described here is applicable for neutrons. Neutrons can interact with atoms in many different ways. Because the neutron has no charge and has a mass relatively large compared with an electron there is only weak interaction with the electron cloud around the atoms. The lack of any electric charge on the neutron allows it to penetrate into the interior of any atoms it encounters along its path. There is no repulsive barrier for the neutron to penetrate in order to reach the nucleus. The main interaction will be with the nucleus of the atom in the form of scattering. This is very different for when a charged particle tries to reach the nucleus. A charged particle would require an energy in the order of magnitude of MeVs, to get through the Coulomb barrier and within range of the short-range strong forces of nuclear attraction. The neutrons interact with the atomic nuclei via the 'short range nuclear forces'. They also interact with unpaired electrons via a magnetic dipole interaction. The latter is important in strongly magnetic materials. The scattering of a thermalized neutron of a single fixed heavy nucleus is illustrated in Figure 2.13. The incoming neutron is represented as a plane wave e^{ikx} with wave vector $\mathbf{k_i} = k\mathbf{i}$ along the x-axis.

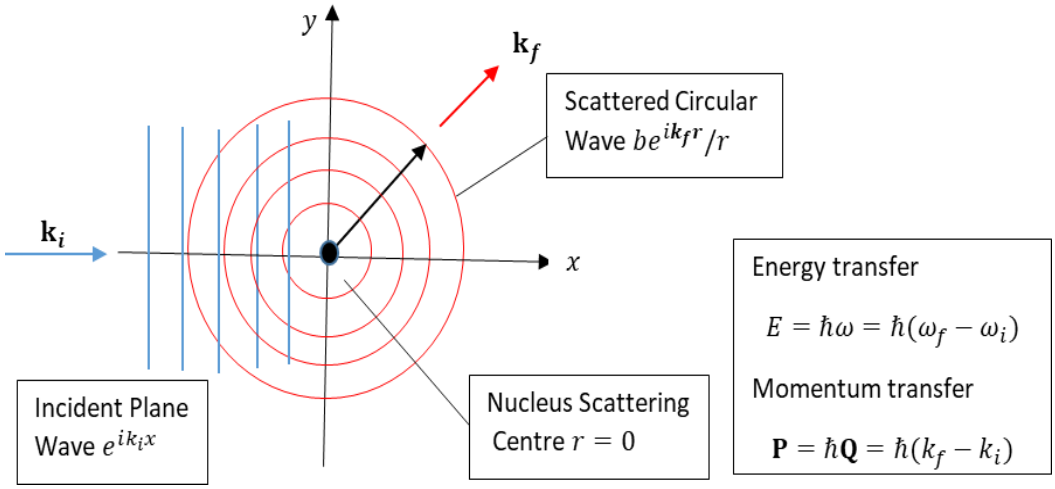

Figure 2.13: Neutron scattered by a single nucleus

Because the range of the nuclear force (~1 fm) is much smaller than the neutron wavelength we may represent the nucleus as a point. The outgoing neutron is represented as a circular wave $be^{i\mathbf{k}_f r}/r$ where $\mathbf{k_f}$ is the wave vector and b the scattering length. The scattering length is used to characterize the amplitude of scattering of neutrons by atoms is expressed in units of length and is of magnitude ~10^{-12} cm. Its magnitude depends on the atomic mass number (ie isotope) and on the

orientation of the nuclear spin relative to the neutron spin. The scattering length is a complex number but the imaginary part is sufficient small to be ignored [24].

The energy of a thermalized neutron is too small to change the energy of a heavy nucleus and no kinetic energy of the neutron is transferred to the nucleus. Hence the magnitude of the wave vector of the circular wave (outgoing wave) is the same as for the plane wave (incoming wave), that is, $|\mathbf{k_f}| = |\mathbf{k_i}|$. The neutrons momentum $\mathbf{P} = \hbar\mathbf{Q} = \hbar(k_f - k_i)$ and kinetic energy $E = \hbar\omega = \hbar(\omega_f - \omega_i)$ stays the same but it moves in a different direction after the interaction. This type of scattering is called elastic scattering. If the nucleus is of comparable mass to the neutron mass or the neutron has a much higher kinetic energy, then the neutrons could also gain or lose energy in the scattering process. This is called inelastic scattering and $|\mathbf{k_f}| \neq |\mathbf{k_i}|$. In a real neutron scattering experiment the incident beam would interact with a sample containing many atoms. Not every incoming neutron will be scattered. The probability of a neutron being scattered by a nucleus is dependent on the cross section of the nucleus. The scattering of a neutron from a sample is schematically illustrated in Figure 2.14. The incident wave(blue) will be scattered by nucleus at position $\mathbf{R}_j$ in the sample.

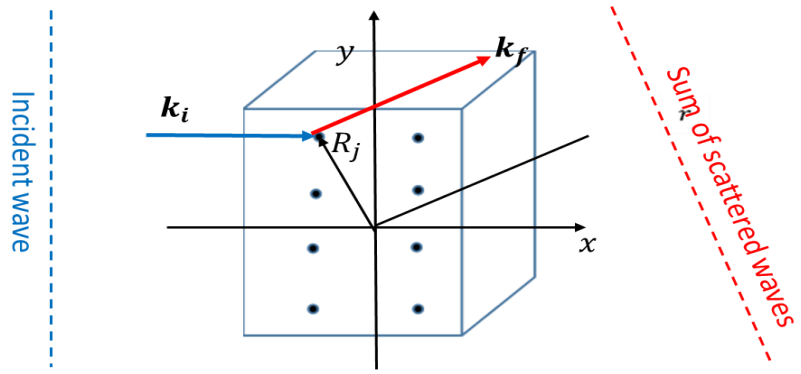

Figure 2.14: Sample cube; Black dots are atoms;R_j position of atom j; *Scattering of many nuclei (Source: ISIS Neutron Theory*[33]*)*

So neutron scattering is either elastic or inelastic, and coherent or incoherent. This gives four categories for scattering: coherent elastic, coherent inelastic, incoherent elastic and incoherent inelastic. All of them can be present in a single sample. Coherent elastic scattering (neutron diffraction) is important for studying crystal and magnetic structures. Coherent inelastic scattering is used in neutron scattering studies of elementary excitations of materials. Examples of excitations or phonons (vibrational waves) and magnons (spin waves). In phonon studies a neutron loses energy when creating a phonon (inelastic), however the scattering amplitude depends on the phases of the atom movements in the phonon and the phases of the incident and scattered neutron waves(coherent). Incoherent elastic scattering may occur for example if the material contains a random mixture of isotopes. The phase of the scattered wave differs for each isotope which will result in some incoherence. Incoherent inelastic scattering can provide information on the sample

dynamics like diffusion mechanisms. Figure 2.15 provides an illustration of the four categories of scattering and for which area of study they are most suitable.

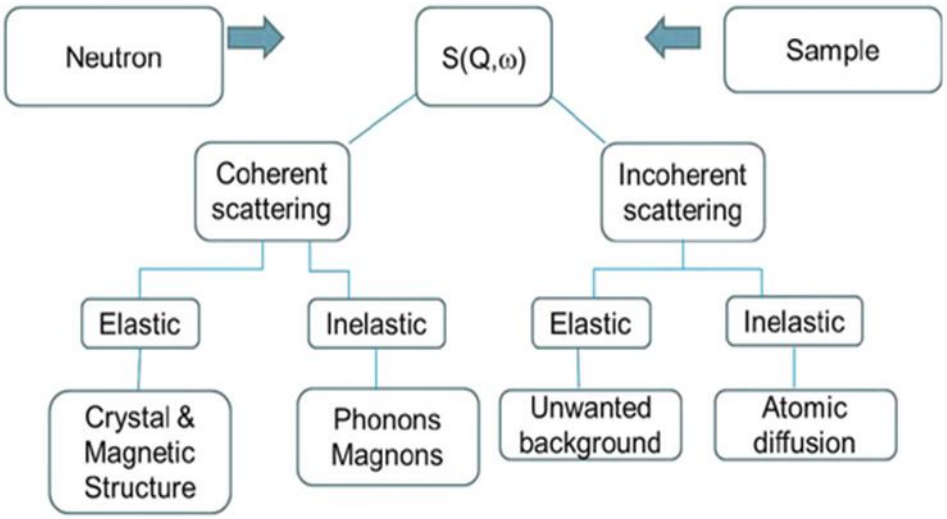

Figure 2.15: Schematic of different types of scattering, $S(\boldsymbol{Q}, \omega)$ is the scattering function

2.3.5 Measuring residual stress using neutron diffraction

Each material has a unique spectrum. If the spectrums of a stress- and stress-free samples are compared, the spectrum in the stressed sample will show that the peak positions have shifted relative to the peak positions in the stress-free sample [34]–[36]. This shift can be used to calculate the strain in the sample under stress.

2.3.6 ENGIN-X time of flight instrument

An example of a time of flight instrument is ENGINX located at ISIS (Rutherford Appleton Laboratories). ENGINX is the successor of ENGIN [11] and was commissioned in 2003[12][13]. It was specifically designed for making engineering strain measurements and can handle large components weighing up to 1T as shown in Figure 2.15.

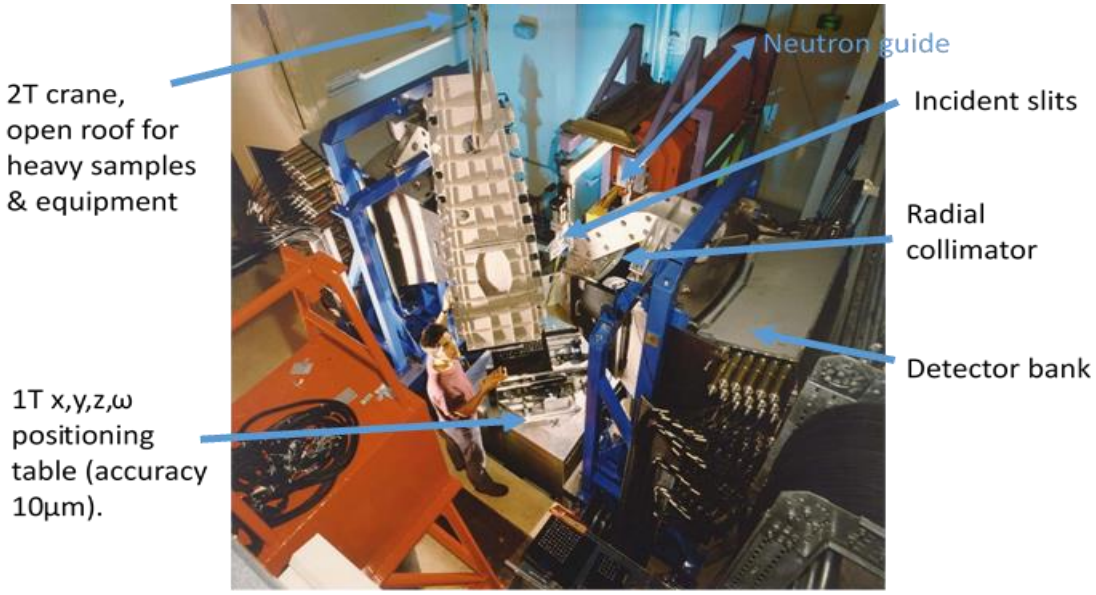

Figure 2.16: ENGIN-X at ISIS RAL - component shown is part of an aeroplane wing

The purpose of a time of flight neutron diffractometer is to measure the strain at specific locations in the bulk of a given specimen; a schematic is shown in Figure 2.17**.** The geometric intersection of the incident beam and the diffracted beam is referred to as the Instrument Gauge Volume (IGV) and its dimensions are controlled by the slit opening and the collimators.

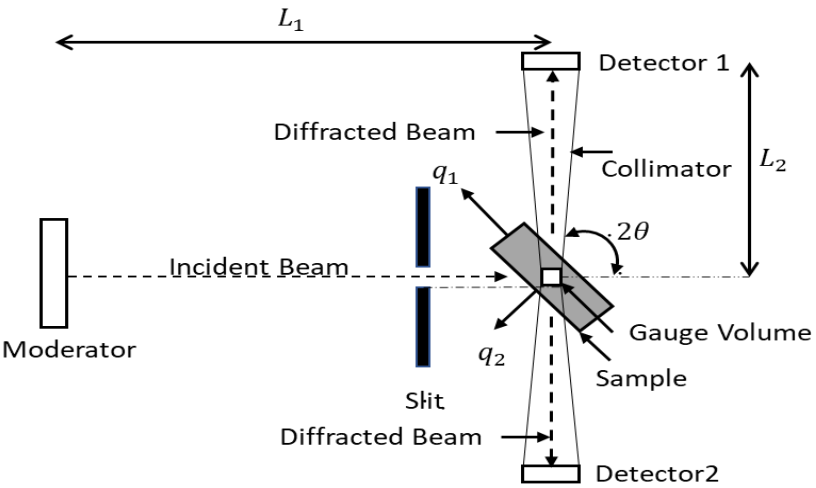

Figure 2.17: A schematic of a time of flight neutron strain scanner. The elastic strain is measured along the directions of the impulse vectors, q_1 and q_2.The intersection between incident beam and diffracted beam defines the volume of the sample that is explored.

The part of the sample that coincides with the IGV is referred to as the Sample Gauge Volume (SGV). The pulsed beam consists of neutrons with a wide range of energies that travel from the moderator to the sample, where a small fraction of the neutrons is scattered into a detector at an angle of 2θ. The wavelength of the detected neutrons, assuming it is an elastic collision, is defined from its TOF τ (s),

$$\lambda = \frac{h\tau}{m_n(L_1 + L_2)} \tag{2.3.2}$$

with h (Js) being Planck's constant, m_n(kg) the neutron mass and L_1 (m) and L_2 (m), the primary and secondary flight paths, respectively. A typical diffraction pattern of a polycrystalline material is shown in Figure 2.18.

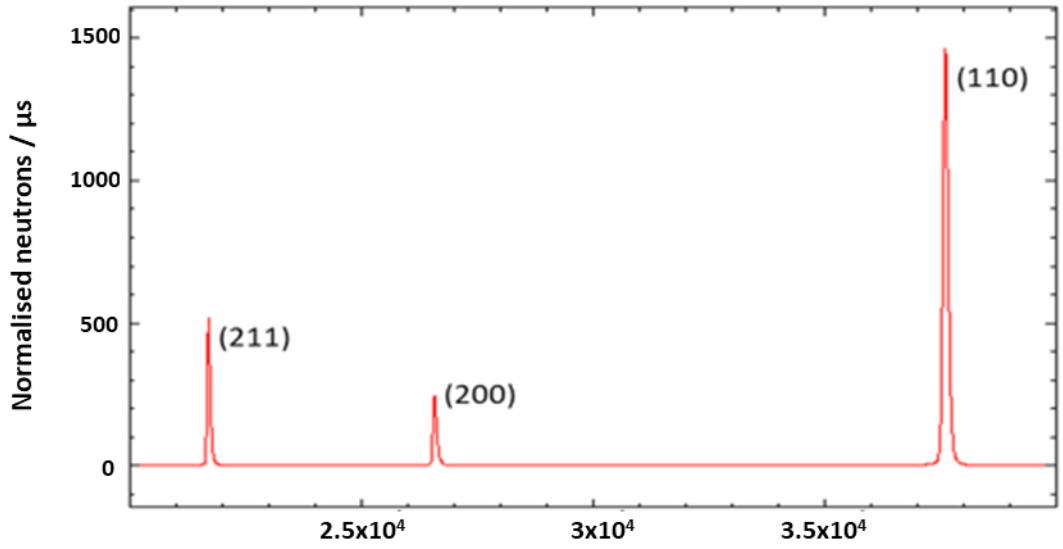

Figure 2.18: Part of diffraction pattern for Fe-alpha; each peak corresponds to a different lattice plane(hkl)

Each peak in the pattern corresponds to an (hkl) family of lattice planes as defined by Bragg's law $\lambda_{khl} = 2d_{hkl}\sin\vartheta_{hkl}$. The d-spacing is then obtained from the position τ_{hkl} of the peak in the TOF spectrum,

$$d_{hkl} = \frac{\lambda}{2\sin\vartheta_{hkl}} = \frac{h}{2m_n(L_1 + L_2)\sin\theta_B}\tau_{hkl} \qquad (2.3.3)$$

The positions of the peaks can be determined to a high degree of precision ~ 50με (1 με=1x10^{-6}) by least-squares refinement of the peaks.

2.3.6.1 Electronic time focussing

A neutron beam from a spallation source like at ISIS(RAL) is comprised of pulses with each pulse having a range of wavelengths. The detectors in the case of ENGINX are arranged radially around the centre of the gauge volume. Therefor Bragg's equation is satisfied, for the same d_{hkl} for different combinations of wavelength λ and angle θ. Figure 2.19 (a) shows the detectors, detector elements and collimators of ENGINX and Figure 2.19 (b) shows the gauge volume and an individual detector. Each detector element records intensity versus time of flight.

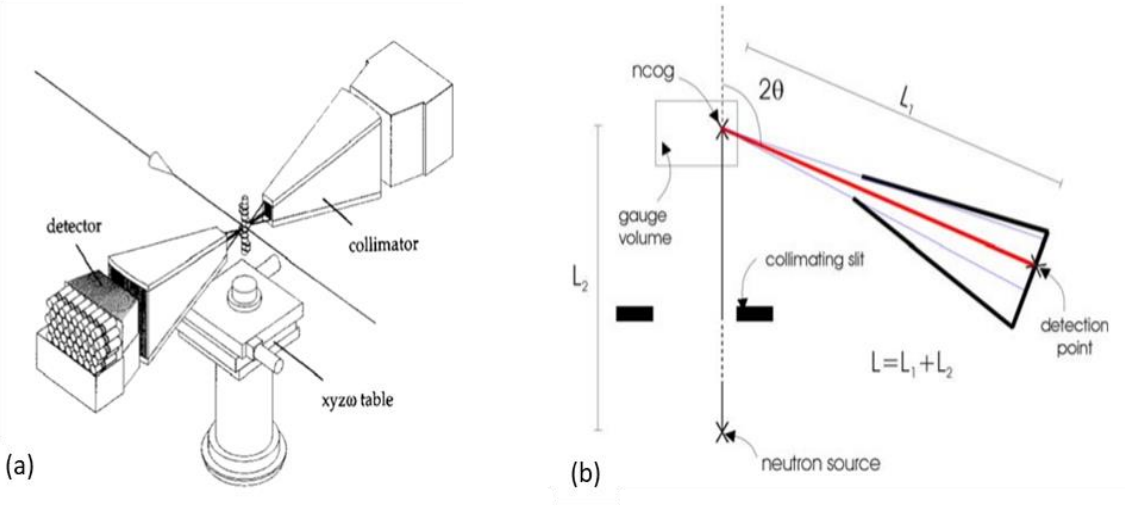

Figure 2.19: (a) Schematic of ENGINX showing detector, detector elements and collimator; (b) The gauge volume, diffracted beam(Red) and individual detector element[37].

Therefor every particular d_{hkl} peak will be recorded in each detector element, but because the θ of each detector element varies, the same peak will correspond to a different time of flight in each element. As each detector element is physically small the number of neutrons making up the individual spectra will generally be too low to provide a clear peak. To get better statistics the spectra from each of these detector elements is mapped onto a single detector element (usually the central element which on ENGINX is at $2\theta = 90$). This is achieved using the technique of 'electronic time focussing'[38]. In this technique the time of flight of neutrons recorded in the individual elements is adjusted to be the value it would have had, had the neutron been recorded in the central ($2\theta = 90°$) detector element.

Using (2.3.3) the peak position in d-spacing may be expressed in terms of the measured TOF τ_i for detector element i

$$d_{hkl} = \frac{h}{2m_n L_i \sin\theta_i}\tau_i \tag{2.3.4}$$

where L_i is the total flight path length $(L_1 + L_2)$. Using the concept of pseudo-time[37], which is the TOF τ^* that would have been measured by a detector located at a reference position L_0 and Θ_0 (usually $2\Theta_0 = 90$), we have

$$\tau^* = \frac{2m_n d_{hkl}}{h} L_0 sin(\Theta_0) \tag{2.3.5}$$

Combining Equations (2.3.4) and (2.3.5) gives

$$\tau^* = \tau_i \frac{L_0 sin(\Theta_0)}{L_i sin(\Theta_i)} \tag{2.3.6}$$

For a radial detector it is assumed $L_i = L_0$. Spectra from ENGINX are electronically time focussed in this manner. This time focussing technique has been implemented in the virtual detectors in McStas.

2.3.6.2 Calibration

The instrument consists of a number of components like a guide, benders, slits and the sample. Each of these components can alter the path length the neutron travels. Therefor the path the neutrons follow through the instrument will most likely differ from the distance $(L_1 + L_2)$. There is also uncertainty in the scattering angle θ_B. For example, both the scattering position within the sample as well as the angle of incidence of the scattered neutron are unknown. Variations in L and θ_B can potentially have a large impact on the residual stress measured which could be of the same order of magnitude as the residual stress being measured. In addition to the uncertainty in L and θ_B there is uncertainty in τ_{hkl} arising from the finite precision of the timing electronics. Representative values for L and θ_B are obtained through calibration of the instrument.

The lattice spacing d_{hkl} is determined using an empirical formula that relates the time-of-flight τ_{hkl} to the lattice spacing considering instrument dependent characteristics

$$\tau_{hkl} = zero + difc * d_{hkl} + difa * d_{hkl}^2 \tag{2.3.7}$$

where

$\boldsymbol{zero}[\boldsymbol{s}]$ is a parameter that accounts for small differences between the various timing signals in the accelerator and the instrument data acquisition system, and allows for the finite response times in the detector electronics.

$\boldsymbol{difa}[\boldsymbol{m^{-2}s}]$ is a parameter that introduces small corrections to the expected TOF to allow for peak shifts due to absorption in the sample. The neutron absorption cross-section of an atom is wavelength dependent. Shorter wavelength neutrons will experience less absorption than larger wavelength neutrons. The quadratic dependence has been empirically derived.

$\boldsymbol{difc}[\boldsymbol{m^{-1}s}]$ is an instrument dependent parameter and relates the theoretical TOF of the measured Bragg reflection to its lattice spacing. Rearranging (2.3.3) $difc$ can be expressed in terms of L and θ_B, that is,

$$\tau_{hkl} = \frac{2m_n(L_1 + L_2)\sin\theta_B}{h} d_{hkl} \tag{2.3.8}$$

Comparing (2.3.8) and (2.3.9) gives

$$difc = \frac{2m_n(L_1 + L_2)\sin\theta_B}{h} \tag{2.3.9}$$

The parameters $zero$, $difa$ and $difc$ are referred to as diffractometer constants. To obtain values for these constants an instrument calibration measurement is done. For this calibration a powder sample of known lattice parameter is used.

The first step in this calibration process is to obtain a good spectrum in each detector element. Then for each spectrum a Rietveld fit[39] is applied while holding the lattice parameter fixed, to obtain values for the parameters $zero_i$, $difa_i$ and $difc_i$ for each detector element. An instrument like ENGIN-X has over a 1000 detectors elements. The element specific $zero_i$, $difa_i$ and $difc_i$ are then formed into a focussing table which is used to combine spectra from each element into a single spectra for each of the two detectors; thus effectively creating a virtual instrument with just two single element detectors at $2\theta = 90$ degrees.

The second step of the calibration process uses the same powder sample but now the jaws and collimators are set up specific for the measurement at hand to determine a single set of $zero$, $difa$ and $difc$ parameters for each of the two virtual detectors. When performing an experiment those parameters are important as they will be used in the peak fitting process when using Rietveld or Pawley method. For McStas those parameters stay fixed as the virtual instrument is not subject to changes in settings due to operational use like the real instrument.

2.3.6.3 Data analysis

To determine the residual stress in a component the lattice spacing of the material is measured using neutron diffraction. This lattice spacing is compared with the lattice spacing of a stress free sample of the same material obtained through a different source. Using ENGINX to perform such a measurement results in an output file containing the neutron intensities as a function of the time-of-flight. To determine the lattice parameter a Rietveld [40][41] refinement is applied to this experimental profile of the spectrum. The Rietveld refinement is a method for estimating the intensities of Bragg peaks in a powder diffraction pattern. The entire diffraction profile is calculated (model) and compared with the observed profile point by point. A trial structure (model) is used to calculate the intensities of the peaks in the experimental pattern. The parameters of the model are then adjusted using the Least-Square method to obtain the best fit. The Model consists of 3 parts:

1. Crystallographic Model: describes size, symmetry of unit cell, atomic positions, thermal parameters and occupancy
2. Instrumental Model: describes optics and set-up of diffractometer
3. Profile Model: describes peak shape

Model data is minimised iteratively until a satisfactory answer, that is, a good fit between experimental and calculated pattern is obtained. The output of the Rietveld refinement is a

spectrum. The positions of peaks in this spectrum correspond with the different plane orientations. An example of such a spectrum is shown in Figure 2.18. The peak positions of a stress-free sample are compared with the positions of the peaks for the same planes for a stressed sample. The shift in the peaks can be used to calculate the strain,

$$\varepsilon_{hkl} = \frac{d_{hkl} - d^0_{hkl}}{d^0_{hkl}} = \frac{\tau_{hkl} - \tau^0_{hkl}}{\tau^0_{hkl}} \tag{2.3.10}$$

Where d^0_{hkl} represents the lattice spacing for material free off residual stress and d_{hkl} is the lattice spacing for material with residual stress. Instead of a Rietveld fit it is also possible to do a single peak fit. In this case one or more peaks are fitted individually using the least squares method. This is a simplified fit not using the models described above but can be useful where the Rietveld or equivalent fitting methods cannot clearly distinguish between peaks that are very close to each other.

2.3.7 SALSA

An example of a reactor based diffractometer is SALSA (Strain Analyzer for Large and Small scale engineering Applications) [42] located at ILL (Institut Laue-Langevin) in Grenoble and can handle large components like an aero-engine fan blade as illustrated in Figure 2.20 . SALSA is a monochromatic strain diffractometer stationed on a continuous flux neutron beam. For constant wavelength diffraction, the energy (wavelength) and direction (collimation) of the incident beam needs to be adjusted. For that purpose, a crystal monochromator is used to select a particular wavelength band out of the poly-chromatic beam.

Figure 2.20: Photograph of SALSA with an aero-engine fan blade on the sample table(ref)

The wavelength selected is such that the Bragg reflection condition $\lambda = 2d_{hkl}\sin\theta_{hkl}$ for the scattering plane (hkl) is met. The use of radial focussing collimators results in a transmission of the

whole divergence of the beam whilst defining a precise gauge volume. They also reduce the extent of anomalous shifts in diffraction peak position as the sample gauge enters or leaves the engineering component. This capability allows precise measurements near surfaces and interfaces[43]. A schematic of a of SALSA is shown in Figure 2.21.

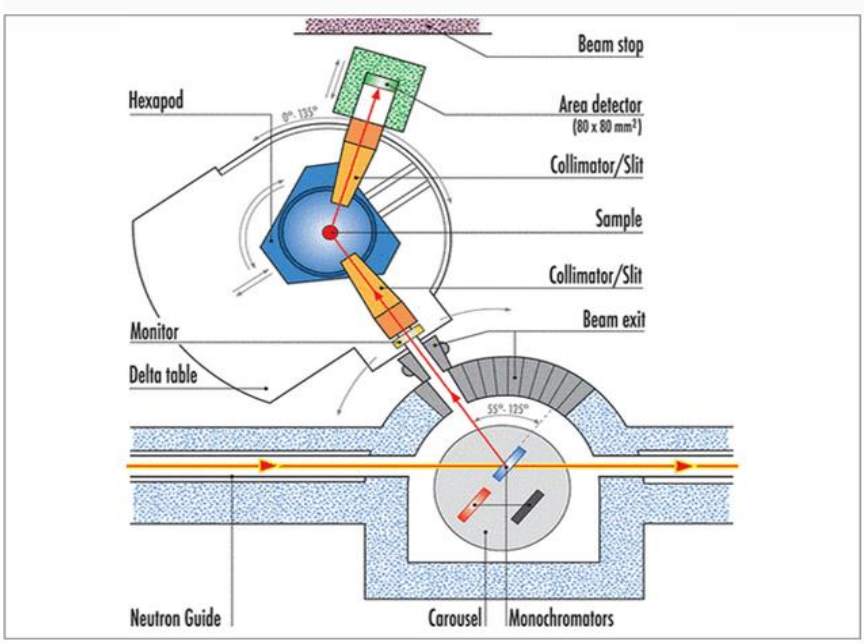

Figure 2.21: A schematic of the SALSA instrument. The hexapod shown is optional and not needed for the experiments described in this research.

To determine the residual stress in a component the lattice spacing of the material is measured. This lattice spacing is compared with the lattice spacing of a stress-free sample of the same material obtained through a different source. For each experiment a single reflection is optimised to be at 90 degrees. And because of the limitation in detector size, only a single reflection can be collected at one time. All the other reflections are still occurring, but just not collected. The output of the measurement is a diffraction pattern. Usually a fitting routine is used to determine the peak centre angle and angular width from the profile of detected count intensity variation with angle which is often represented by a Gaussian function[44]. Knowing the peak centre angle θ_{hkl} and using Bragg's law, the strain can then be calculated as

$$\varepsilon_{hkl} = \frac{d_{hkl} - d^0_{hkl}}{d^0_{hkl}} = -(\theta_{hkl} - \theta^0_{hkl})\cot\theta^0_{hkl} \qquad (2.3.11)$$

where d^0_{hkl} represents the lattice spacing and θ^0_{hkl} the Bragg's reflection angle of the stress-free material.

2.4 Welding

Joining components is a common requirement in manufacturing and construction industry. There are many techniques available for joining components. Welding is one such technique commonly used to join metal components. Most welded joints are made by melting the metal on each side of the joint line. The molten metal combines to form a weld pool which on solidification forms a metallic bridge between the two components of the joint. This is referred to as fusion welding. There are various welding processes available and which one to use will depend on to what the weld will be subjected to during its operational life. In a nuclear powerplant the operating conditions can be very harsh exposing a weld to high temperatures, high pressures and a corrosive environment. Another industry making intensive use of welding is the aircraft engine manufacturing industry. The welds in an aircraft engine are also exposed to a very demanding operational environment. An area of particular interest both in nuclear power plants and aircraft engines is the welding of dissimilar alloys[45]. The welding of dissimilar welds in the aeroengine industry is seen as a way to improve efficiencies of modern engines. [46].

2.4.1 Fusion welding and residual stress

For fusion welding a suitable source of heat is needed and shielding to protect the weld pool against atmospheric contamination. Fusion welding uses a localised injection of intense heat and most of the heat flows through the parent metal on each side of the joint[47]. The two parameters most critical are the maximum temperature reached and the rate of cooling subsequently. The weld micro-structure in each location is closely related to the thermal history with changes in grain structure, the presence of second phases and defects all reasonable in even the best fusion welds. Moving away from the fusion zone the temperature falls until the parent metal ceases to be heated. The temperature will reach a point at which no relevant metallurgical or stress changes take place. The region of the parental metal which has undergone a metallurgical change as a result of the thermal cycle is called the heat affected zone (HAZ). The parent metals will be made up of more or less uniform grains but the weld metal is composed of dendritic grains which have grown from the molten pool on solidification. A list of some of the commonly used fusion welding processes is given in Table 2.2.

Table 2.2

Welding process	Heat source	Type of operation	Application
Oxy-acetylene (gas) welding	Fuel gas flame	Manual	Small bore pipework; Light fabrications
Tungsten inert-gas (TIG) welding	Arc	Manual	High quality welds in metals such as stainless steel, aluminium and copper; sheet work in aircraft engines
Manual metal arc (MMA) welding	Arc	Manual	Fabrication of pressure vessels; joints in pipework and pipelines;
Resistance spot welding	Resistance heating at an interface	Automatic	Light fabrications from pressed sheet, such as car bodies; High quality work in aircraft engines.

Where many other joining techniques involve operations that can be standardised and adapted to machine production and control, fusion welding due to operating factors is less suitable for automation. The success or quality of fusion welding therefore depends on the skill of the person operating the process. The nature of the welding process involving heating an area to a very high temperature and then cooling it down leads to changes in the metallurgy of the material in the weld zone and in the HAZ. These are micro-structural changes which lead to residual stress in the weld. Near the surface this is tensile stress but deeper (~3mm) into the weld it is compressive[48].

2.4.2 Welding of components used in nuclear power plants

A nuclear power plant is made up of thousands of components and although in new nuclear plant designs the emphasis is to reduce the number of components it is unavoidable that components will have to be joined. Welding is used intensively as a joining technique when building a nuclear power plant. The welds are often between components made of different alloys such as austenitic stainless steel and ferritic steel. These welds are referred to as dissimilar metal welds (DMW)[27], [49]–[54], one such weld is illustrated in Figure 2.22.

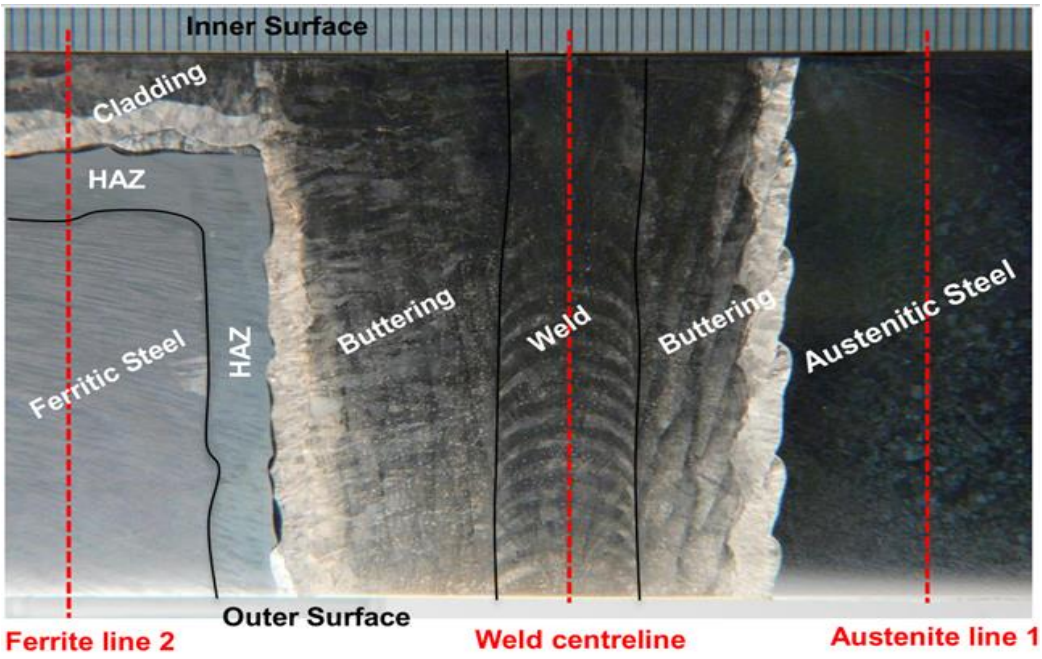

Figure 2.22:Dissimilar metal weld between ferritic steel and austenitic steel manufactured by Areva. Source: Traore, Y. et al. (2014).

Measuring the residual stress in this type of weld is challenging due to the presence of microstructural features like large grains, step change in chemical composition, crystallographic texture and complex variation in d_0. There may also be pores or defects, seen here between the ferritic steel and buttering, which can act as the initiation site of cracks and therefore characterisation of residual stress in the region close to these defects is critical.

2.4.3 Measuring residual stress in welds using neutron diffraction

Because of the localised heating occurring during welding and the consequently varying levels of strain mismatch resulting from differing levels of thermal contraction residual stress is often a key consideration for the structural integrity of welds. However, the presence of the microstructural features mentioned above make this quite challenging, as discussed in the next section. Verifying the type of metallurgical changes that take place as a result of the welding process are important as they define the quality of the weld. Non- destructive methods such as neutron diffraction can be used to check a weld[55] and to identify types of defects discovered, their size and location in the weld, but it cannot tell if the weld is acceptable or not. Typical problems arising when measuring stress in welds are temperature gradients, the presence of large grains and pores/voids that can lead to an underestimation of the residual stress. To perform the necessary scans using neutron diffraction takes time and beam time is expensive with limited availability due to high demand.

2.5 Literature review of pseudo strain errors

Measuring strain using neutron diffraction may give rise to errors or uncertainties from many different sources. This type of error to be focused on in the dissertation are those arising from failing to fulfil the assumption that the measurements sampled volume is isotropic and

homogeneous. This is often referred to in the literature as pseudo-strain, spurious strain or surface effect. Early examples of pseudo-strain effects are described in [26], [56]–[60]. Because these errors manifest themselves in a shift of the diffraction peak, which is also a manifestation of strain, the term Pseudo strain is appropriate. From this point on, the term pseudo strain will be used for any aberration that results in a shift in diffraction peak, as a result of deviations from the assumptions made about the uniform nature of the measured material.

2.5.1 Sources of pseudo strain

Pseudo-strains may arise from various sources such as geometric, attenuation, wavelength, surface, grain size, micro-strain and texture. Not all of these sources causing pseudo strain need to occur at the same time. In some measurements it is purely geometric, in others it can be geometric, attenuation and grain size all contributing at the same time. The composition of the gauge volume plays an important role in understanding the nature of these root causes. The gauge volume represents the region of diffracting material over which a measurement is made and is described by the intersection of incident and diffracted beams. The pseudo-strain in near surface strain measurements[61][37] stems from the gauge volume only partially filled with material. To link a lattice strain to a point in the sample material the most representative location of the scattering volume, the neutron-weighted centre of gravity (NCOG) is used, as shown in Figure 2.19. The NCOG takes into account variations in intensity due to attenuation or absence of sample material in the gauge volume.

For a time of flight instrument like ENGINX the variation in the position of the NCOG due to attenuation effects or partial filling of the gauge volume will result in variations in the neutron flight path length L and the scattering angle θ_{hkl}. From equation (2.3.3) it follows that this change in L and θ_{hkl} will cause variation in the measured lattice-spacings, that are not related to residual stress and thus introduces an error in the value of the lattice strain. This variation can be expressed as

$$\frac{\Delta\tau}{\tau} = \frac{\Delta d}{d} + \frac{\Delta(L\sin\theta_{hkl})}{L\sin\theta_{hkl}} \tag{2.5.1}$$

This expression states that the peak shift is the sum of the lattice strain due to the residual stress plus the pseudo-strain. The pseudo-strain, ε_{ps}, can be split into a spatial and angular component:

$$\frac{\Delta(L\sin\theta_{hkl})}{L\sin\theta_{hkl}} = \frac{\Delta L}{L} + \cot\theta_{hkl}\Delta\theta_{hkl} \tag{2.5.2}$$

The above expressions relate to a TOF instrument like ENGINX however pseudo-strain also arises when using a diffractometer like SALSA that measures the change in diffraction angle with the wavelength varying over a narrow range. Pseudo-strains are not limited to near surface strain measurements with gauge volume partially filled but can also arise in measurements in which the

material within the measurement gauge volume is not homogeneous and anisotropic. This is the case when the gauge volume contains: a) two different materials as in metal to metal interface or b) when measuring in the vicinity of large grain bundles such as occur in DMW's. Pseudo strain can also occur due to wavelength-dependent attenuation of the incident and/or diffracted beam[62][61] when measuring deep in the materials.

2.5.2 Mitigation techniques

The magnitude of the pseudo-strain can be large (1x10-3 (1000μstrain) in comparison to the resolution of the instruments used to measure such strains(50μstrain) and therefore require correction. Different ways to mitigate pseudo-strains are proposed. The proposed solutions depend on the instrument used for measuring the strain. For a TOF instrument like ENGINX, Creek et al. have developed a model of a system that uses a radially collimated diffracted beam and evaluates two methods for calculating the pseudo-strain due to attenuation and surface scanning. To correct for the pseudo-strain an accurate 3D model of the system should be built and the pseudo-strain measured by each detector element from each point in the gauge volume should be evaluated. This is very complex and would require significant computation time. Therefor a 2-dimensional model is used by Creek et al. as a pragmatic, computationally efficient solution. The first method approximates all scattering to the NCOG and calculates pseudo-strain relative to this point. The second method is an integration of the pseudo-strains over the entire gauge volume. Taran and Balagurov[63] propose an analytical method to calculate the pseudo-strain effect in a thin-walled sample using the concept of pseudo-time introduced by Creek et al[37] for a TOF instrument.

An experimental approach for correcting pseudo-strain errors is to rotate the sample $180°$ and repeat the measurements. This approach makes use of the fact that the displacement of the NCOG is moving in opposite directions when scanning either from the front-side or the rear-side of a sample, resulting in the pseudo-strain shift moving in a point symmetric way. The results of the two measurements will cancel out the pseudo-strain. This is an inefficient process as two measurements are required, limited in precision and may not always be possible due to the geometry of the sample. Pirling et al. have developed a method for a continuous beam instrument (SALSA) that eliminates the need to perform two measurements. In this case a mathematical model has been developed that can be fitted to the measurement and subtract the pseudo-peak shifts. The model is an analytical description of the peak shift and is depending on the sample position and takes into account the scattering angle, beam intensity profile, linear absorption coefficient of the sample material and the wavelength distribution in the primary beam. This model has the benefit that when the beam profile and wavelength distribution are determined, measurements can be done and analysed at any diffraction angle 2θ and for different materials.

The mitigation methods described above are specific to the type of instrument, the type of measurement (near surface strain measurement) and/or sample geometry. These methods may not be adequate to mitigate for pseudo-strain when measurements involve gauge volumes composed of inhomogeneous and anisotropic materials as is the case in metal to metal interfaces and in the vicinity of large grain bundles as occur in DMW's. To improve the understanding of pseudo-strain arising in these cases and to mitigate for it an alternative approach is proposed using Monte-Carlo neutron diffraction simulation.

2.6 Neutron diffraction simulation software

There are several software packages like McStas[64], Vitess[65] and McVine[66] that can be used to perform neutron diffraction simulations based on the Monte Carlo method. For this research project McStas was chosen. This choice was made for practical reasons and McStas being open source software. The instrument assessed in this research project is ENGIN-X, a diffractometer located at ISIS (RAL) for which already a virtual model of ENGIN-X existed in McStas. A further argument supporting the choice of McStas was the fact that it was already installed and maintained on the High Power Computer (HPC) at ISIS. The simulations are very computing intensive and access to a High Power Computer is a significant advantage as it reduces the simulation times from potentially tens of hours per sample scan to 2 to 3 hours.

2.6.1 Ray tracing

To model neutron diffraction on a computer raises several challenges. A common technique to model light waves and to track them is using ray tracing. Light waves are made up of photons and this technique represents each photon as a ray which is traced when travelling through the instrument. A visualisation of light rays interacting with objects and as seen by an observer is shown in Figure 2.23.

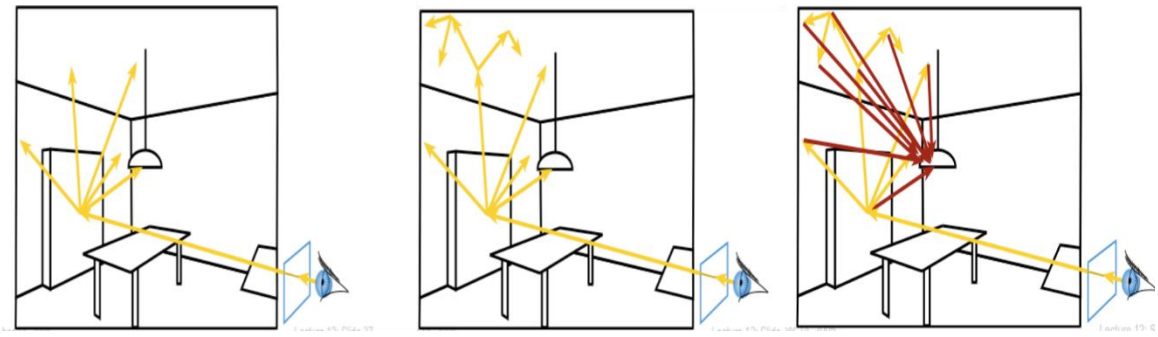

(a) Cast rays to every pixel of a scene

(b) Recursively cast secondary random rays from visible points

(c) Send rays to light

Figure 2.23: Interactive Computer Graphics course notes Source: Gilles, D.F.

This technique can also be applied to neutron waves replacing the photons by neutrons. The first step is to generate these neutron rays with the desired wavelength and then track the neutrons as

they travel through the neutron diffraction instrument, predicting the interaction, or lack of it, with each part of the diffractometer. Any instrument in McStas has a neutron source component to generate neutron rays. Dependent on the type of neutron source a different source component type is used. To generate neutrons equivalent to the thermal neutrons used in a time-of-flight instrument the source component type uses a randomizer. Instruments in McStas are made up of various other components with which the neutron ray interacts. Which component types are used depends on the real instrument that is modelled. How each neutron interacts with the various components used depends on the type of component the component is using. The neutrons can be absorbed by the component, reflected, scattered (elastically or inelastically) or pass through without any interaction. During the time of flight of the neutron its position, velocity and spin before and after interaction are logged and can be written to files provided "monitors" are added at the relevant places in the instrument. The interaction is a semi-classical process and uses classical optics theory to handle the wave behaviour of the neutron and quantum mechanical theory to handle the scattering of the neutrons. The outcome of the classical interaction will be predictable but the quantum mechanical scattering will be based on probability. The scattering of neutrons by the nuclei using the quantum mechanical scattering theory involves the calculation of a large number of complex multi-dimensional integrals. This probability aspect inherent in quantum mechanics and the complexity of the calculations is where the Monte Carlo method becomes useful

2.6.2 Monte-Carlo method

The Monte-Carlo method[67][68] was first used in a scientific environment during the Manhattan project for large scale calculations of neutron scattering and absorption which are processes that are suitable to use random numbers. The MC method can be defined as representing the solution of a problem as a parameter of a hypothetical population, and using a random sequence of numbers to construct a sample of the population, from which statistical estimates of the parameter can be made [69]. Many of these integrals could have been calculated using numerical methods but it would have been too time consuming. The difference between the numerical technique and the MC method for estimating the value of an integral can be illustrated by looking at a calculation of a simple integral. Let $f(x)$ be a finite continuous integrable function of parameter x for which an integral estimate is sought. The discrete statistical mean value of f in the uniformly sampled interval $a < x < b$ converges to the mathematical mean value of f over the same interval, that is,

$$\lim_{n\to\infty} \frac{1}{n} \sum_{i=1, a\le x_i\le b}^{n} f(x_i) = \frac{1}{b-a}\int_a^b f(x)dx \qquad (2.6.1)$$

In the case were the x_i values are regularly sampled, this corresponds to the midpoint integration rule. When the values for x_i are randomly, but uniformly sampled this integration is known as the MC integration technique. The MC method is more efficient than the numeric method when the

number of parameters (dimensions) exceeds 5. Neutron diffraction simulation involves the calculation of 10 dimensional integrals (neutron position (3), velocity(3), spin(3) and time(1)) for each neutron, with a typical diffraction experiment requiring the simulation of billions of neutrons.

2.6.3 Building a virtual model of an instrument in McStas

To design a model of an instrument in McStas it is recommended to start from an up to date architectural design document because slight differences in actual and modelled geometry can have a large impact on neutron ray paths. If that is not available a detailed document needs to be drafted up describing the instrument in detail before starting the modelling. The guiding design principle is to build a model that is as close as possible to the real instrument. The model of a neutron diffraction instrument in McStas can be divided into four main sections:

(1) Moderator
(2) Guide system
(3) Sample assembly
(4) Collimators + detectors

Each of these sections is made up of one or more components. A component is based on a component type and the same component type can be used as many times as needed. A component type consists of input parameter segment, a processing segment and an output segment. The input segment allows parameters specific to the working of this component to be passed on. The number of input parameters varies by component type, the most common ones are the dimensions of the component. The processing segment handles how neutron rays interacting with this component will be handled, this can include reflection, coherent and incoherent scattering processes, absorption and exceptions if applicable. The output segment can write neutron information to an output file or pass it on as output parameter values that will be used as input by the next component in the instrument. The most commonly used component types are arms, guides, choppers, slits, samples, collimators and detectors/monitors. These component types are included in the distribution of the McStas software. Sometimes a standard component type may not be adequate to replicate the interactions with a fully bespoke component. In such cases a bespoke component type can be build and many of these are also included in the distribution of McStas and they are referred to as “Contributed component types”.

2.6.4 Component types

There are many different component types available in McStas and to understand how they work is essential when building a new virtual model. In this section the working of the most often used component types will be discussed.

2.6.4.1 Progress bar

The progress bar is a component type that is positioned at the start of the instrument. This component type acts as a monitor and gathers statistics during a simulation.

2.6.4.2 Source

The source is a component type used to generate neutrons to be used in the simulation. The McStas distribution contains generic component types that can be used to emulate neutrons produced by a reactor source as well as neutrons generated by a spallation source. These components are also referred to as moderators because they contribute to the combined function of generating and moderating the neutrons by means of generating the distribution of neutrons entering the instrument.

2.6.4.3 Arms

The arm is a component with very basic functionality and does not interact with the neutrons. This component type is usually used to fix the coordinate system for a set of components that are part of the instrument. This is particularly useful when working with samples that are rotated and/ or moving through the beam in a scan scenario. Using arms in this scenario allows the sample to move relative to a specific arm while other components like collimators, monitors and detectors stay in a fixed position.

2.6.4.4 Slits

A slit is a component type that is used to control the shape and size of the beam. The McStas library includes a generic rectangular shaped slit. The opening of this slit is set with the parameters `xwidth` and `yheight`. Neutrons that do not pass through the slit opening are absorbed by the slit. This modelled slit is infinitely thin whereas the slits in real instruments, have a finite thickness. To mitigate the discrepancies in instrument geometry resulting from the infinite thinness, a gap is added between the component that precedes the slit and the slit itself to ensure the total neutron flight path length remains the same as in the real instrument. Instead of adding a gap it can sometimes also be mitigated by extending the length of the preceding component which can be done if it is a guide segment.

2.6.4.5 Guides and benders

A guide is a component type that is used to control the path the neutrons travel. The inside of the guide is coated with materials that allow the neutrons to reflect dependent on the angle of incidence. The guides can be configured in a group with each guide slightly rotated versus the direction of the beam. Such a set up acts as a bender. The pseudo code as used in McStas to set up a guide component is shown in Figure 2.24.

```
COMPONENT guide5a = Bender(
        w=0.025,            // [m] Width of the bender
        h=0.065,            // [m] Height of the bender
        l = 27.840)         // [m] length of bender
        r=4500,             // [m] Radius of the bender
        Win = 0.006186667, // [radians] Angle of the deflection of the whole bender = l / r
        k = 1,              // Number of channels inside the bender
        ma = 3,             // m-value of material outer side
        mi = 3,             // m-value of material inner side
        ms = 3,             // m-value of material top and bottom side
AT (0, 0, 9.660) RELATIVE source
```

Figure 2.24: Definition of a bender component type in McStas pseudo code, including specific values for the input parameters of this component type like its dimensions and reflection/ absorption level of the walls. The name of the instance of this component is 'guide5a' and 'Bender' is its component type name. This component type can be used as often as needed in the same instrument file provided its instance name is different.

In the virtual instrument these separate guide components can be replaced by one curved guide called a bender. The curvature will match an imaginary curve through the guide segments of the real instrument. The curve is a part of a circle and the radius of the bender will be such that it matches the radius of this circle. The bender can be used to eliminate fast neutrons of the beam, these neutrons will pass through the side of the guides or bender component type dependent on their angle of incidence and the coating used on the wall of the guides or bender.

2.6.4.6 Collimators

A collimator is a component type that is used to focus the neutrons into a specific direction, to reduce divergence and improve efficiency. They can be used at different places in the instrument. They can be used to define the size of the gauge volume, this can be in combination with slits. Before setting up an experiment the appropriate gauge volume needs to be decided. Gauge volume size has a marked influence on the number of neutrons needed for a successful experiment, analogous with count time in a real instrument.

2.6.4.7 Detectors

A detector is a component type that captures the neutrons and depending on the type of detector used will provide information on the neutron in terms of scattering angle, the location where it has collided with the detector screen and how many neutrons. McStas provides a standard set of detectors but also allows to build dedicated detectors to reflect more accurately the real detectors used. In the case of a TOF instrument the detectors will capture the TOF of the neutron, the

intensity and the error in the intensity and number of neutrons reaching the detector. This information can be converted to generate a diffraction pattern and intensity profile.

2.6.4.8 Samples

The McStas software was originally developed to support the design of neutron diffraction instruments. Over time more component types have been developed that allow the modelling of samples. McStas Version 2.4 and later offer two options to model samples. The first method uses the powder component type PowderN and the single crystal component `Single_crystal`. The powder component supports only single scattering while the single crystal supports multi-scattering. These components can be used in an assembly but there are restrictions that limits what can be done. One limitation is that the components that are part of the sample are positioned and processed sequential, the other limitation arises when putting a sample component inside another, this is only possible if they are positioned concentric. These components have a number of input parameters that are used to specify the physical properties of the sample and the geometry. The basic geometries supported are cubic, spherical and cylindrical. For more complex geometries it is possible to specify a file of type PLY. Various software packages can be used to create more complex geometries in 3D and export in PLY format. The physical properties are specified using the reflections parameter. The reflection parameter uses a file of the type `laz` or `lau` as input. These files contain information like the lattice parameters, space group, density of the material and cross sections (absorption, coherent, incoherent). For many materials these files are included in the McStas distribution. If a material is used that is not covered by McStas then a `laz` or `lau` file can be generated from a `cif` file using the utility `cif2hkl` which can be downloaded from the McStas website. A `cif` file (Crystallographic Information File) can be obtained from databases like ICSD (Inorganic Crystal Structure Database). In McStas the same component type can be used multiple times as long as it has a unique reference name. This can be used to model the interface between two different materials by defining for each material a powder sample component with its own physical properties. The powder sample component also has a concentric option. This feature can be used to put a component inside another component. This allows the simulation of a powder sample contained inside a hull or a single crystal positioned in the centre of a cylindrical powder sample. A second method that can be used to model samples is the union concept. The union concept uses a materials definition section which is placed at the start of the instrument and defines the physical properties of each material using the `reflections` parameter and defines the parameters that control the scattering processes. The sample is modelled using the `Union_box`, `Union_cylinder` and `Union_sphere` component types and is no longer constrained by sequential and concentric positioning and components inside the sample assembly may overlap. To ensure overlapping components are processed correctly by McStas a parameter `priority` is specified for each component. The union also supports multiple scattering

and generates as part of the processing a history file of the scattering which can be used to verify the sample works correctly. A hypothetical example of a sample assembly is illustrated in Figure 2.25 together with a snapshot of the content of the history file.

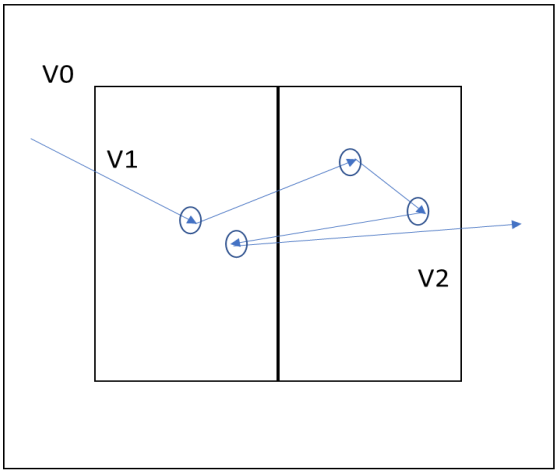

Example content of union history file

Description of the used volumes & scattering processes

V0: Surrounding vacuum

V1: sample1 Material: material1 P0: Process Incoherent

V2: sample2 Material: material2 P1: Process Coherent

Histories sorted after intensity

Intensity	Neutron path	#Neutrons
1.58E+02	V0 -> V1 -> V0	68284
2.51E+01	V0 -> V1 -> P0 -> V0 24928	24928
1.98E+00	V0 -> V1 -> P0 -> P1 -> V0	5754
1.77E+00	V0 -> V1 -> P1 -> V2 -> V0	10
1.46E-01	V0 -> V1 -> P1 -> V2 -> P0 ->P1 ->V1 ->P1 ->V2 ->V0	

Figure 2.25: The LHS shows a simple interface between two cubes (V1 & V2) with V0 the surrounding vacuum and a neutron scattered multiple times while passing through. The RHS shows a snapshot of a union history file listing the different paths taken by neutrons through the samples and ranked by intensity and number of neutrons.

The final part of the union is the `Union_master` component type. This component type is placed after the last component that makes up the sample assembly. The `Union_master` does not refer to this last component but to the arm component at the start of the sample section. The `Union_master` starts a new Monte-Carlo simulation specific for the sample assembly and controls this.

2.6.5 Neutron scattering inside sample

To explain and interpret the results of the simulations it is important to understand how McsStas handles neutron scattering inside a sample[70]. Within a sample the incident beam is attenuated due to scattering and absorption. This causes significant variation in illumination(intensity) throughout the sample. In analytical treatments attenuation can be difficult to handle and as consequence often ignored by making a thin sample approximation. In Monte Carlo Simulations the beam attenuation can be handled relatively simple. If the absorption cross section per unit cell is σ_c^a and the scattering cross section σ_c^s then the linear attenuation coefficients (inverse penetration lengths) are defined as $\mu^a = \sigma_c^a/V_c$ respectively $\mu^s = \sigma_c^s/V_c$ where V_c is the volume of the unit cell. The path length the neutron travels within the sample is made up of path length l_1 before scattering and path length l_2 after scattering. The attenuation along this path can then be expressed as:

$$f_{att}(l) = f_{att}(0)e^{-l(\mu^a+\mu^s)} \tag{2.6.2}$$

Where $l = l_1 + l_2$ and $f_{att}(0)$ a normalisation constant which can be set to 1.

The probability for a neutron ray to be scattered from within the interval $[l_1, l_1 + dl]$ will be

$$P(l_1)dl = \mu^s f_{att}(l_1)dl \tag{2.6.3}$$

While the probability for a neutron to be scattered from within this interval into the solid angle Ω and not being scattered further or absorbed on the way out of the sample is

$$P(l_1, \Omega)dld\Omega = \mu^s f_{att}(l_1) f_{att}(l_2)\gamma(\Omega)dld\Omega \tag{2.6.4}$$

Where $\gamma(\Omega)$ is the directional distribution of the scattered neutrons and l_2 is determined by Monte Carlo choices of l_1 and Ω, and from the sample geometry. (Insert a pictorial of a neutron ray passing through a sample and getting scattered. This is important for the explanation of the drop off in intensity when bank is in reflection mode).

A possible choice for the scattering depth l_1 could be from a flat distribution in $[0, l_{full}]$ where l_{full} is the path length of a neutron travelling through the sample without scattering. Choosing the directional dependence from $g(\Omega)$, we have a Monte Carlo probability

$$f(l_1, \Omega) = {g(\Omega)}\Big/{l_{full}} \tag{2.6.5}$$

The neutron weight factor is now adjusted by the amount

$$\pi_i(l_1, \Omega) = \mu^s l_{full} e^{-(l_1+l_2)(\mu^a+\mu^s)} \frac{\gamma(\Omega)}{g(\Omega)} \tag{2.6.6}$$

This explanation omits multiple scattering where a neutron is scattered multiple times before leaving the sample. Multiple scattering is included in the single crystal component, the polycrystalline component and the union concept but not in the powder component.

2.6.6 Implementing McStas or equivalent software

McStas software can run on different operating systems. Operating systems supported are Windows, Linux and Mac OS. The Linux version of McStas can run on a PC and on High Performance Computers (HPC). Installation on a PC is straight forward using the instructions provided. Installing on a HPC will normally be done by the systems administrator of the HPC. When designing new instruments or modifying existing ones the PC version is preferable as it allows 2D and 3D visualisation of the instrument. This is the best way to verify if the components are in the correct positions and if the neutron rays can reach the detectors. Particularly when performing a scan it is important to verify the sample is moving correctly through the beam. Simulations can be done using a PC but when large numbers of scans with multiple scan points are required then it is recommended to copy the instrument on to a HPC. To run the simulation on an HPC a shell script needs to be written that specifies the parameters and instrument to be used. As part of this research several shell scripts have been written. In addition to the methods described for improving the performance of the simulations, McStas also offers the capability to run in parallel mode. This is possible because there is no relationship between the simulations of the neutron histories. In

practice the McStas software in conjunction with the operating system of the HPC takes care of this provided the right compilation and execution commands are included in the shell script. The shell script allows to specify the number of the processors required and the amount of time they will be needed for. To determine how many neutron histories are needed to ensure an adequate number of neutrons reach the detector a calibration simulation is performed. In a calibration simulation the same number of neutron histories is simulated for each scan. This simulation provides the intensity at each scan point and the number of neutrons that reached the detector. This information is then used to adjust the number of neutron histories for each scan point. The neutron histories used for this research project varied between 1e9 and 1e12. The higher end of the range is needed when running with smaller gauge volumes.

2.7 Reported McStas work

The McStas software has been used intensively for optimization and background characterisation when designing neutron diffraction instruments. The type of instruments designed are wide ranging and McStas is used by many institutes around the world as reported in the literature [71]–[75][76][77][78]. The following is an example of what can be done with McStas. McStas was used to build a virtual model of the cold triple axis spectrometer RITA-II at Paul Scherrer Institute , Switzerland with the aim to develop a new data analysis method[79]. To validate the McStas model of the instrument a set of virtual experiments were performed and the simulated results compared against experimental data. The virtual model of the RITA-II instrument excluding the guide system and the simulation results for one of the virtual experiments are shown in Figure 2.26. This virtual experiment shows the simulated image at the sample position, the beam divergence and a comparison of the diffraction pattern between simulation and experiment.

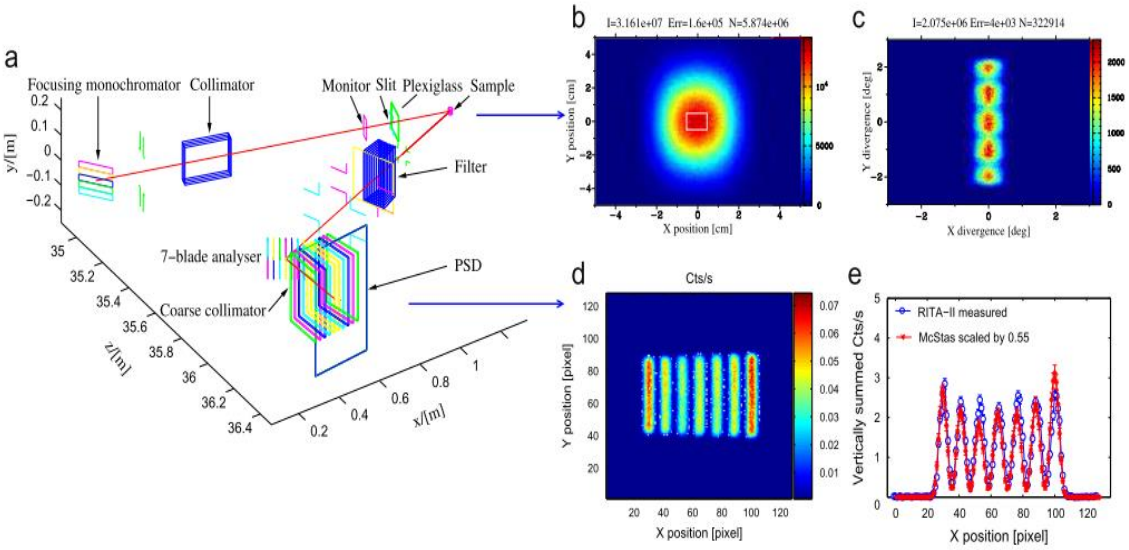

Figure 2.26: (a) The virtual RITA-II instrument in McStas. The guide system is not shown. The simulated image at the sample position is shown in (b) with the central 1 cm^2 marked by a white box the divergence of which is shown in (c), both using wavelengths between 3.84 and 4.25 Å for the source, vertically focussing monochromator and a 40' linear collimator before the sample position. A vanadium sample is inserted in the instrument and (d) shows the simulated pattern on the 2D PSD. Figure (e) shows the vertically collapsed simulated (*-red) and measured (o-blue) pattern. Both (d) and (e) clearly show the seven analyser blades of RITA-II in the monochromatic dispersive (imaging) model[79].

Although McStas is used for studying residual stress/strain in relation to instrument and component design[80], no evidence has been found in the existing literature that McStas has been used to study pseudo strain.

2.8 Performing virtual experiments

A virtual experiment requires a model and simulation of all aspects of the experimental setup. In the case of neutron diffraction experiments a model of the instrument and a model of the sample is required. McStas has its own pseudo-code language that is used to specify the components, default values for the input parameters and their position relative to the origin of the instrument. The instrument model and its input parameters are for the main part fixed apart from parameter settings for certain components like slits and collimators. The sample however will be modelled according to the specific aspects the virtual experiment is aiming to study. The sample can be a simple cube but can also consist of an assembly of components to model more complex geometries. For basic geometries like a cube, cylinder and sphere standard sample component types like `PowderN` and `Single_crystal` are available in the McStas library. To model more complex geometries involving multiple components like in an interface the union component types like `Union_box` or `Union_cylinder` should be used. The result of the modelling is an instrument file. To use this instrument file in a simulation the pseudo code in this file needs to be converted to a

lower level computer language which is done using a pre-compiler. This pre-compiler translates the pseudo-code into C/C++, these are lower level computer languages. Output of the pre-compilation is a file containing C/C++ instructions. This file is then compiled using a C-compiler to generate an executable file. This file is then used in the simulation. To run a simulation a shell script is needed. A shell script contains instructions on how many processors are needed to run the simulation, an estimate of the expected runtime, the instrument executable to use and all necessary input parameters for the instrument. The shell script can be modified to meet more complex simulation scenarios and made specific for an instrument as will be discussed later. The most common input parameters for the instrument relate to slit settings and collimator settings which are used to control the shape and direction of the beam and define the size of the instrument gauge volume (IGV) to be used. For the sample the most common parameters are the dimensions, the density, the physical properties of the materials used and the angle under which the sample will traverse the beam during a scan. The detectors used in the instrument are usually bespoke for a given instrument but all have in common that they generate an output file containing data that can be converted in a diffraction pattern. The processing and analysis of this data requires usually software that is specific for the instrument modelled.

2.9 Summary

Joining components is a common requirement in engineering. A method often used for joining components in nuclear power plants and aircraft engines is welding. An area of particular interest is dissimilar material welds. The nature of the welding process using high temperatures in a small area followed by cooling leads to build up of residual stresses. Both nuclear power plants and aircraft engines are subject to stringent safety procedures and standards. It is therefore very important to accurately measure the residual stress in such welds in order to predict how the weld will perform over its lifetime. Residual stress can be measured with destructive and non-destructive methods such as neutron diffraction. Neutron diffraction is an established method in the nuclear industry.

The characteristics of neutrons make them well suited for measuring residual stress in materials using neutron diffraction due to their high penetration and applicable wavelengths to engineering alloys. In certain type of residual stress measurements using neutron diffraction, errors can arise due to the geometry of instrument and sample. This is the case in near surface strain measurements, which can be interpreted as an air to material interface, at the joint between two dissimilar materials, which can be interpreted as a material to material interface and when measurements are made in regions with a lack of uniformity in terms of diffracting material. Such as in the presence of voids, defects and disproportionately large grains, like those found in the vicinity of welds. In each of these measurements the vital assumption of a uniform filled GV is

broken leading to a shift of the centre of the gauge volume and a peak shift in the diffraction pattern. If ignored these shifts in peak manifest as a change in the measured lattice parameter and ultimately a change in the measured strain. Therefore, these errors will be referred to as pseudo strains in this dissertation.

Techniques have been developed to mitigate for errors associated with nonuniform gauge volume filling, however these cannot always be applied due to geometric constrains and can be instrument specific. To perform strain measurements requires beam time which is in finite supply and has a significant cost which is generally prioritised for structural integrity measurements with little devoted to instrument analysis. To obtain a better understanding of pseudo strain computer simulation of neutron diffraction using Monte Carlo method is proposed. There are several software packages available that offer this capability. For this research project McStas has been chosen. McStas is a neutron ray tracing software package with neutron diffraction Monte Carlo method embedded. The instrument and samples modelled using McStas are an approximation of the real instrument and sample. The instrument modelled in this research project is ENGIN-X a TOF instrument located at ISIS(RAL). The Monte Carlo method simulation offers the possibility to study pseudo strains in a more cost-effective manner. It allows to perform simulations of scenarios that with a real instrument would not be possible due to limited availability of beam time and the cost.

The virtual experiments done with McStas as part of this research focus on prediction of intensities and its capability to model instruments and samples, its ability to predict precise differences in lattice parameter necessary for strain measurement is not yet studied.

3 Design and validation of a new ENGINX McStas model

3.1 Introduction and motivation

As stated earlier, several of the decisions made early on in this project were based on the pragmatic reasoning that a model of ENGINX, the time of flight neutron diffraction instrument located at ISIS(RAL), already existed in McStas. The virtual model of ENGINX was designed and built in 2006 and used for the initial feasibility studies and virtual experiments. Inspection of this virtual model along with comparison of virtual experiments with those from equivalent experiments done using the real ENGINX instrument indicated that the 2006 model had been produced applying several extensive simplifications. Although adequate for the purpose of instrument realisation and flux optimisation experiments, when modelling the subtle shifts in diffraction peak it was decided that a complete redesign of the virtual instrument model from scratch using architectural drawings as shown in Figure 3.1, was essential. The new model built as part of this research program was built in 2017 and will be referred to explicitly as “the 2017 model” to distinguish it from “the 2006 model” to avoid confusion. In this chapter the evaluation of the two models along with a detailed description of how the 2017 has been updated to minimise the usability and susceptibility to human error by allowing dynamic selection of collimator size and reading input parameters from script file to allow for complex multi-dimensional simulations in an efficient manner and probably most importantly for future application of the model using a scripting style familiar with ENGINX users.

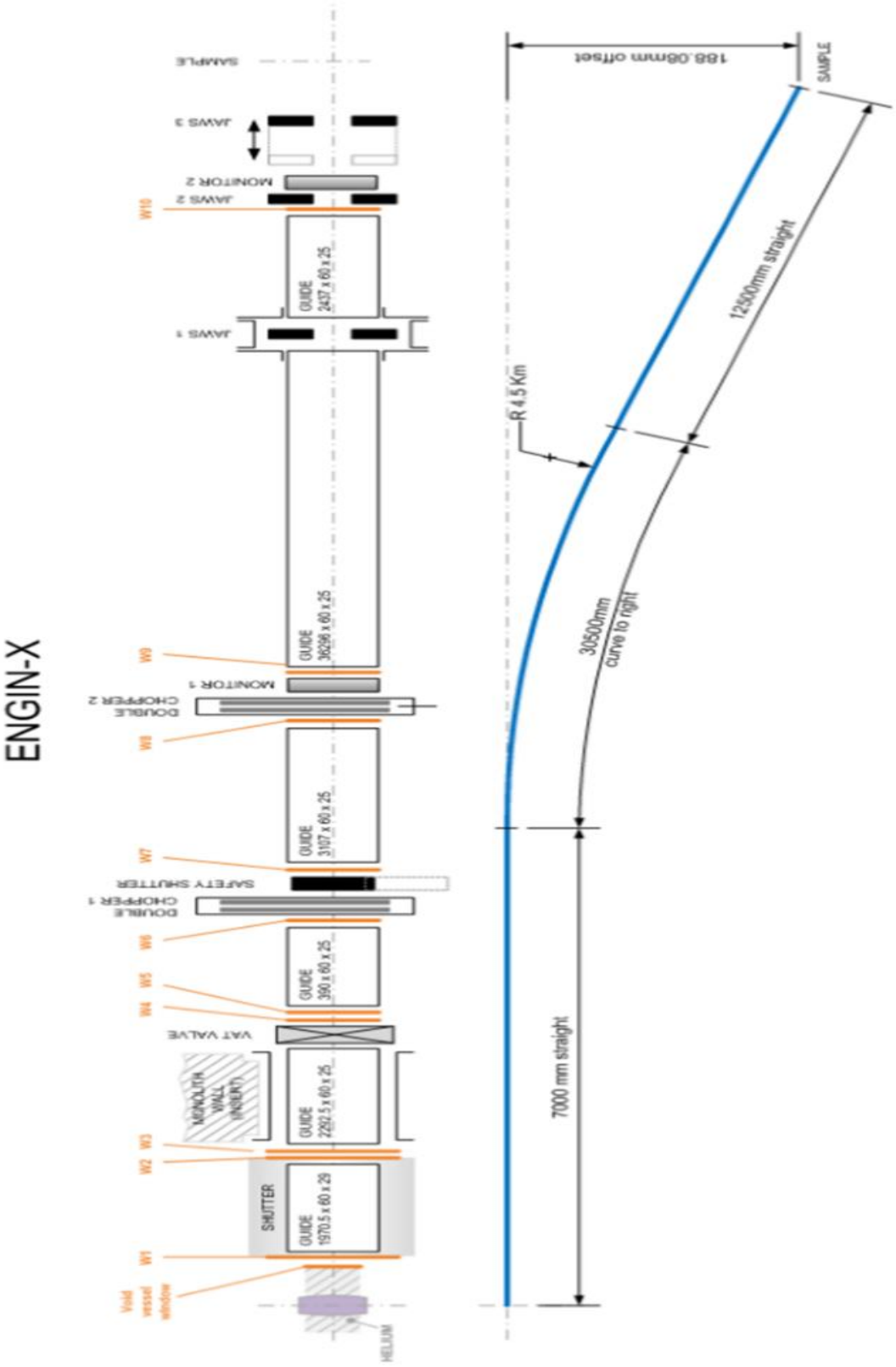

Figure 3.1: Architectural drawing of ENGIN-X and the curvature of the guide system(Source: Francesco Zuddas (ISIS)).

3.2 Design of virtual instrument in McStas

3.2.1 Definition of coordinate systems

Before designing and building a virtual model of an instrument it is very important to verify the definition of the axes used in the real instrument and the ones used by McStas. The definition of the instrument axes in ENGINX differ from those in McStas. In ENGINX the incoming beam is parallel to the y-axis while in McStas the beam is parallel to the z-axis. The x-axis orientation is the same for both and runs parallel with an imaginary line connecting the detector banks. In the real ENGINX instrument the z-axis is de vertical axis which is perpendicular to the beam and the x, y plane while in McStas the vertical axis is the y-axis which is perpendicular to the beam and to the x, z plane. The instrument coordinate systems for ENGINX and McStas are illustrated in Figure 3.2.

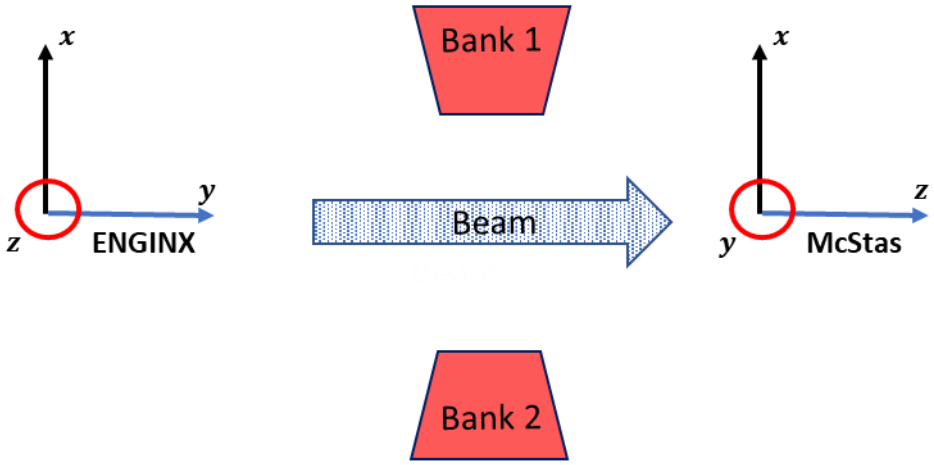

Figure 3.2: Definition of axes of instrument coordinate system in McStas and ENGIN-X

The instrument coordinate system is not the only coordinate system used in McStas. Components like samples have their own coordinate system. This becomes apparent when performing sample scans where the sample may be rotated and translated. To prevent unexpected behaviour the "`arm`" component can be used to fix a new coordinate system. In the virtual model of ENGINX usually two `arm` components are used to control the movement of the sample and to ensure that other components that do not move as part of a scan stay in their fixed positions.

To facilitate the building of new instruments or changing of existing instruments two utilities are available. The `mcdisplay` utility provides a 2D view of the instrument and is very useful to check if the components are in the correct position relative to each other and to verify a sample is crossing the beam correctly during a scan. The `mcdisplay-webgl` provides a 3D view in which neutrons can be simulated which show up as rays travelling through the instrument.

3.2.2 Component types used in ENGIN-X

The virtual model of ENGIN-X is uses both standard and bespoke component types. The standard ones were described as part of the general discussion of McStas. Here the bespoke component types will be discussed in more detail. In Table 3.1 all the component types used in the virtual model of ENGIN-X are listed. McStas offers the possibility to add various monitors at different positions in the instrument. These are mainly used to validate that certain aspects of the instrument work as anticipated and are usually deactivated once instrument is working correctly. Some monitors also exist in the real instrument, these have been included in Table 3.1.

Table 3.1: Component types used in virtual McStas model of ENGIN-X

Component Type	Component type name	Number of instances in ENGIN-X	Purpose
Progress bar	Progress_bar	1	Collect statistics of simulation
Moderator	ISIS_moderator	1	Generate neutron histories used in simulation
Slit	Slit	4	Controls shape and size of the beam
Bender	Bender	2	Curved guide removes fast neutrons from beam
Guide	Guide	4	Controls the beam direction, shape and size. Can have different geometries ie elliptical, rectangular
Chopper	DiskChopper	2	Circular shape, rotates at specific frequency
Monitor	PSD_monitor	2	Positional specific divergence monitor, to collect beam statistics
Arm	Arm	2	Used to fix coordinate system and to control rotations and translations of the sample assembly
Powder sample	PowderN	[1, N]	Used to model a powder sample, supports only single scattering
Single crystal sample	Single_crystal	[0, N]	Can be used to model a grain, supports multi-scattering
Union box sample	Union_box	[1, N]	Can be used to model rectangular shaped sample components, supports multi-scattering
Union cylinder sample	Union_cylinder	[0, N]	Can be used to model cylindrical shaped components, supports multi-scattering
Union master	Union_master	1	Controls the Monte-Carlo simulation of the sample assembly
Collimator	Exact_radial_coll	2	Controls beam shape, size and direction
Detector	TOFLog_spher	2	Collects the neutrons scattered by sample and generates output file with intensity and number of neutrons as function of TOF

The sections of the moderator, guide system, collimator and detectors are fixed but their parameter settings may be adjusted depending on the experiment. The sample is the part of the instrument that changes with each experiment and the virtual model of the samples will be discussed in detail for each experiment.

3.2.2.1 Source and moderator

To generate neutron histories in the virtual instrument a component is needed that is the equivalent of the neutron source and moderator in the real ENGIN-X instrument. For ENGINX a bespoke moderator component is used called `ISIS_moderator`. This component is positioned immediately at the start of the instrument just after the progress bar component. The `ISIS_moderator` component defines the range of wave lengths the generated neutrons will have, the dimensions of the moderator, the focussing rectangle and the type of moderator to use. The wavelength range is specified using two parameters, `Emin` for lower end of the energy range and `Emax` for the upper end of the range. The dimension of the moderator can be directly specified using the `x-width` and `y-height` parameters or if set to -1 default values will be used. The default option was used for all the simulations performed in the context of this research. The focussing rectangle can be specified using `focus_xwidth` and `focus_yheight` parameters. It is important that the focussing rectangle dimension is chosen such that it matches the entrance of the first section of the guide system. A focussing rectangle that is too large means the beam diverges too much and not enough neutrons will be available for simulation. The moderator type to use is specified using files which hold the definitions of the moderator to use e.g. “water”, “CH4”, graphite etc.

3.2.2.2 Guides and benders

The guide system of ENGINX is made up of 4 rectangular guide components, 2 benders, 2 choppers, 2 monitors and 4 slits. These are all standard components available in McStas with their parameters set to reflect the real ENGINX instrument. Where virtual components do not have the same dimensions as the equivalent real components, gaps are introduced so that the neutron flight path still matches the flight path of the neutrons in the real instrument.

3.2.2.3 Samples

The sample can be made up of one component or an assembly of components. In the real ENGINX the sample is mounted on a rig which itself is fixed on a table that can rotate and translate. In the McStas virtual model of the instrument this table is not present, but all the necessary rotations and translations can be achieved using `arm` components and the option to specify a translation or rotation at each component.

3.2.2.4 Collimators

To focus the diffracted beam ENGIN-X uses two collimators which are positioned under an angle of 90 degrees with the beam. These collimators are represented in the virtual model by the `exact_radial_coll` component type. The `exact_radial_coll` is based on a Soller collimator and is a bespoke component. The ENGINX instrument has multiple sets of collimators to allow gauge volumes of 0.5, 1, 2, 3 and 4 mm. In practice this means that the collimators need to be swapped if a different gauge volume is needed. In the 2006 model an equivalent operation would have been needed by swapping the relevant code. In the 2017 model new functionality has been coded which allows the collimator to be dynamically assigned and avoids the need for swapping code in the instrument when a different gauge volume is needed. The selection of the gauge volume can be passed on as a parameter in the script file. This makes it possible to run a series of simulations using the same sample set up but different collimator settings. This allows users of the ENGIN-X instrument to do an assessment of the impact of using different gauge volumes on their experiment. This kind of functionality reduces the impact of human error.

3.2.2.5 Detectors

The 2006 instrument model allowed only the simulation of detector bank 1 using the contributed component called `TOFLog_spher`. The code of this component has been re-written and in the 2017 model it is now possible to also simulate detector bank 2 as well. This is an important enhancement as it allows to study the effect on the pseudo strain dependent on whether a bank is in transmission or reflection mode which will be explained in detail when discussing the results of the experiments. The terminology of transmission and reflection mode needs to be defined in the context of the type of experiment that will be performed. In the case of an air to material scan, a detector is deemed to be in transmission mode when the neutrons pass through the sample before reaching a detector, and is in reflection mode when the neutrons enter the sample but do not pass through the sample before reaching a detector as illustrated in Figure 3.3.

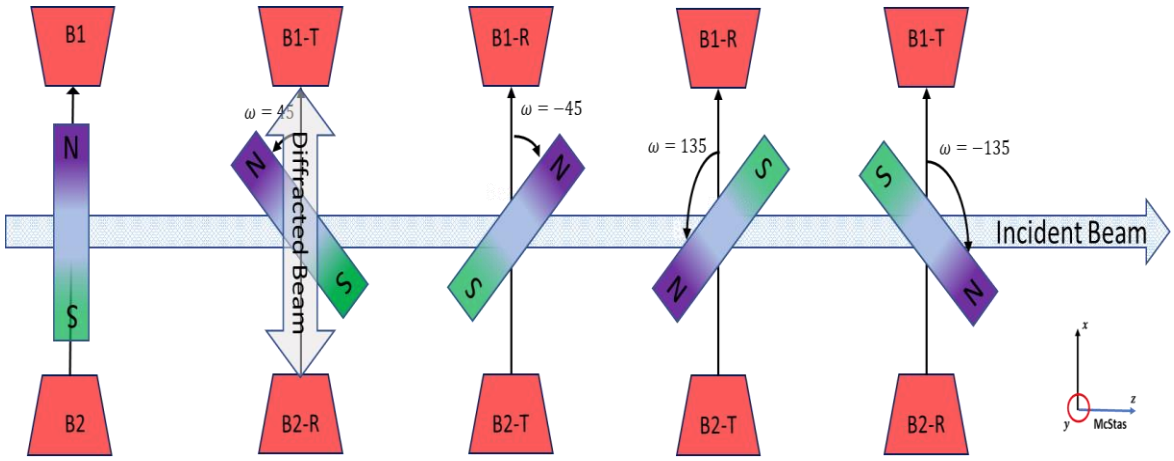

Figure 3.3: Depending on orientation of sample a detector is either in transmission or in reflection mode (sample colouring to facilitate observation of sample rotation only).

The terms B1 and B2 are abbreviations and refer to detector bank1 and detector bank 2, respectively. The capital letter R stands for Reflection and T for transmission, so B1-T means bank is in transmission mode and B2-R means bank 2 is in reflection mode. These abbreviations will be used in figures and tables when applicable. The rotation angle ω is the angle of rotation about the y-axis in the McStas coordinate system. When describing rotations in virtual experiments then this is the angle referred to.

3.3 Comparison of the 2006 and 2017 models

The initial simulations were done using a McStas model of ENGINX built in 2006. The results of these initial simulations when compared with the experimental data suggested that this model may not be sufficient accurate/correct. In 2017 the model of 2006 was compared with up to date architectural documents of the real ENGINX instrument which revealed that several components were missing from the instrument model and that some of the parameter settings of the moderator did not reflect the settings of the real instrument. This investigation led to the decision to build a new instrument model of ENGINX from scratch. A schematic comparison between the 2006 and the new 2017 model is shown in Figure 3.4.

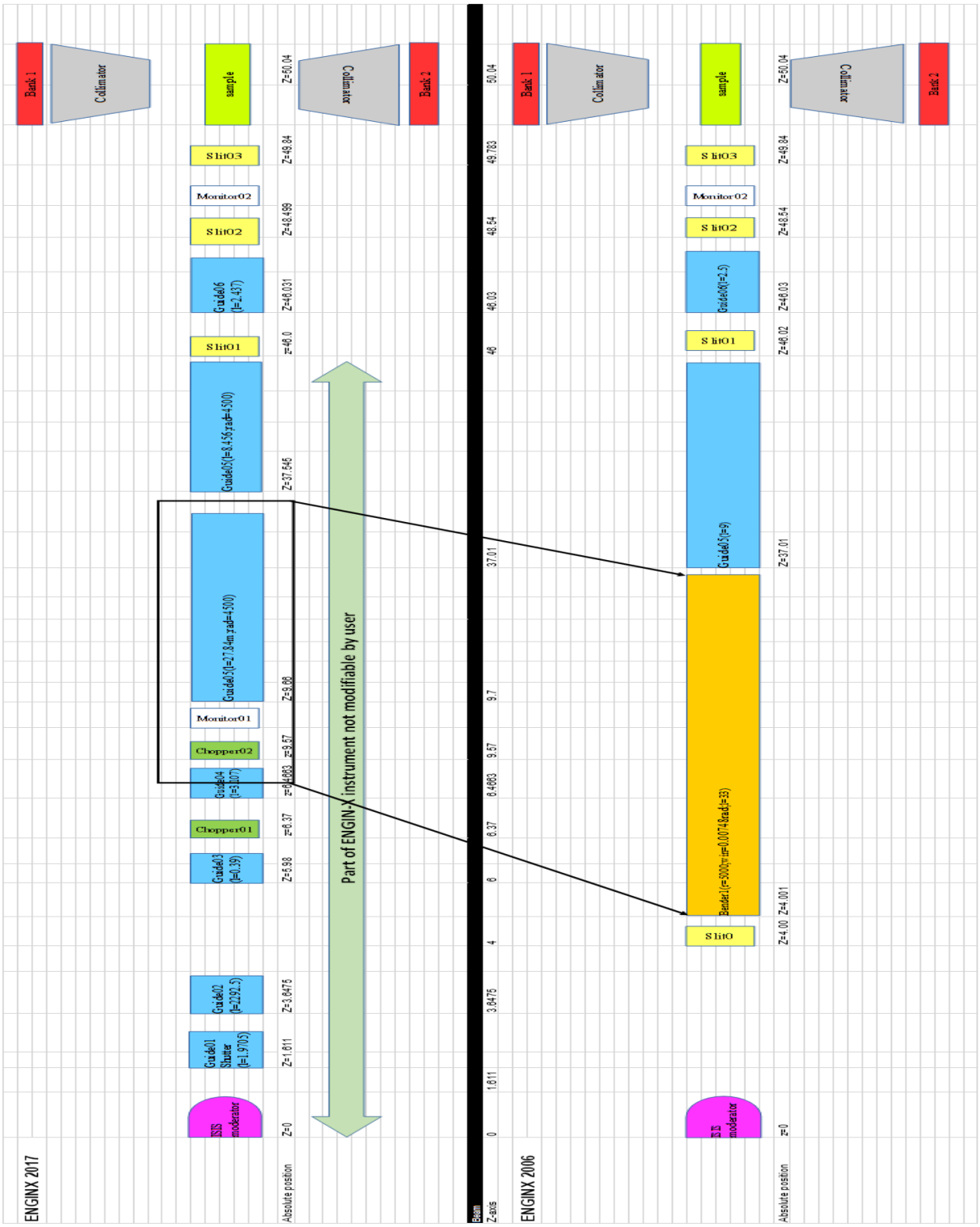

Figure 3.4: A schematic comparison between the 2006 model and the 2017 model of ENGINX in McStas.

A snapshot of the ENGINX instrument using the 3D visualisation provided by McStas is shown in Figure 3.5. The view seen here is from sample perspective. The 3D utility allows run real time simulations showing the neutron rays as they travel through instrument and get scattered of the sample before reaching the detectors.

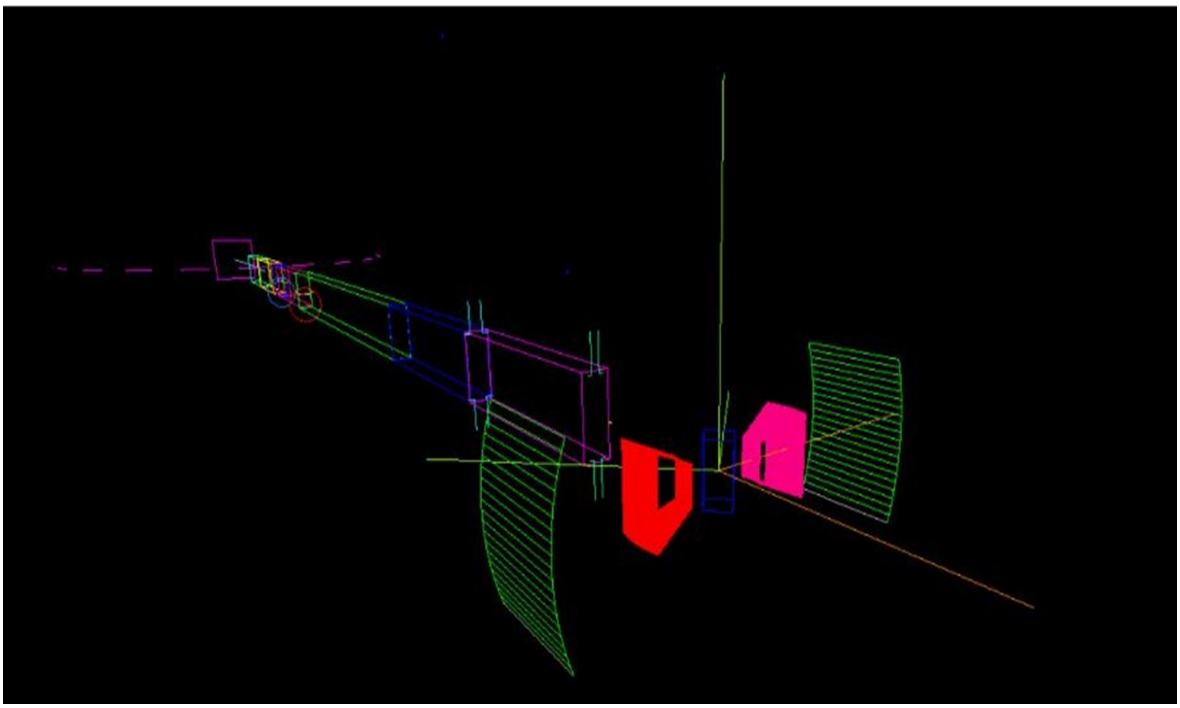

Figure 3.5: A 3D presentation of ENGIN-X instrument seen from the sample (blue cube) between the red and pink coloured collimators. The grids in green colour represent the detectors modelled as spherical. The 3D display capability in conjunction with 2D display are used intensively to model instruments, samples and scan scenarios.

When compared to Figure 3.1 it is clear the discrepancies between the 2006 model and the actual instrument. The reason that components were left out of the model is most likely due to limitations of the available computer capacity at the time of the design in 2006 and that the model was built for testing the instrument design rather than sample models. Based on these observations it was decided to build a new model from scratch.

3.4 Running a McStas simulation of ENGINX

An instrument can be simulated interactively using the Windows GUI interface that comes standard with McStas. This is very useful capability when designing and modifying instruments and samples. When building a new instrument, modifying one or testing a scan it can be useful to add additional monitors to the instrument that can capture specific statistics of the beam and neutrons. McStas offer a range of monitors and it is possible to build one from scratch. The monitors do not influence neutrons travelling through the instrument, intensities and neutrons reaching the detectors are not affected. An instrument like ENGINX has for each component many input parameters. For the majority of the users these parameters will not change when performing measurements. The parameters that are likely to change are sample dimensions, physical properties of the material, gauge volume orientation of the sample and its position during the scan. For strain measurements the sample traverses the beam. To make a simulation like this a script file similar to the real ENGINX instrument

must be created which specifies as a minimum the run number, sample positions, sample rotation angles and the number of neutrons. It is possible to add more parameters such as collimator size, slit opening dimensions, detector and materials to use. The number of neutrons to use requires a calibration run in which for all sample positions the same number of neutrons is used, usually 1e8 neutrons is a good start. The results of this scan need to be analysed in terms of intensities and number of neutrons that reached the detector. If the number of neutrons is too low it will be difficult if not impossible to fit the diffraction pattern data using OpenGenie. As a rule of thumb about 200000 neutrons per scan point reaching the detector will be sufficient and the fitting error will normally between 20 to 50 με. The shell script developed to run the simulations can be run on a PC using Linux, however for most simulations a HPC will be required to obtain good results in an acceptable time frame. The majority of simulations conducted in this dissertation have been run using anywhere up to 1024 CPU cores using the full parallel capabilities of McStas and the ISIS HPC facility.

3.5 Data analysis

The results of the experiments were analysed using `OpenGenie`. `OpenGenie` is a GUI based software package that is built on top of GSAS which is used to perform peak fitting on the ENGINX instrument. The new McStas 2017 model contains code so that the data files are formatted, named and numbered in such a way that they can be read and processed directly in `OpenGenie` by a procedure called `mcstas_enginx`. This procedure converts the McStas output files to files that have the same layout as the files produced by ENGINX so that the same fitting procedures can be used for both experimental as well as simulated data. Depending the type of experiment and data to analyse different options are available in `OpenGenie`. For the analysis the Pawley method, single peak fit and multi-phase fitting has been used.

The work in this thesis has focused on simulation of neutron diffraction rather than data analysis and therefore a concerted effort has been made to keep all data analysis as consistent with the analysis protocols currently used on the instrument as possible.

3.6 Methodology

3.6.1 Characterization of beam and gauge volume

To characterize the beam in terms of divergence, intensity spread and gauge volume size and shape an experiment was performed at ENGINX using a scan of an annealed steel pin. In this experiment an annealed steel pin traversed across the beam along the axis between the detector banks as shown in Figure 3.6.

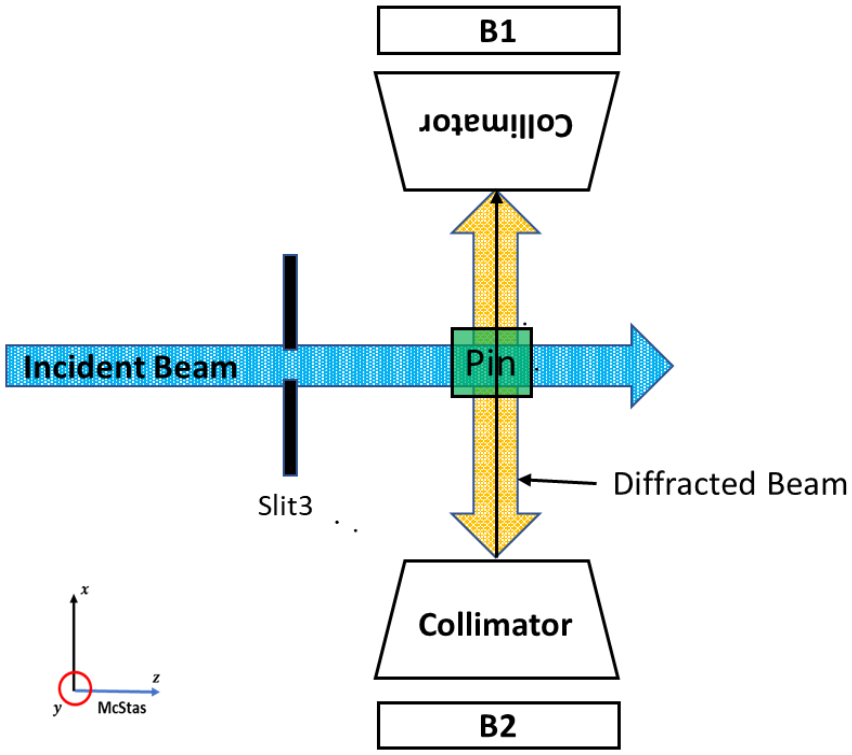

Figure 3.6: Set up sample steel pin experiment, sample is not rotated.

The pin was made of ferritic steel in the shape of a rod with dimensions 1x20x1 mm. A 4mm gauge volume was used and the scan started at -2.5mm from the centre of the IGV. The scan consisted of 11 scan points going from -2.5mm to +2.5mm in steps of 0.5mm. A second scan was performed where the pin was moved along the beam. The starting position of this scan was -3.5 mm of the centre of the IGV and comprises of 15 scan points going from -3.5mm to +3.5mm in steps of 0.5mm. Both experiments were simulated in McStas using the 2006 and the 2017 model with the sample modelled as a powder component using the component type PowderN. In addition, further simulations were done to get a more detailed understanding of the impact on the results when using different collimators and by shifting slit 3 in horizontal direction. The collimators used were 2 and 4mm. The position of slit 3 was shifted in steps of 0.1 mm from -0.2mm to 0.4mm in a direction that is parallel to the axis between the detectors while keeping the opening the same. To assess the impact on the pseudo strain and intensity a simulation was performed in which the steel pin was fixed at the centre of the IGV and the vertical opening of slit3 was varied between 5 and 30mm in steps of 5mm. To obtain information on intensity and strain across the IGV a grid scan simulation was performed for a 2mm GV whereby the steel pin was moved in steps of 0.25 mm in the xz plane with $y = 0$ and x and z between -2.5 and 2.5 mm, and for a 4mm in steps of 0.5mm in the xz plane with $y = 0$ and x and z between -4 and 4mm. In later chapters where more complex sample assemblies are needed a sample type referred to as Union_box is used. Therefore, to determine the appropriateness or interchanging between sample types a second model of the sample was built using the Union_box and a simulation

was performed to verify that the union gives the same results. The key parameters for the different experiments and simulations are shown in Table 3.2. The coordinate references used are based on the McStas definition of the instrument and sample coordinate systems. It is important to note that the sample coordinate system is no longer aligned with the instrument coordinate system when the sample is rotated as is the case in most of the experiments described in this dissertation.

Table 3.2: Experiments and simulations performed using an annealed steel pin

Description	IGV	ω	Jaws3 x-pos range, step size mm	Scan range, step size mm	Total scan points	Scope
Scan across beam	4	0	[0,0,0]	$x[-2.5,2.5,0.5]$	11	Virtual/ Exp
Scan along beam	4	0	[0,0,0]	$y[-3.5,3.5,0.5]$	14	Virtual/ Exp
Scan across beam	2,4	0	[-0.2,0.4,0.1]	$x[-2.5,2.5,0.5]$	231	Virtual
Vary slit3 vertical	4	0	[0,0,0]	$x = 0;$ $slit3V[5,30,5]]$	6	Virtual
Grid scan	2	-45	[0,0,0]	$(x,y)[-2.5,2.5,0.25]$	441	Virtual
Grid scan	4	-45	[0,0,0]	$(\boldsymbol{x},\boldsymbol{y})[-\mathbf{4},\mathbf{4},\mathbf{0.5}]$	289	Virtual

3.7 Performing real and virtual experiments

In preparation of the real experiment on ENGINX several procedures may need to be performed, such as calibration of detector banks and the positioning and alignment of the sample. The calibration is done at the start of a beam cycle but may need to be repeated if there is a change in the instrument. The positioning and alignment are done at the start of each experiment and may need to be repeated if changes are made to the instrument like swapping the radial collimators. In McStas there is no need for the calibration of the detectors as the instrument components do not undergo physical changes due to operation or environment and are identical to the geometry of the specification (ie they do not contain manufacturing tolerances). On the other hand, the accurate positioning of the sample in the virtual instrument is as important as in the real instrument and therefore position verifications similar to those done on a real instrument are a good idea. McStas offers several utilities to verify the sample

is positioned correctly relative to the beam as well as the other components in the instrument. To perform a scan in McStas a script file similar to the one used in the real experiment is created or for a simple single measurement a command line command similar to that on the real instrument (all be it with different syntax) can be submitted.

3.7.1 Calibration of detector banks

To calibrate the detectors a scan is performed using a reference sample made of Cerium in the shape of a pin. The purpose of this scan is to determine the `difc`, `difa` and `zero` coefficients. The outcome of this exercise results in the 'PAR' files which are used in the fitting routines of Open Genie and GSAS. This scan is done at the beginning of the beam cycle and takes about 12 hours. The calibration may need to be done again if the instrument undergoes significant physical changes. In practice the result of one calibration scan is used for multiple experiments. For McStas the PAR files were obtained by a different iterative process. The `difc`, `difa` and `zero` were given initial values taken from a PAR file generated as part of a calibration of ENGINX. Then in an iterative process the initial values were changed stepwise and for each set the fitting results were compared with the experimental ones. The experimental data used were taken from the scan of the annealed steel pin. As each bank has its own PAR file with different values for the `difc`, `difa` and zero coefficients this process has been followed for each bank. The virtual instrument and its components are not subject to external influences, hence the `difc`, `difa` and `zero` coefficients used do not change, and for the fitting of McStas data always the same PAR files are used.

3.7.2 Sample positioning and alignment

The samples used in experiments on ENGINX are mounted on a rig and the rig itself is mounted on top of the positioning table, referred to as the positioner. The positioner lies beyond slit 3 and is a motorized table which 3 orthogonal translational axes and 3 rotational axes. Samples are accurately aligned using the positioner and theodolite which is positioned under a nominal angle of $\pm 45^{o}$ with the incident beam. A detailed description of this manual procedure can be found in the ENGINX user manual. This procedure is performed twice with the sample rotated 180^{o} the second time. The outcome of this exercise are two sets of values for x and y which are used to calculate an average value. These average values determine how much the positioner needs to be shifted so that the sample and the beam align correctly. To verify the positioning and alignment is correct a short scan using a reference sample is performed to determine the intensity profiles in x and y direction. The shape of the intensity profiles is used to verify the reference sample is aligned correctly versus the beam. The intensity should be at a maximum when the centre of the sample coincides with the centre of the IGV. If this is not the case the procedure is repeated. The average values obtained for x and y using this procedure are then used to adjust the scan positions used in the experiment.

In McStas there is no equivalent for the positioner and the theodolite because the sample can in theory be positioned at any location in any orientation. To verify the sample is positioned correctly McStas provides several software utilities to visualise the instrument components relative to each other in 2 and 3 dimensions. The same utilities also allow the visualisation of neutron rays travelling through the instrument. The geometry of the sample set up in ENGINX may require the sample to move up or downward before rotating or translating it in order to avoid the sample colliding with the slit or other part of the instrument. To some extent this is also a problem in McStas although there would not be physical damage to the instrument if components overlap but it could give the wrong results or worse the program could crash.

3.7.3 Defining the scan script

To run a scan for an experiment on ENGINX a script file needs to be created. This file contains for each scan point the x, y and z positions, the angle of rotation ω, and the number of microamps to use. The microamps determine how much time per scan point will be used. The larger the number of microamps used the more neutrons will be used, and higher quality spectra can be expected. After a certain number of microamps the benefit of using more becomes marginal. To establish how many micro amps to use per point one can take one scan point and repeat the scan with increasing number of micro amps. The error for each measurement can then be plotted versus the micro amps to determine the optimum value as illustrated for bank 1 in **Error! Reference source not found.**.

Figure 3.7: Increasing the number of microamps initially lowers the error in the measurement but the law of diminishing returns applies. The plot shown was obtained using a nickel powder cube and performing a measurement at the same point gradually increasing the micro amps. When approaching 35 amps the error is no longer getting smaller but stays between 40 and 50με.

The scan in McStas uses a similar script file but with some differences. The first difference is that the script file allocates to each scan point a run number which is used to generate the name of output file

containing the diffraction data. This makes it possible to get the same file names for scan positions that are identical in the experiment and the simulation which with the number of measurements often made in an experiment, is a valuable auditing tool. The second difference relates to the neutrons used per scan point. In the ENGINX script file the number of micro amps per scan point is used for this. In the McStas script file the micro amps are replaced with the number of neutron histories to simulate for a specific scan point. The McStas script also offers the capability to add for each scan point additional parameters. These are parameters that are used as input on the relevant components like collimator settings, slit opening or which detector to use. To determine an appropriate number of neutron histories to use for each scan point a calibration process is used. This process starts with doing a scan for all the scan positions using the same number of neutron histories for each scan point. McStas produces an output file containing the intensity for each scan point and the number of neutrons reaching the detector bank. A fit is then performed for the scan points using `OpenGenie` to determine how many neutron histories are needed so that the fitting error is less than ~20με. Where the fitting error is larger the number of neutron histories for this scan point will be increased. The increase can be calculated relative to the number of neutron histories used for a scan point that has a fitting error < 20με. The McStas script is not a standard capability of McStas but has been developed separately using `bash` shell scripting for this project. This is also the point to be aware that the definitions of the axes in McStas are different from those used for ENGINX. For a z-scan in ENGINX the sample is moved along the z-axis while in McStas this would be along the y-axis.

3.8 Treatment of measurement and simulation data

The diffraction data from the experiment and simulations are both analysed using the Pawley refinement method. The Pawley method uses the spectrum of the stress-free material supplemented with physical properties of the material and mathematical techniques like the least square method to perform a fitting of the diffraction data. This results in a new diffraction pattern in which peaks will be slightly shifted when compared with the diffraction pattern of the stress-free material. When the fit involves multiphase materials or different materials the method works as long as the peaks of the different materials are not overlapping. Overlapping peaks occur when the lattice parameters of the different materials are very close in magnitude and structure factors are similar. The contribution to the pseudo strain of each material can be determined by this method.

3.8.1 Uncertainty in the results

To assess how good the experimental and simulation data are, two types of uncertainties (errors) are taken into account. The first uncertainty is the fitting error which depends on how many neutrons are used when scanning a specific sample position. The larger the number of neutrons reaching the

sample the more neutrons will be scattered and a higher probability that more will reach the detectors. For the experiment the number of neutrons used is calculated as the flux of the neutron beam multiplied by the scan time for a particular sample position and for the simulation this is the number of neutron histories simulated for a particular sample position. The second uncertainty originates from the way the pseudo strain is calculated. The calculation of the pseudo strain uses the lattice parameter of the stress-free material. This value can be chosen in different ways partially dependent on the geometry of the sample and type of scan. The pseudo strain error is then calculated using an error propagation method[81] of the form:

$$\Delta z = \sqrt{\left(\frac{\partial z}{\partial x}\Delta x\right)^2 + \left(\frac{\partial z}{\partial y}\Delta y\right)^2} \tag{3.8.1}$$

where z is a function of x and y and Δx and Δy are the uncertainties in x and y. The uncertainty in a strain component ε_{xx}(say) is therefore

$$\Delta\varepsilon_{xx} = \sqrt{\left(\frac{\partial \varepsilon_{xx}}{\partial a_{xx}}\Delta a_{xx}\right)^2 + \left(\frac{\partial \varepsilon_{xx}}{\partial a_0}\Delta a_0\right)^2} \tag{3.8.2}$$

where a_0 is the lattice parameter for strain free sample at position $x = 0$, and a_{xx} is the lattice parameter for the same strain free sample but now positioned at a position x. In a normal strain measurement a_0 will be the unstressed lattice parameter. The lattice parameters are output from the Rietveld refinement method based on the statistical fit of the peak. The uncertainties in a_0 and a_{xx} are represented, respectively, by Δa_0 and Δa_{xx} and are the fitting errors taken from the HDF output file. Equation (3.8.2) may be written as

$$\Delta\varepsilon_{xx} = \frac{a_{xx}}{a_0}\sqrt{\left(\frac{\Delta a_{xx}}{a_{xx}}\right)^2 + \left(\frac{\Delta a_0}{a_0}\right)^2} \tag{3.8.3}$$

3.9 Results – Gauge volume characterisation

The results of the scan of the annealed steel pin across the beam are shown in Figure 3.8 for bank 1 and in for bank 2. For bank 1 the results of the experiment are compared with the simulations done using the 2006 and 2017 McStas model. In all cases the strain calculated on the LHS increase up to ~900 at -2.5mm and becomes increasingly negative on the RHS. On the LHS side of the plot there is a good fit between the experiment and both McStas models, on the RHS however the fit is less good with the ENGINX results being more negative for all measurement locations. The RHS shows that the 2017 model results in a better fit than the 2006 model although there is still a

discrepancy reaching a maximum difference of ~200με at sample position 1.5mm. The error varies between ±30 and ±70με for the ENGINX experiment and between ±20 to ±50με for the simulated data.

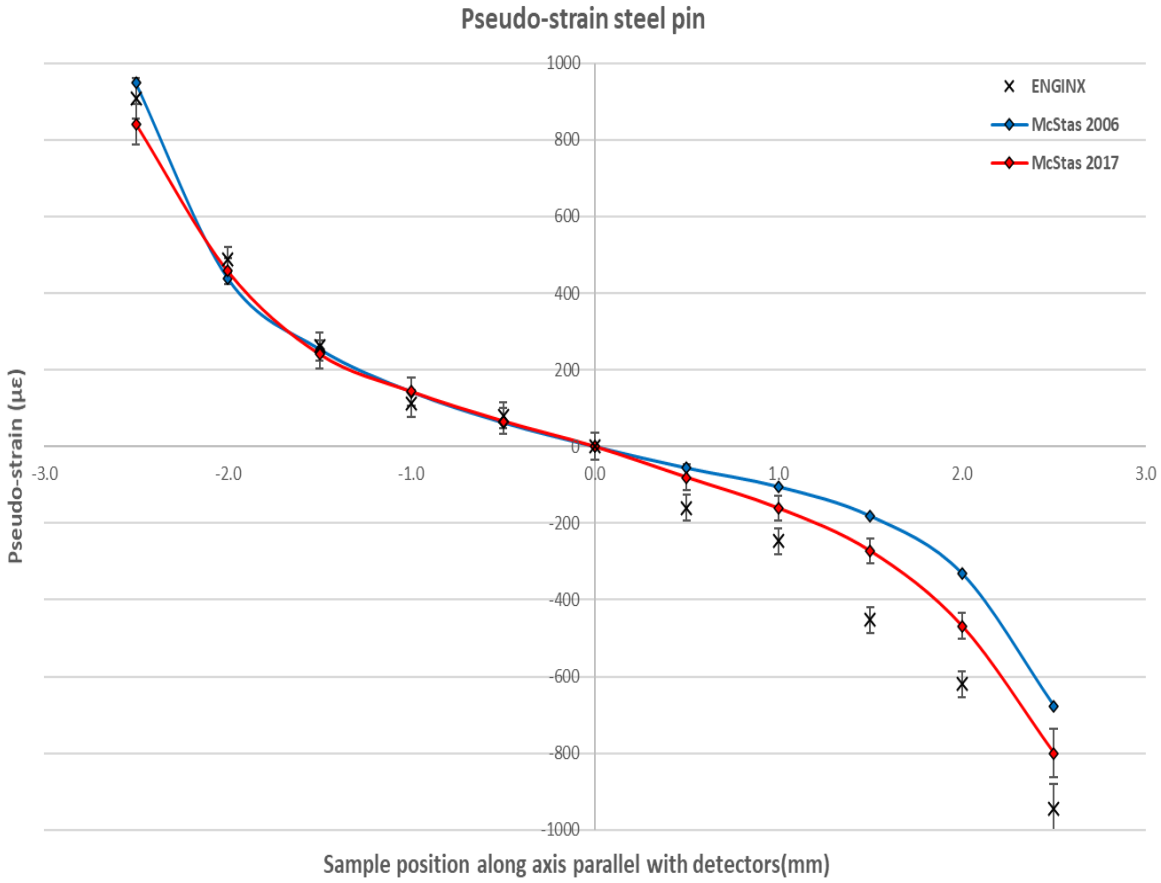

Figure 3.8: Pseudo strain bank 1 as measured on ENGINX and simulated using 2006 and 2017 model for an annealed steel pin (1x20x11mm) with a GV of 4mm. For sample positions less than 0 there is a good fit, for sample positions larger than 0 the 2017 model gives a better fit than the 2006 model but there is still a difference reaching a maximum of ~200με at 1.5mm.

Pseudo strain bank 2 as measured on ENGINX and simulated using 2017 model for an annealed steel pin (1x20x11mm) with a GV of 4mm is shown in Figure 3.9. For sample positions less than 0 there is a good fit, for sample positions larger than 0 there is a difference reaching a maximum of ~200με at 2mm.

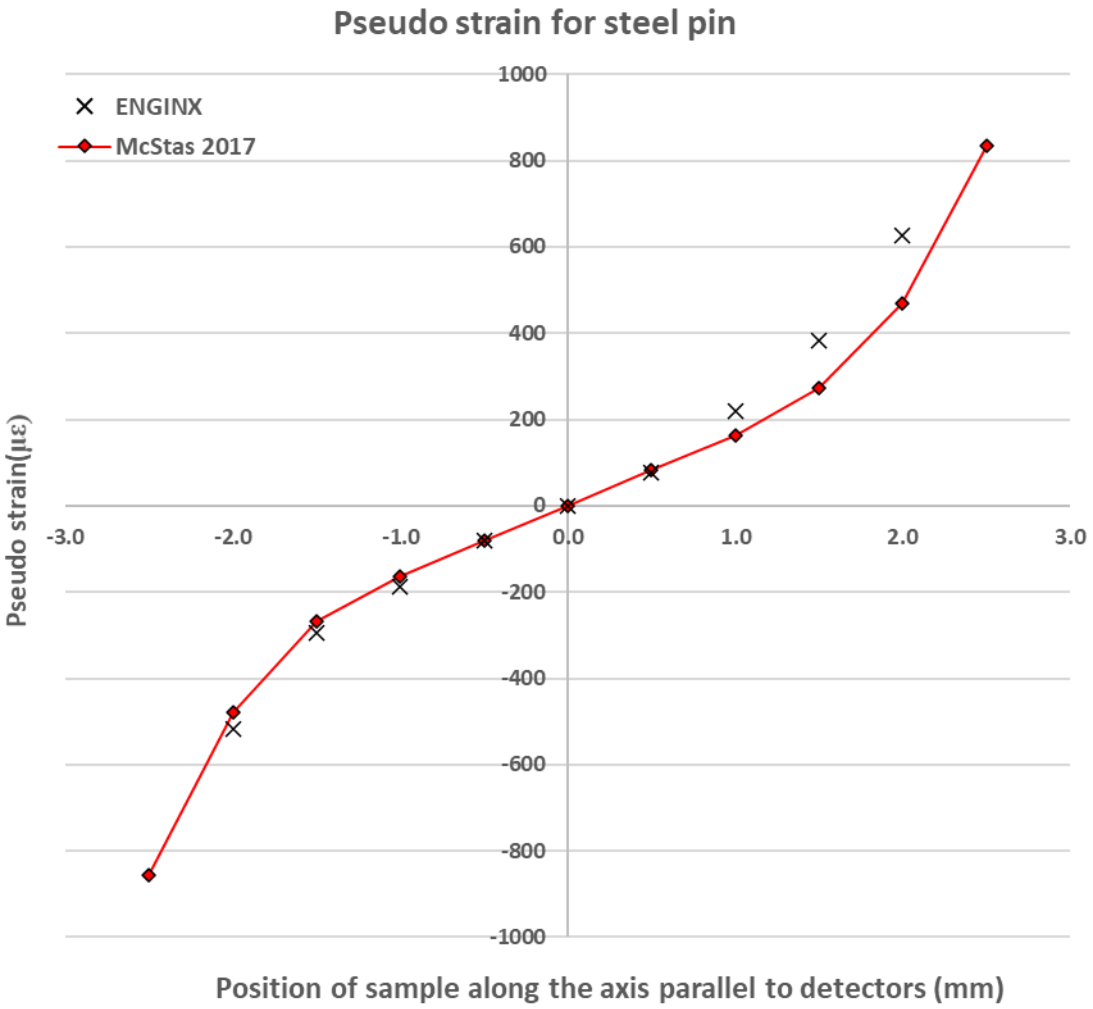

Figure 3.9: Pseudo strain bank 2 as measured on ENGINX and simulated using 2017 model for an annealed steel pin (1x20x11mm) with a GV of 4mm. For sample positions less than 0 there is a good fit, for sample positions larger than 0 there is a difference reaching a maximum of ~200με at 2mm.

Part of the reason that the 2017 model gives a better fit may be found in the intensity profile of the beam as shown in Figure 4.2. The intensity of the beam in the 2017 model stays more or less constant for sample positon between -1.5 and 1.5 mm. The intensity of the beam in the 2006 model drops off when the sample position is greater than -0.5mm and the real ENGINX instrument drops off when sample position is greater than 0 but to a lesser extent. The drop off is not caused by attenuation as the sample is only 1x1 mm.

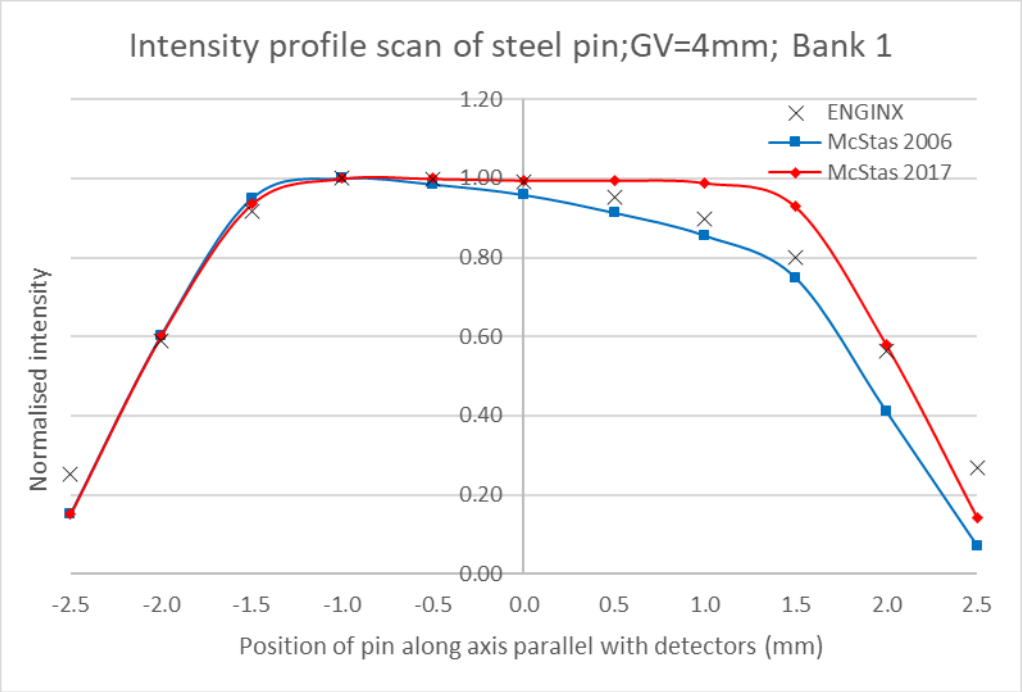

Figure 3.10: Normalised intensity of beam in experiment vs simulations

In Fig 4.3 a comparison of the divergence of the beam is made between the 2006 model and the 2017 model. To generate this diagram a divergence position monitor was placed at the centre of the IGV. The 2006 model shows gaps in the beam divergence profile which could lead to inhomogeneous distribution of the neutrons in SGV and a shift of the NCOG away from the geometric centre of the IGV. The 2017 model does not have those gaps as would be expected in reality. The divergence diagram is generated using a Position Sensitive Detector (PSD) at the position of the sample. The diagram is a cross section of the beam at the sample position. The boundaries of the beam can be adjusted and the window can be rotated so it does not show a rectangular but a diamond shape.

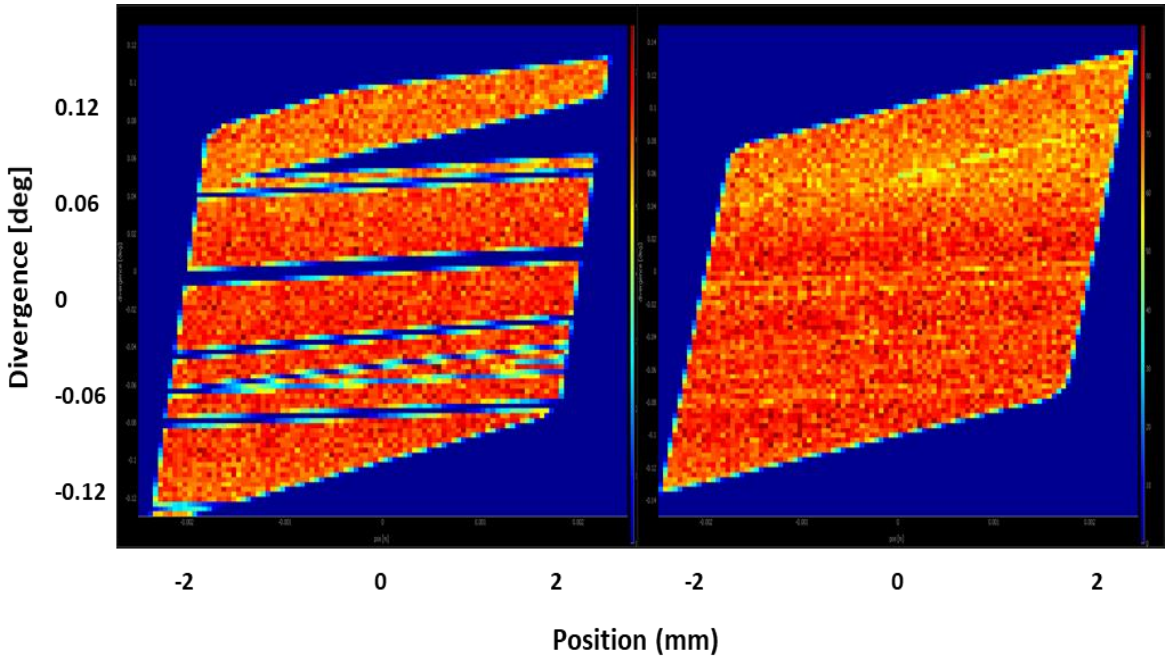

Figure 3.11: The positional divergence diagram of the beam for the 2006 model (left) and for the 2017 model (right). The colours indicate the neutron intensity. The dark blue stripes In the 2006 beam indicate that there are no neutrons and leads to a non-uniform distribution of neutrons in the sample volume.

Although the 2017 model gives pseudo strain results that are closer to the results of the ENGINX experiment there is still a gap for pin positions larger than zero. To investigate this further a comparison of the peak shapes for pin positions at -2, -1.5, 0, 1,5 and 2mm was made. The peak chosen for the comparison corresponds with $d_{211} = 1.1782\text{Å}$. The results are shown in Figure 3.12 and Figure 3.13. The top row in each table shows the pin position. The second row shows the peak shapes in black for the ENGINX experiment. The third row shows the peak shapes in red for the McStas simulation. In the fourth row the peaks are put on top of each other. The horizontal axis represents the d-spacing. In row two and three the vertical axis represents the neutron count. In the fourth row the vertical axis represents a normalised neutron count.

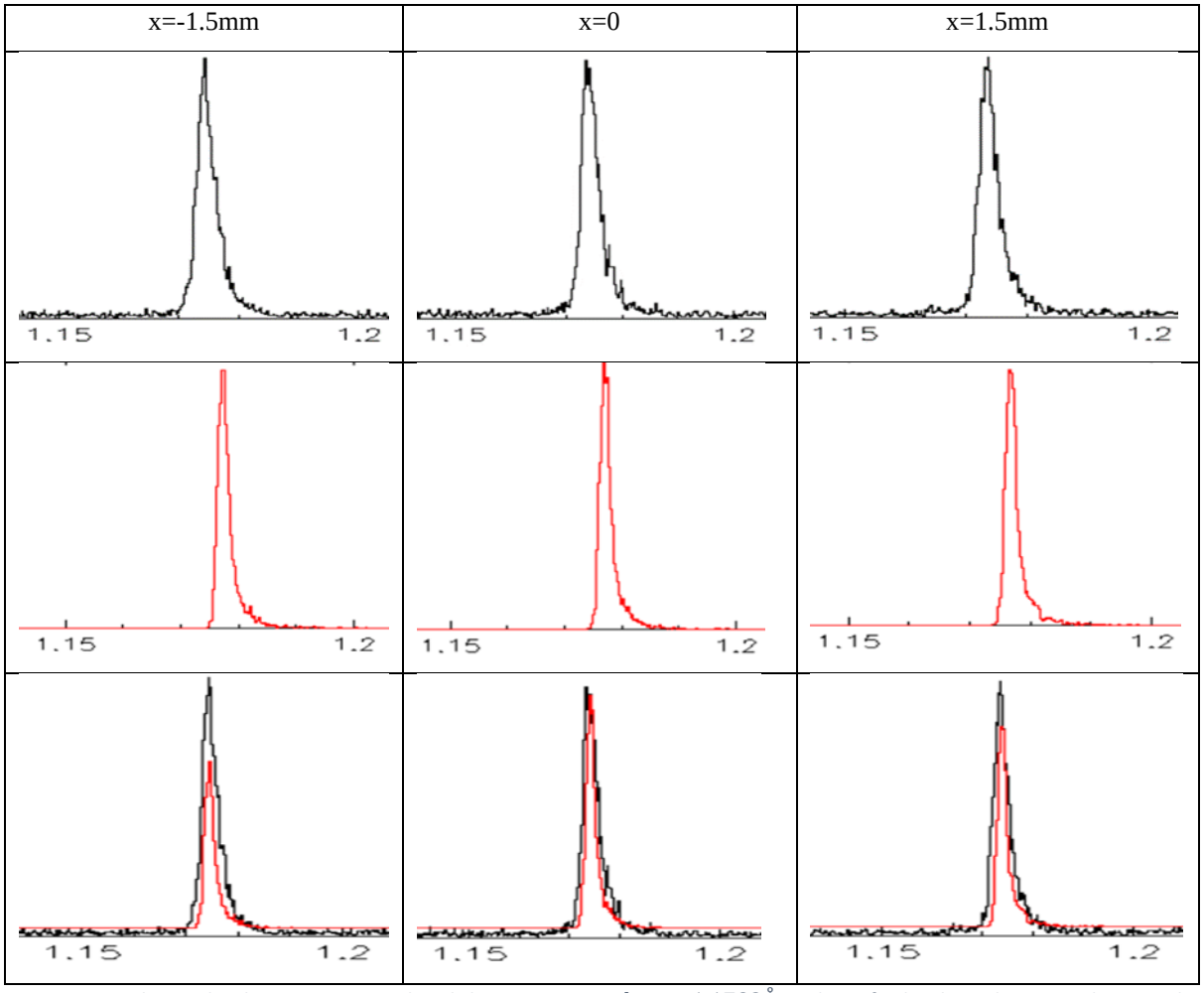

Figure 3.12: The peaks shown correspond with lattice spacing $d_{211} = 1.1782$Å and are for bank 1. The vertical axis is the neutron count and the horizontal axis is the lattice spacing. The pin positions are shown in the top row. The second row show the peak shapes for the ENGINX experiment. The third row shows the peak shapes for the McStas simulation using the 2017 model. In the fourth row the peaks have been put on top of each other and shows there is no difference of significance between the peak shapes of the experiment and the simulation.

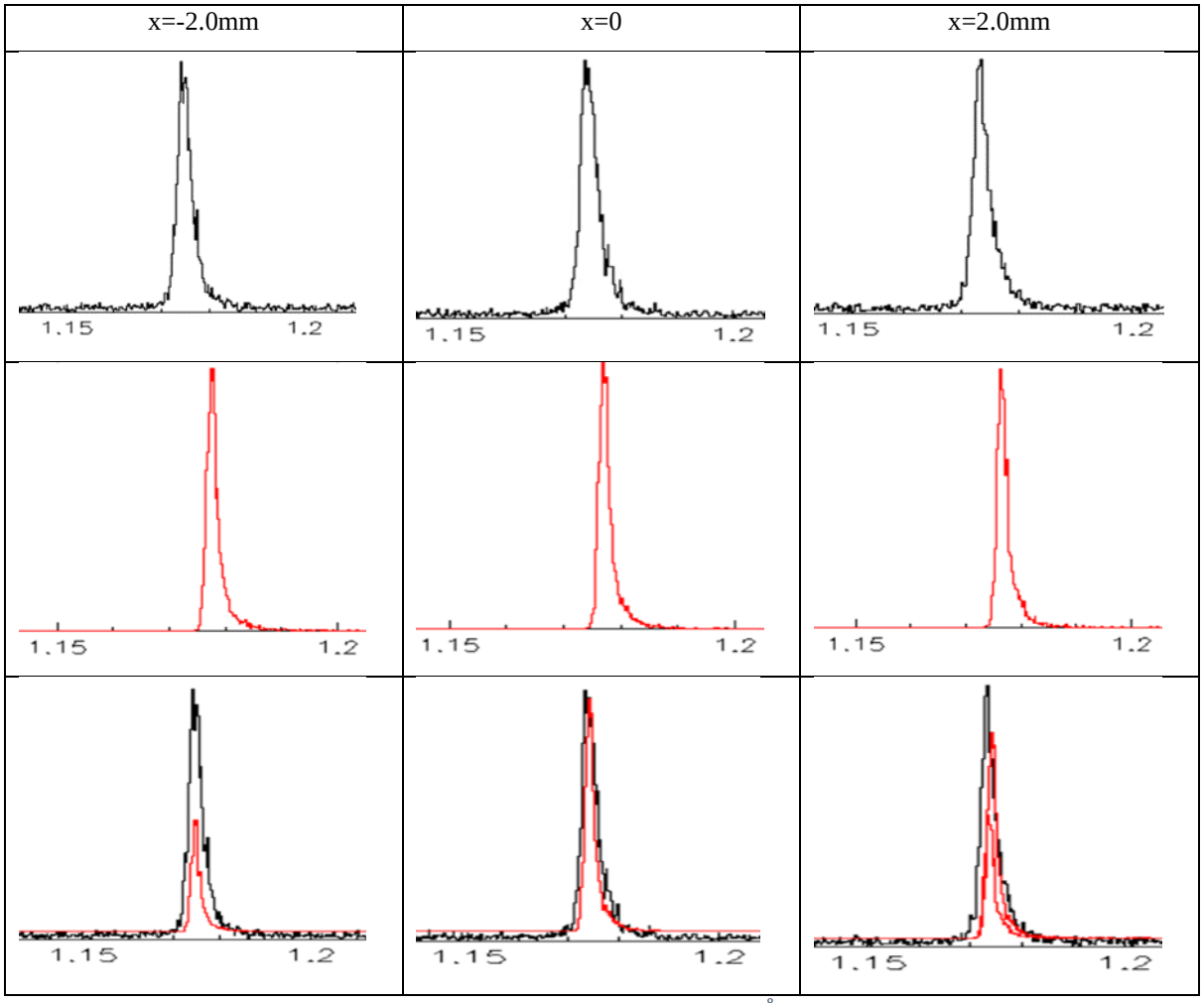

Figure 3.13: The peaks shown correspond with lattice spacing $d_{211} = 1.1782\text{Å}$ and are for bank 1. The vertical axis is the neutron count and the horizontal axis is the lattice spacing. The pin positions are shown in the top row. The second row show the peak shapes in black for the ENGINX experiment. The third row shows the peak shapes in red for the McStas simulation using the 2017 model. In the fourth row the peaks have been put on top of each other and shows there is no difference of significance between the peak shapes of the experiment and the simulation.

The results of the scan of the annealed steel pin along the beam are shown in Figure 3.14. In this case there is a good match between the experiment and the simulations for both models. This is supported by the intensity profiles shown in Figure 3.15 that are for both models identical and symmetrical. The gauge volume during the scan goes from not/ partial immersed to fully immersed and then again partial /not immersed. The shape of the gauge volume stays cuboid which explains the linear form of the pseudo strain curve.

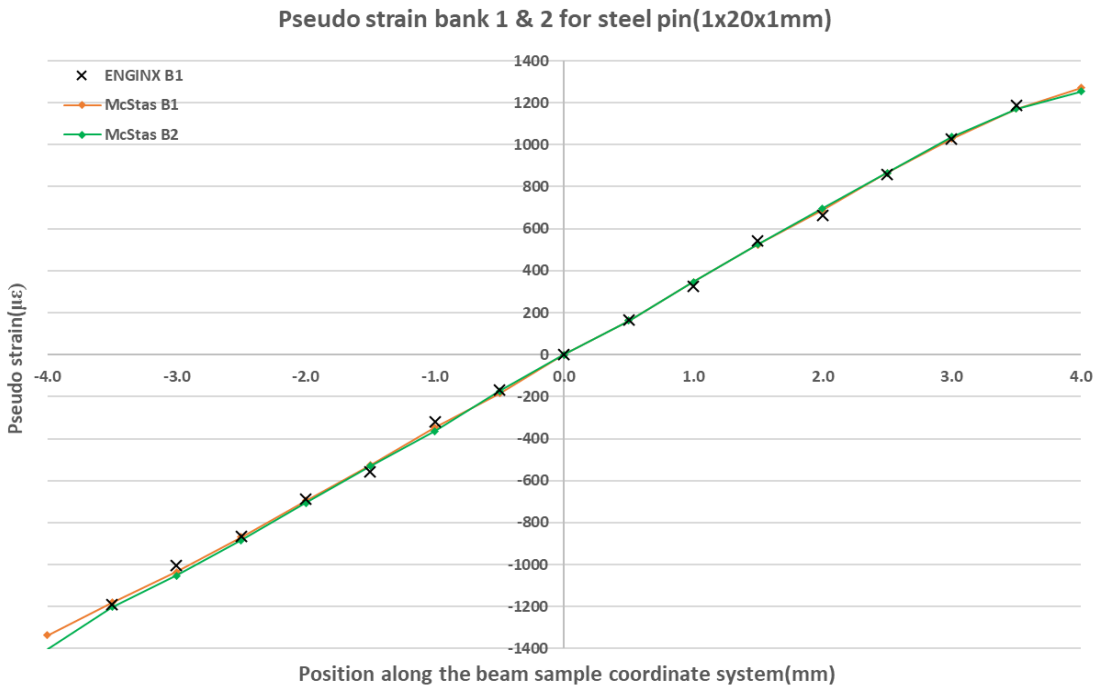

Figure 3.14: Pseudo strain measured in experiment, compared against simulations using 2006 and 2017 model.

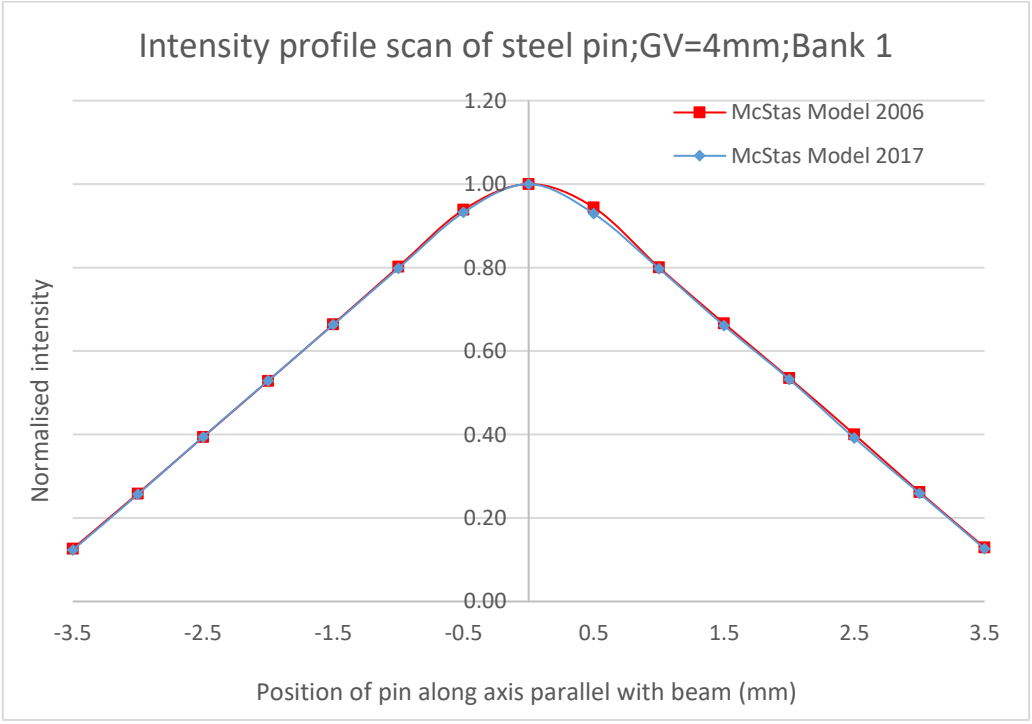

Figure 3.15: Normalised intensity profile bank 1 for scan of a cube along the beam for 2006 and 2017 instrument model.

To assess the impact of the opening of slit3 in the vertical direction a number of simulations were performed were the steel pin was kept at position 0 while varying the height of slit3. The results for the intensity are shown in Figure 3.16. For height between 5 and 20mm the intensity increases for

heights larger than 20mm the intensity stays the same. The lattice parameter for each of the heights (not shown) was determined but there was no noticeable shift.

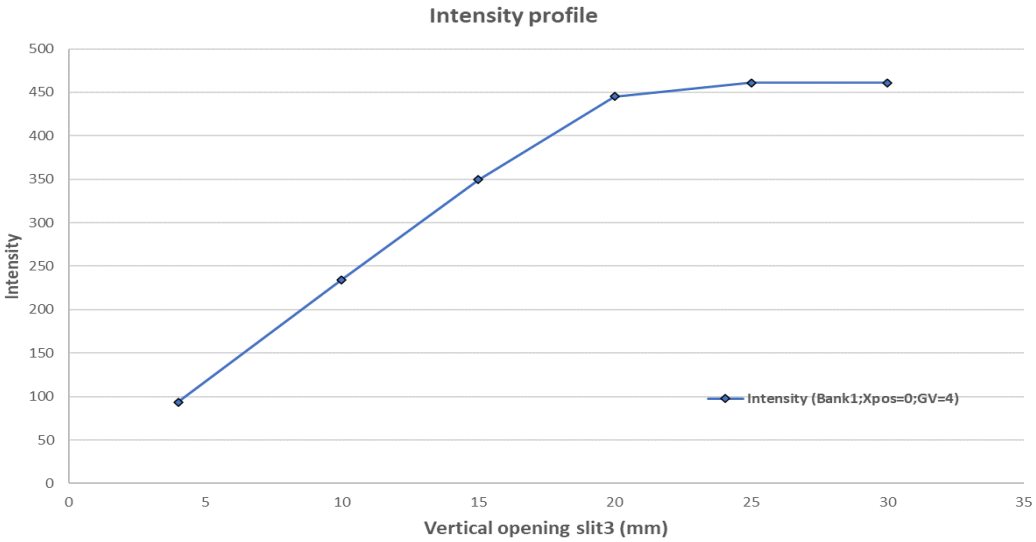

Figure 3.16: Intensity profile bank 1 for steel pin at position 0 with the height of slit3 varying between 5 and 30 mm in steps of 5mm. The GV used is 4mm. For height between 5 and 20mm the intensity increases for heights larger than 20mm the intensity stays the same.

The pseudo strain when shifting slit3 in horizontal direction is shown in Figure 3.17. To keep the plot readable only the most relevant are shown. Moving slit3 horizontally shows that the curves shift with the effect that for a shift of -0.2 mm the curve matches ENGINX for sample position greater than 0 but for sample positions less than 0 the curves diverge.

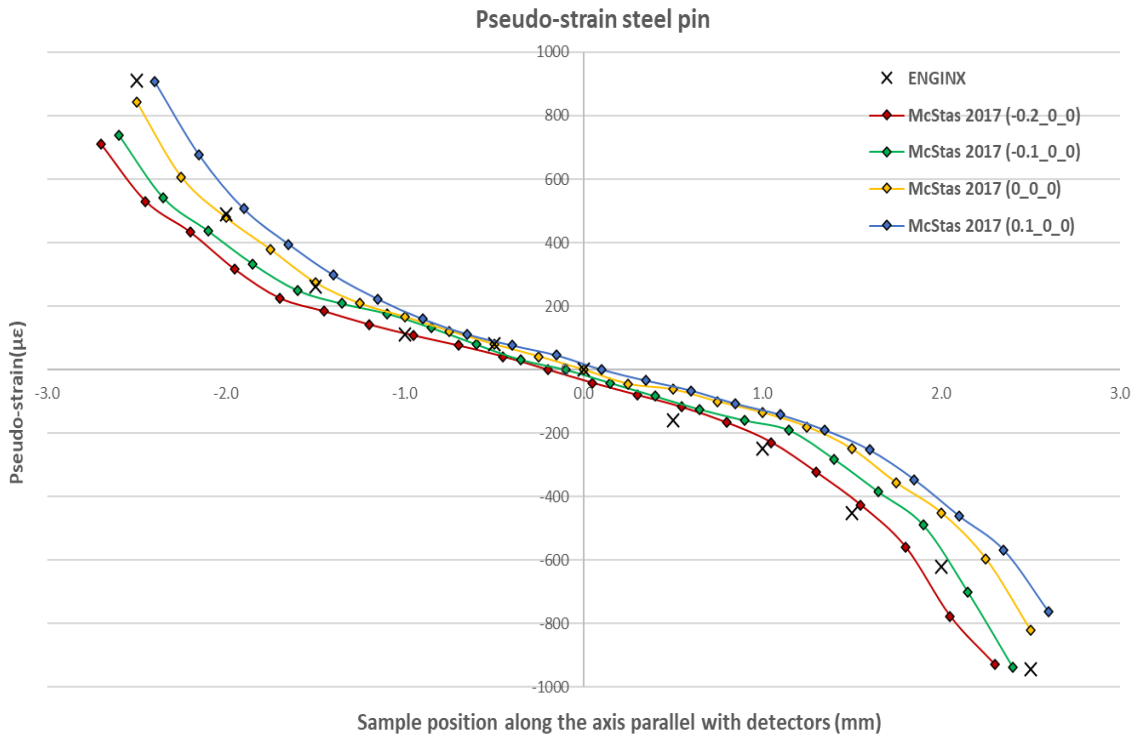

Figure 3.17: Pseudo strain bank 1 using 4mm GV with slit3 moving in horizontal position from -0.2 to 0.4mm in steps of 0.1mm. Only the relevant results are shown. Moving slit3 shows that the curves shift with the effect that for a shift of -0.2 mm the curve in red matches ENGINX crosses for sample position greater than 0 but for sample positions less than 0 the curves diverge.

3.9.1 Geometric effect on pseudo strain

The annealed steel pin is very small so that the attenuation does not contribute to the pseudo strain. This means that the pseudo strain measured in the steel pin scan is solely due to geometry. Based on this a two-dimensional scan for an IGV of 2mm and 4mm was performed of the steel pin with the range of the scan matching the size of the IGV in the xz-plane. The purpose of this scan was to study how the NCOG moves inside this area. The intensity profile for the 2mm GV scan is shown in Figure 3.18 and for the 4mm GV in Figure 3.19. The intensity of the 2mm GV shows a weighting focused on the central portion of the GV largely symmetrical in all direction. With the 4mm GV this is not the case with a diagonal “ridge” observed across the intensity profile.

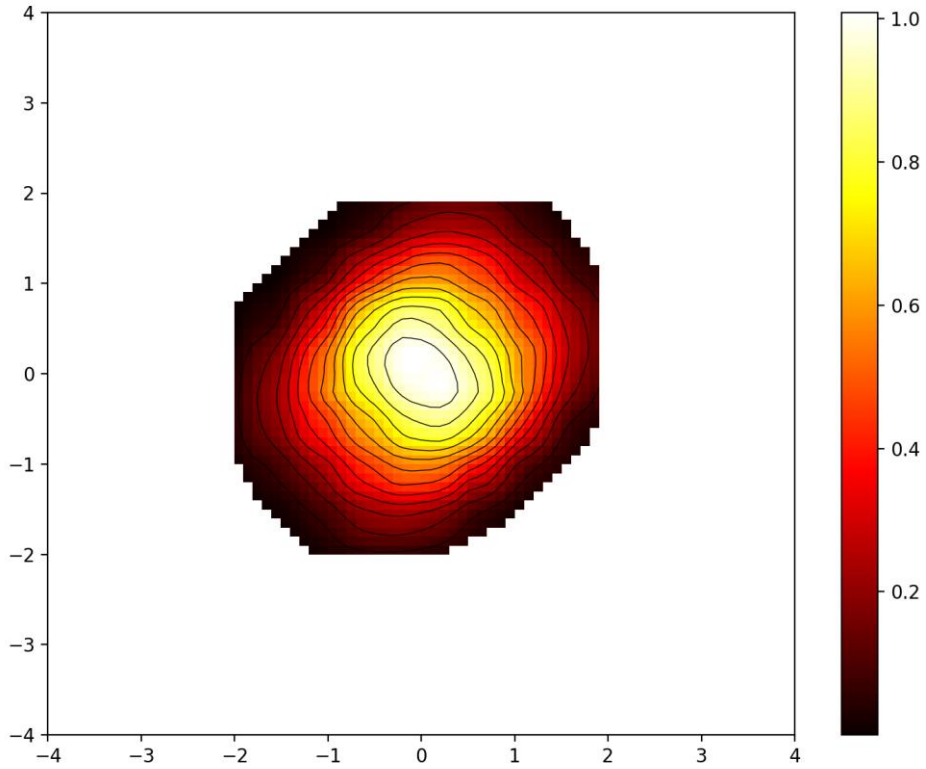

Figure 3.18: Intensity profile for steel pin scan inside IGV plane 2x2mm. The intensities shown are relative to the maximum intensity measured. The intensity of the 2mm GV shows a weighting focused on the central portion of the GV largely symmetrical in all direction.

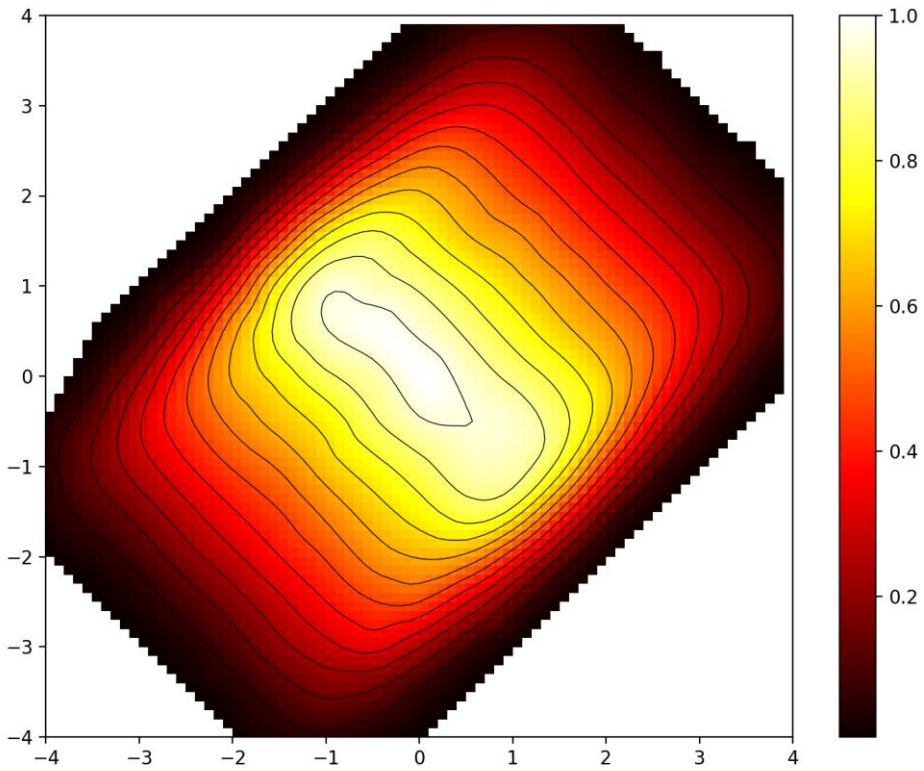

Figure 3.19: Intensity profile for steel pin inside IGV plane 4x4mm.The intensities shown are relative to the maximum intensity measured. Where the intensity of the 2mm GV shows a weighting focused on the central portion of the GV and largely symmetrical in all direction this not the case with the 4mm GV where a diagonal "ridge" can be observed across the intensity profile.

The pseudo strain results for a grid scan of an annealed steel pin (1x20x1) using a 2mm GV are shown in Figure 3.20 and The pseudo strain results for a grid scan of an annealed steel pin (1x20x1) using a 4mm GV are shown in Figure 3.21. In the 2mm GV there is a band of close to zero pseudo strain vertically thought the GV with regions of negative and positive strain on the left- and righthand sides respectively. The 4mm GV shows a similar pattern, it is worth nothing that the 4mm GV pseudo strain profile is not just an extension of the 2mm to greater distances from the centre.

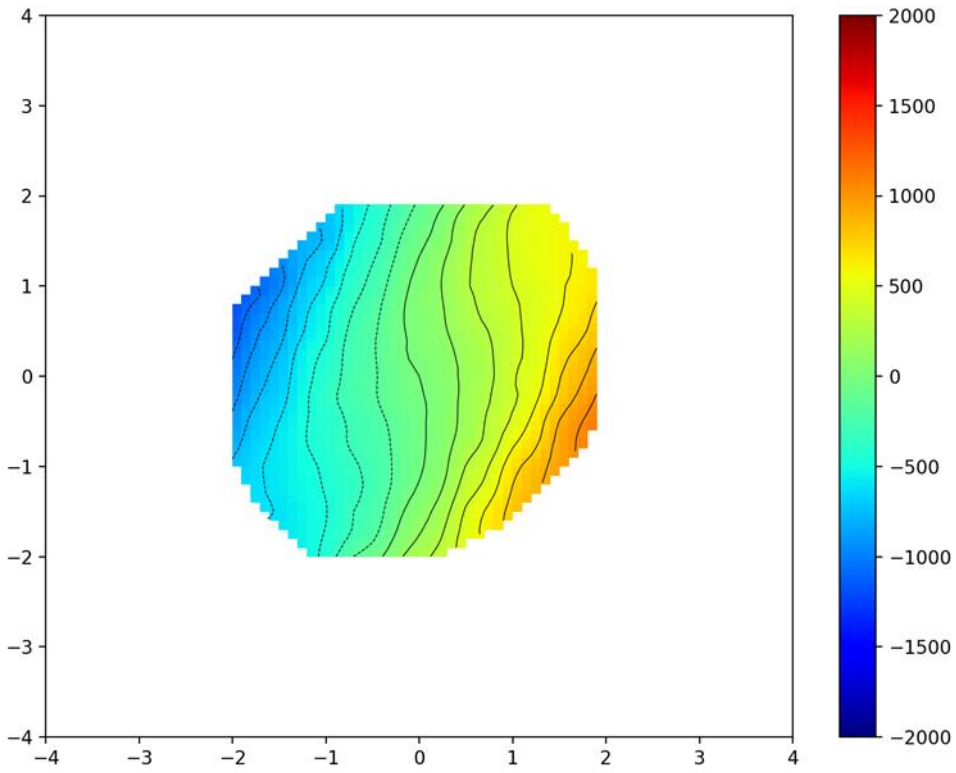

Figure 3.20: Pseudo strain bank 1 for grid scan of annealed steel pin (1x20x1mm) for a 2mm GV. The size of the scanned area was 2x2mm, equal to the gauge volume area. The pseudo strain varies from ~-1500με (dark blue) to ~1000με (orange colour). Bank 1 is in reflection mode. The black dotted lines correspond with points in the IGV that have the same pseudo strain.

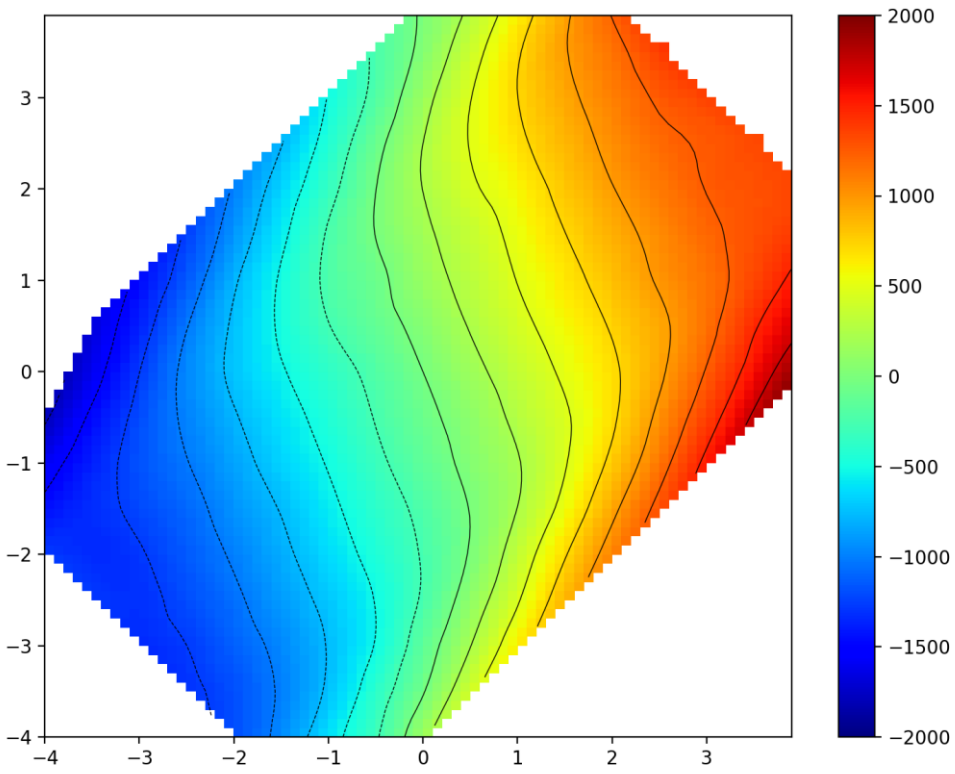

Figure 3.21: Pseudo strain for steel pin scan inside IGV plane 4x4mm.

3.10 Discussion

In this chapter results of a steel pin traversed across the instrument beam in both real and simulated experiments are presented.

The first issue tackled is the replacement of the 2006 model with a new more complete and representative model that better reflects the reality of ENGINX. In terms of intensity, the scan performed along the beam shows good agreement between both McStas models and ENGINX data. The scan across the beam between the two detectors banks however shows some significant disagreement between the 2006 and ENGINX data. Indeed this was the data that first highlighted the issues with the original model.

The scans of strain along and across the beam show the first conformation that McStas is a reasonable tool for prediction of pseudo strain on ENGINX. The prediction of the 2017 model is significantly better than for the 2006 model, however there is still a discrepancy. The scans performed with varying slit 3

position indicate that a very small shift in slit 3 can cause a discrepancy in the strain profile of the magnitude observed. A 100 micron shift in slit 3 cannot be ruled out and is currently under investigation by the beam line staff.

The 2-dimension plots nicely show a visual representation of strain as well as intensity. The intensity profiles essentially show a weighting across the GV. The strain profiles show that although large pseudo strains are measured these are towards the edges of the gauge volume where the weighting by intensity is very low. Plots such as these are invaluable for helping inexperienced users understand the importance of full gauge volume filling and the reality that the GV is not in fact a perfect 4x4x4mm.

Furthermore the intensity across the GV isn't uniform, when adjusting the measurement centre for surface scans it is not a simple geometry correction, but requires weighting of the data to be done based on intensity.

3.11 Summary

A new model of the ENGINX instrument has been built based on architectural documents of the real instrument. The new model has been tested and results compared against the prior model of ENGINX in McStas and against the real ENGINX. The new instrument model not only addresses deficiencies in the existing McStas model of ENGINX but also includes new code so that there is no need to create new instrument models to use different collimators or banks and generates output files with the same naming conventions as ENGINX. The 2006 model only bank 1 could be used in the 2017 also bank 2 can now be used. This is very useful when analysing intensity profiles depending on whether a bank is in transmission or reflection mode relative to sample. The same naming convention was added to facilitate the conversion of McStas output data to a format that can be used by the data analysis tool OpenGenie. This also required new code in OpenGenie. To run simulations on the HPC used at ISIS a new bash shell script has been written that reads the values for the input parameters to be used in a simulation from a text file. The first 6 columns of this text file resembles closely the one used for the real ENGINX instrument. This new script makes it possible to run scans with variable step size in three dimensions and varying the number of neutrons per scan point. The script can easily be adapted to add more columns to the script file. Those extra columns can be used to store values for parameters used in components such as slits, collimators, detector bank and materials as well as to activate a component for use in simulation. This last feature has been used extensively in the virtual experiments described in the next chapters. The ability to add extra parameters makes it possible to simulate many different scenarios without the need to create new versions of the ENGINX instrument model. The shell script includes the necessary code to use the parallel processing capabilities offered by McStas which is essential to run realistic simulations in a practical timeframe. The shell script can

run on PC using Linux and on HPC. The simulations done for this research project are very computing intensive and would not have possible to run on a PC. The new instrument model, the added functionality and the new shell script are indispensable to perform the virtual experiments described in the next chapters.

3.12 Summary of changes to ENGINX McStas model

The modifications made to the ENGINX instrument code and ancillary software needed to perform the virtual experiments and data analysis that are the focus of this project are listed in Table 3.3 .

Table 3.3: Issues with the 2006 model and remediations.

No	Issue	Modification
1	Using a different collimator required a new instrument file in McStas, causing version control problems and human error	Added extra C-code in the instrument file initialisation section so that the user only needs to specify the gauge volume size and this code will select the right collimator and settings.
2	Detector component type `TOFlog_spher` only working for bank 1	Re-wrote the C-code in the `TOFlog_spher` component type to include both detector bank 1 detector bank 2 in the instrument
3	McStas output files cannot be read by OpenGenie, the data analysis software used for the peak fitting on ENGINX	Modified the code in OpenGenie. A procedure has been written that converts the McStas output into a format that resembles the output of ENGINX. The converted output can now be analysed with OpenGenie in the same way as output from ENGINX
4	Scan facility in McStas too limited. Supports only scan in one dimension and cannot do grid type scans. The number of neutron histories is fixed for the whole scan range, cannot be varied by scan point. Scan step size is fixed for the whole scan.	Created a new shell script to run McStas on the HPC. This shell script read a script file. The script file has been designed to mimic the script file of the real ENGINX

No	Issue	Modification
		instrument. There are two key differences: (1) The McStas script file specifies the run number for each scan point. (2) In the ENGINX script file the number of micro amps per scan point is specified while in the McStas script file the number of neutrons to simulate per scan point is specified. The script also contains code to generate the intensity profiles.
5	Simulating the same instrument for a range of different parameter values without the need to create separate instrument files and shell scripts	Expanded the shell script and the script input file used on HPC. The script input file has been expanded with additional columns representing parameters like collimator size, detector bank, slit opening etc
6	Components missing from 2006 instrument model and incorrect parameter settings	Added guides, slits and choppers that were missing from instrument and corrected settings of the source component
7	No control over run numbers in McStas scan, run number are always a range of sequential numbers	Modified the instrument code so that the run number for a given scan point is read from the script input file and this number is used as part of the output filename.
8	Display of run number in output window of peak fitting in OpenGenie	Modified OpenGenie so that the output window shows the run number of the dataset subject of the fit.

4 Evaluation of McStas for lattice parameter characterisation

4.1 Introduction and motivation

To date very little research has been reported using McStas to simulate lattice parameters with the majority of research focusing on instrument intensity optimisation [82] and background characterisation [79]. In this section results are presented from a set of simple experiments to determine if McStas has sufficient precision and sensitivity to characterise the small shifts in diffraction peak caused by changes in diffraction geometry, attenuation and gauge volume filling.

4.2 Methodology – partial filled gauge volume

To assess the effect of a partially filled gauge volume, an event that is essential for surface measurements but may also occur by accident as a result of poor set up or poor knowledge of a sample geometry, scans traversing the GV from air to within the material have been performed. In these strain measurements the gauge volume enter a sample surface by traversing the neutron beam with the start position of the scan chosen so that the sample is not interacting with the beam, the sample then moves in steps so that the sample gauge volume (SGV) will initially be partially immersed near the surface of the material , fully immersed when the GV is in the centre of the sample and again partially immersed when reaching the opposite surface of the sample as shown in **Error! Reference source not found.**. This type of scan is referred to as a near surface strain measurement or air-to-material /material-to-air transition. The partial immersion of the SGV gives rise to a change in peak position with can be interpreted pseudo strain.

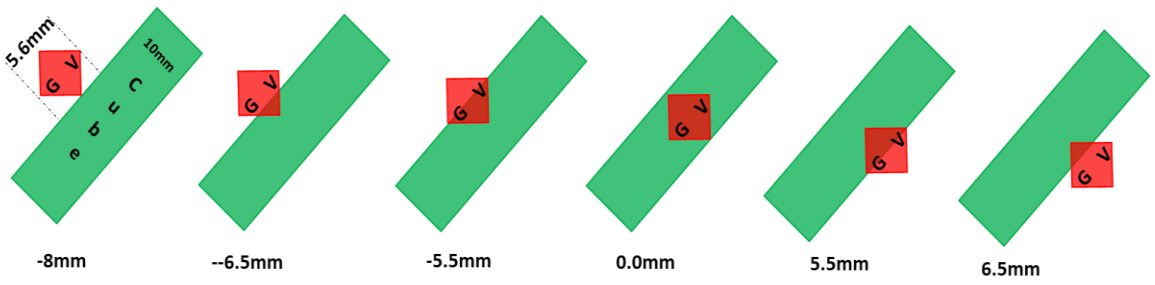

Figure 4.1: Change of sample gauge volume (IGV=4mm) when cube traverses beam under angle of 45°

For this experiment a hollow cube made of an aluminium alloy filled with iron powder was used. Aluminium has a low density of 2.7 g/cm^3 and a small absorption cross section of 0.23 barn, hence the number of neutrons scattered or absorbed by the aluminium hull is very low. The dimensions of the region containing iron powder were 10x15x29 mm, the hull had a thickness of 0.5mm with external

dimensions 10x16x30mm. The iron powder had a quoted tap density (the density of the powder when tapped) of 41%. The cube traversed the beam at an omega angle of -135° as shown in Figure 4.2 . A 4mm gauge volume was used and the scan was started at -8mm from the centre of the IGV. Two step sizes were used during the scan dependent on the position, one of 0.5mm and one of 1mm resulting in a total of 25 scan points. Two virtual sample models were set up in McStas. In the first model the powder cube was modelled using two concentric positioned cubes of component type `PowderN`. Where the inner cube represents the iron powder cube and the outer cube represents the aluminium hull. The second model uses the union concept and the powder cube was represented with a `Union_box` component type. The dimensions of the hull and powder cube for each sample type were identical and nominally identical to those used in the experiment.

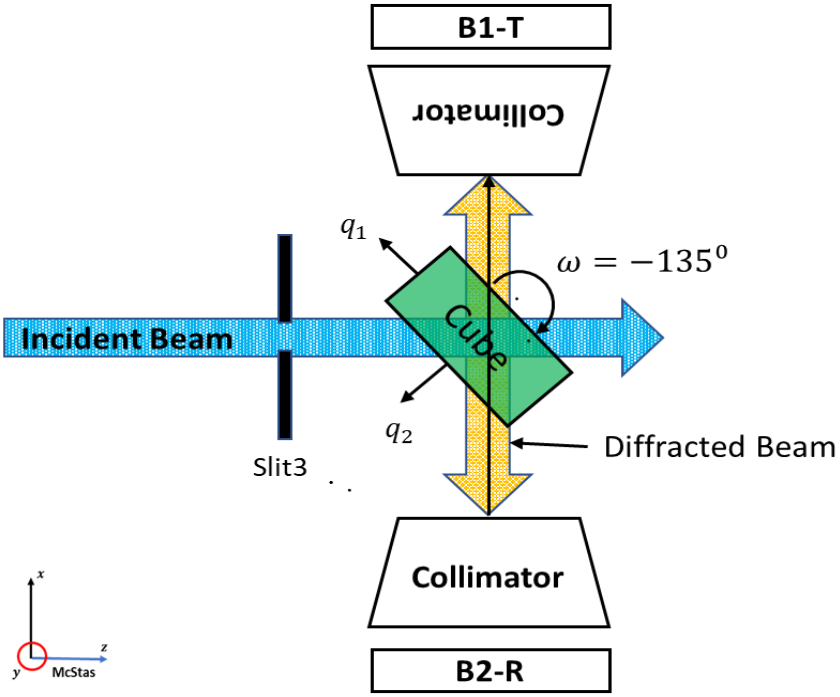

Figure 4.2: Iron powder cube of dimensions 10x15x29mm and density 41%, traversing beam under an angle of -135°. B1-T and B2-R denote bank 1 in transmission and bank 2 in reflection respectively. .

The physical and crystallographic properties for the iron powder cube were taken from the `Fe.laz` reflections file in McStas which corresponds with a generic ferritic steel. Many of the values in this file can be overwritten at sample component level. This approach was used to override the density in the reflections file by setting the packing factor to 41%. A 4mm gauge volume was used and the scan started at -8mm from the centre of the IGV and used the same step sizes as used in the experiment. The simulation was repeated with the iron powder replaced with a nickel powder using the 'Ni.laz' file in McStas. The objective of this second simulation was to investigate the effect of attenuation on

pseudo strain as a function of the material. Nickel was selected because it has a large neutron cross section compared to Iron and will be used in future simulations.

As mentioned in section 2.5.2, making a second measurement at a rotation of 180^o and averaging is a common method for mitigating non-uniform gauge volume filling effects. To verify the accuracy of this process, the simulations were repeated with the sample rotated 180^o (omega of -45^o).

For this sample a z-scan was also simulated using McStas to show a z-scan has no pseudo-strain as the gauge volume stays fully immersed during the scan.

The different experiments and simulations are summarised in Table 4.1.

Table 4.1: Experiments and simulations performed using an iron powder cube

Description	Material	IGV	ω	Scan range, step size mm	#Scan points	Scope
Horizontal scan across beam	Iron	4	135	$x[-8,8,0.5]$	25	Exp & Virtual
Horizontal scan across beam	Iron	4	-45	$x[-8,8,0.5]$	25	Virtual
Horizontal scan across beam	Nickel	4	135	$x[-8,8,0.5]$	25	Virtual
Horizontal scan across beam	Nickel	4	-45	$x[-8,8,0.5]$	25	Virtual
Vertical z-scan	Iron	4	135	$\boldsymbol{y}[-\mathbf{8},\mathbf{4},\mathbf{0.5}]$	25	Virtual

4.3 Results material to air for a powder cube

The pseudo strain occurring in an air to material and material to air scan are shown in Figure 4.3. During the experiment bank 1 was in transmission mode and bank 2 in reflection mode. As the gauge volume enters the sample (most negative x position) a large positive strain is measured which reduces as the gauge volume approaches the centre of the sample. At the centre of the sample the strain is 0 as a result of this also being the reference point. As the gauge volume leaves the sample (increasingly positive x) there is an increasingly negative strain measured. The results for bank 2 show a good fit between the real experiment using ENGINX and the equivalent virtual experiment using McStas. The results for bank 1 show a good fit for sample positions between -4.0 and 7.0 mm, when the sample

position is smaller than -4.0 mm the experiment shows a smaller pseudo strain than the simulation. This difference increases the further the sample moves through the beam.

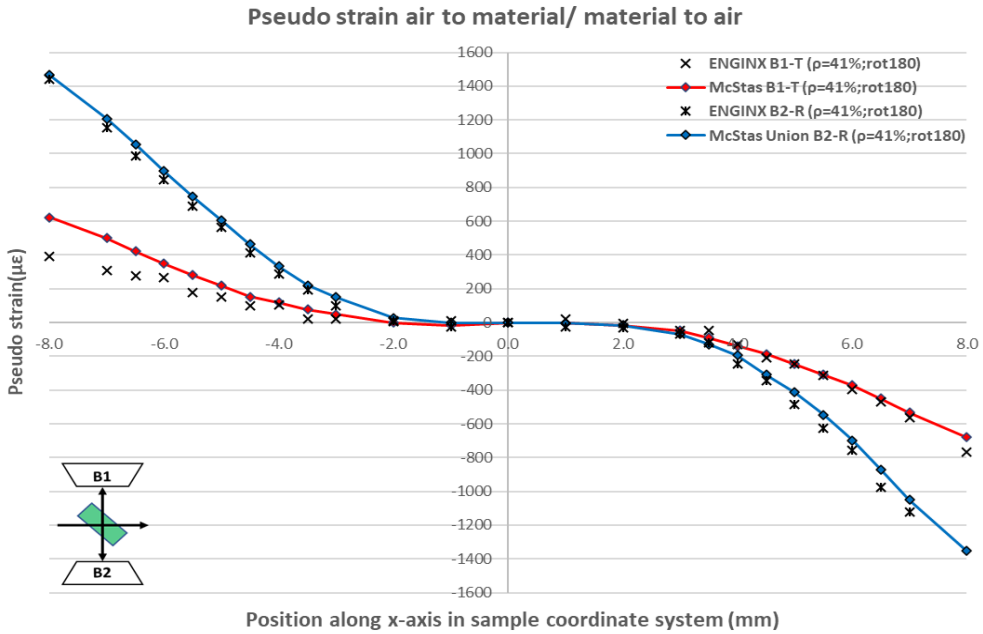

Figure 4.3: Pseudo strain occurring in air to material/ material to air scan. The sample used is an iron powder cube (10x15x29mm) with density 41%. The results shown are from a real experiment using ENGINX and an equivalent virtual experiment using McStas with the sample rotated 180^{o}. TOF range of 20000-40000 was used for peak fitting in OpenGenie.

The McStas simulations as shown in Figure 4.3 where repeated using the sample model built using the `Union_box` component type. The results of these simulations are shown in Figure 4.4.

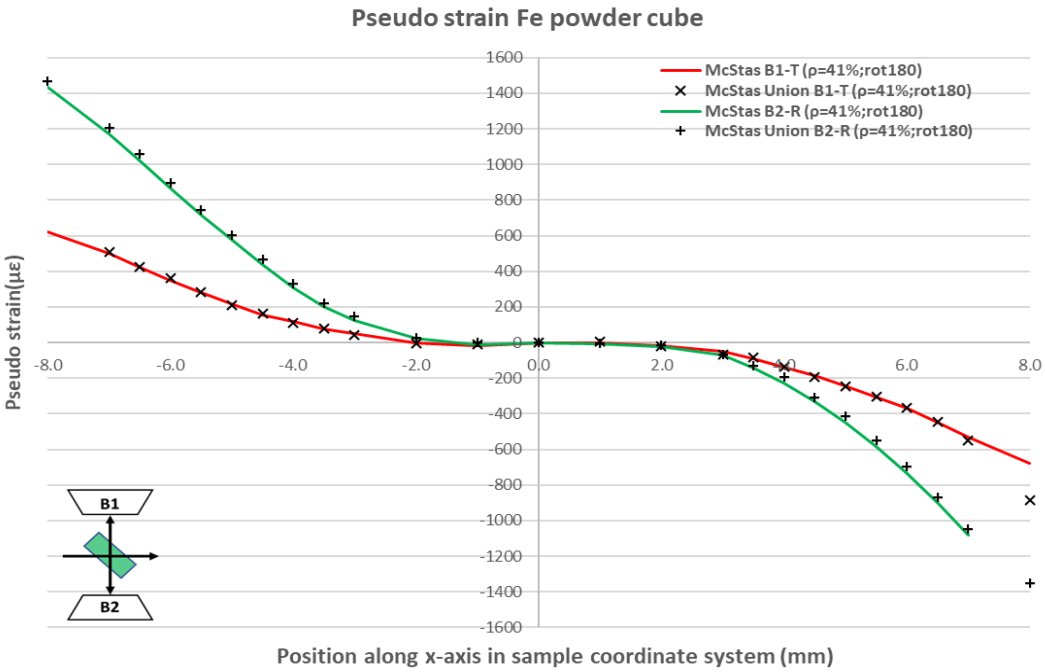

Figure 4.4: The pseudo strain for an iron cube (1015x29) density 41%. The crosses show the pseudo strain using the Union_box component type they match the pseudo strain (red and green plots) using the PowderN component type.

The pseudo strain (crosses) using the Union_box component type match the pseudo strain (red and green plots) using the PowderN component type. The PowderN results presented show little deviation from their corresponding Union_box results essentially confirming the suitability to interchange between each setup in this geometry.

The results of measurements made at 180^{o} and averaged for an air to material/ material to air scan using an iron powder cube are shown in Figure 4.5 for bank 1 and in Figure 4.6 for bank 2. These simulations show that when the detector bank is in transmission mode the results of the two simulations cancel each other out. When the detector bank is in reflection mode the simulation results do not cancel out with a discrepancy increasing to a maximum of approximately 150 at positions of -5.5 and 5.5.

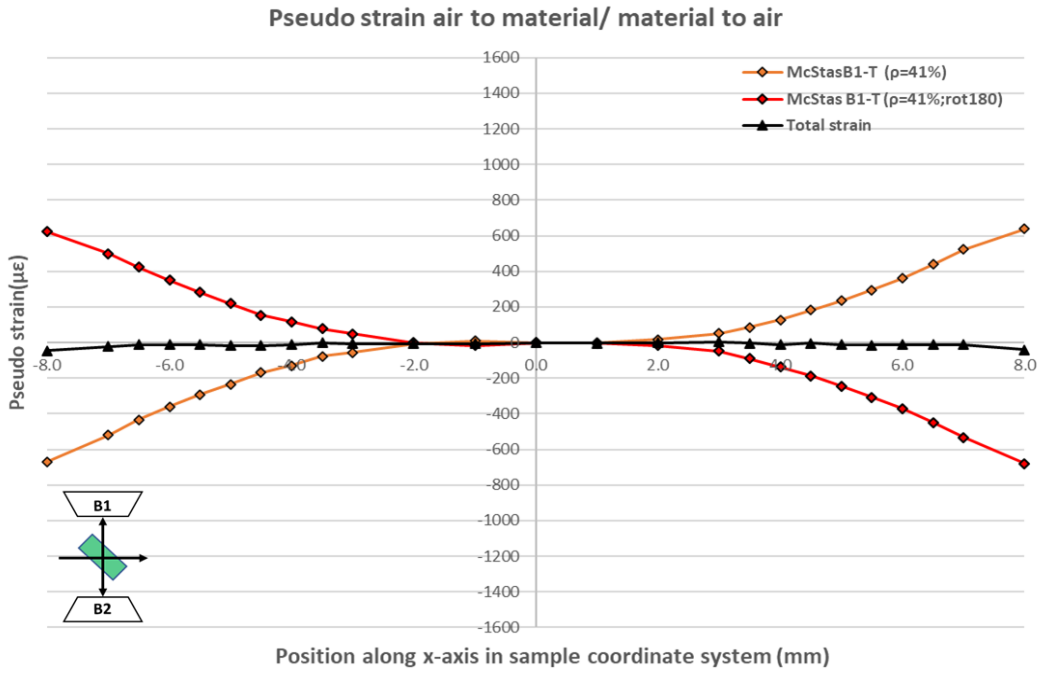

Figure 4.5: Pseudo strain results bank 1 for air to material/ material to air scan with sample orientation parallel to scan direction and rotated 180°. Sample is an iron powder cube (10x15x29mm) with density 41%. Bank 1 is in transmission mode. The total pseudo strain for both orientations adds up to zero.

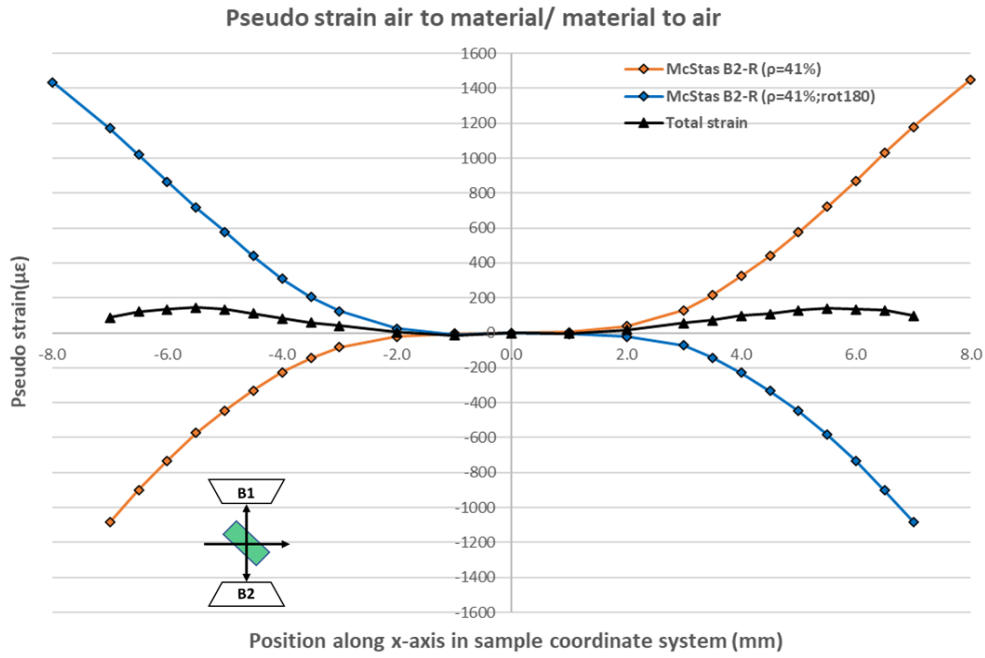

Figure 4.6: Pseudo strain results bank 2 for air to material/ material to air scan with sample orientation parallel to scan direction and rotated 180°. Sample used is iron powder cube (10x15x29mm) with density 41%. Bank 2 is in reflection mode. The total pseudo strain for both orientations is zero when x between -3 and 3 mm outside this range the total strain is significantly larger than zero reaching a maxim of ~ 150με at ~-5.5 and +5.5mm.

The normalised intensity profile for bank 1 in transmission mode of an iron powder cube of dimensions 10x15x29mm with density 41% is shown in Figure 4.7: Normalised intensity profiles with bank 1 in

transmission for an iron power cube (10x15x29) with densities resp, 41% and 82%. The simulation results match the ENGINX experimental results for density 41% however the simulation shows that difference in density does not change the normalised intensity profile. The normalised intensity profile of the McStas simulation matches the normalised intensity profile of the ENGINX experiment. The shape of the intensity profile is symmetrical and the intensities do not change with the density.

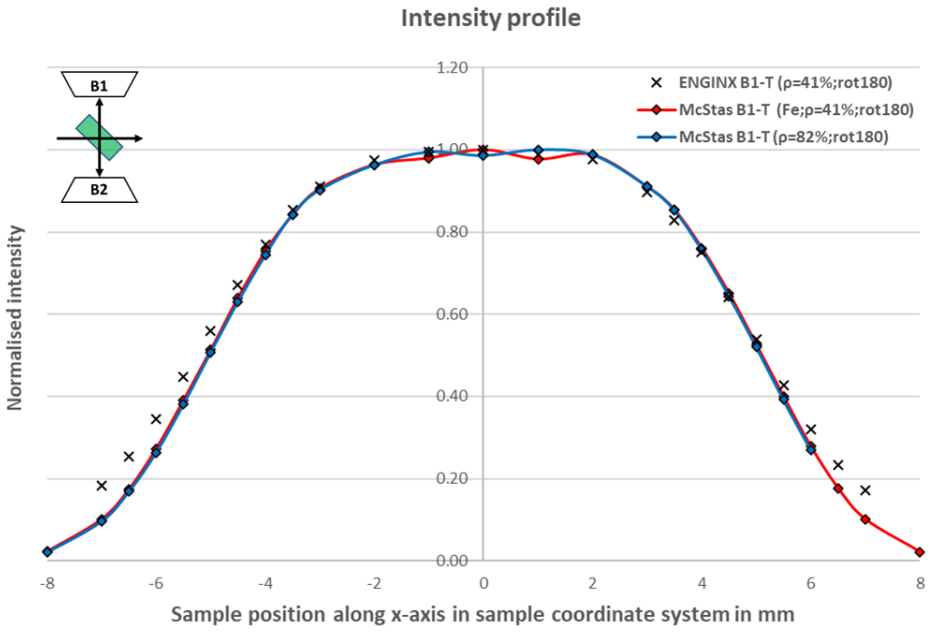

Figure 4.7: Normalised intensity profiles with bank 1 in transmission for an iron power cube (10x15x29) with densities resp, 41% and 82%. The simulation results match the ENGINX experimental results for density 41% however the simulation shows that difference in density does not change the normalised intensity profile.

The normalised intensity profile for bank 2 in reflection mode of an iron powder cube of dimensions 10x15x29mm with density resp, 41% and 82% is shown in Figure 4.8Figure 4.7: Normalised intensity profiles with bank 1 in transmission for an iron power cube (10x15x29) with densities resp, 41% and 82%. The simulation results match the ENGINX experimental results for density 41% however the simulation shows that difference in density does not change the normalised intensity profile.. The normalised intensity profile of the McStas simulation matches the normalised intensity profile of the ENGINX experiment when the density is 41%. The shape of the intensity profile lacks the symmetry of the transmission intensity profile. The intensity is now also varying when the density changes.

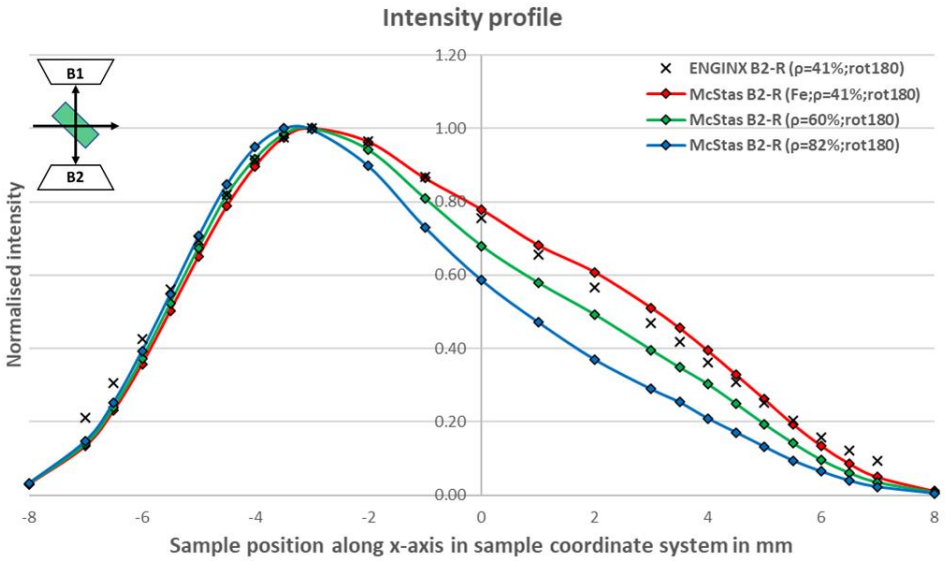

Figure 4.8: Normalised intensity profiles with bank 2 in reflection for an iron power cube (10x15x29) with densities resp, 41%, 60% and 82%. The simulation results match the ENGINX experimental results for density 41%. The simulation results show that the intensity profile changes with density.

The effect of the density on the pseudo strain for an iron powder cube (10x15x29mm) with densities of resp, 41% and 81% is illustrated in Figure 4.9. When the sample position is between -3 and +3mm than there is no difference in the pseudo strain for the two densities. The difference is close to zero at -3 and +3mm but gradually increases with the pseudo strain for a cube with density 81% larger than for a cube with density 41% for sample positions less than -3m m and larger than +3mm.

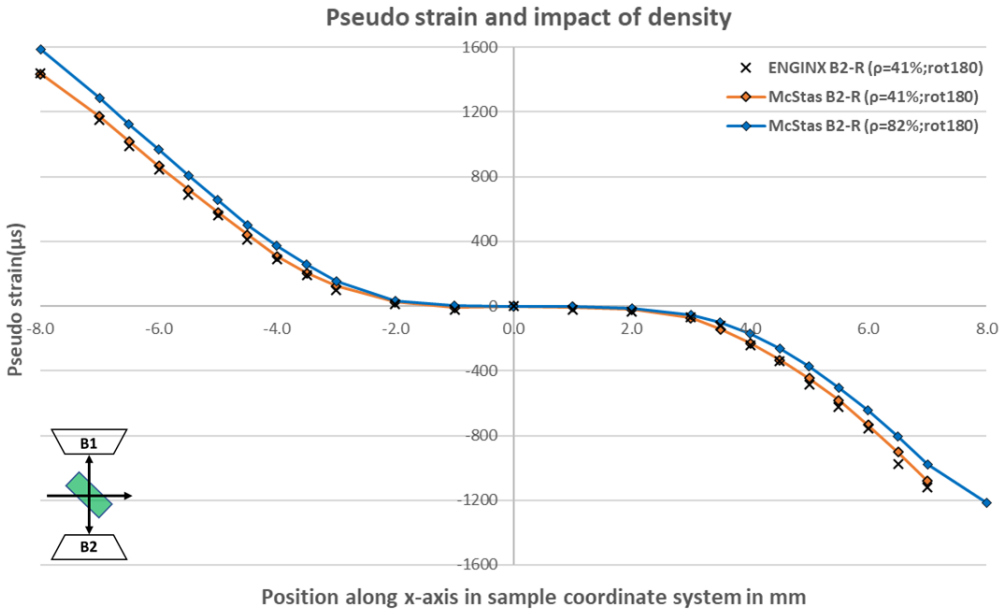

Figure 4.9: The pseudo strain for an iron powder cube (10x15x29) and density 82% is the same as for a density of 41% when the sample position is between -3 and +3mm. For sample positions less than -3mm and larger than 3mm the pseudo strain of the 81% density is larger than for a sample with density of 41%. The magnitude of this difference gradually increases.

The dimensions of the sample influence the intensity profile. The normalised intensity profiles for an iron power cube of dimension 9x14x29mm and of dimension 10x15x30mm are shown in Figure 4.10. In both cases the iron powder was contained in an aluminium hull of 0.5mm thickness. The results show a closer fit between McStas simulation and ENGINX experiment for the iron powder cube with dimension 10x15x30mm. At first sight these results seem trivial and somewhat obvious. However, the purpose is to highlight the influence of a small error in sample modelling. A difference in 1mm from the design spec for a weld is reasonable and would cause effects to be present in the simulation that would not exist at the same location in the real sample.

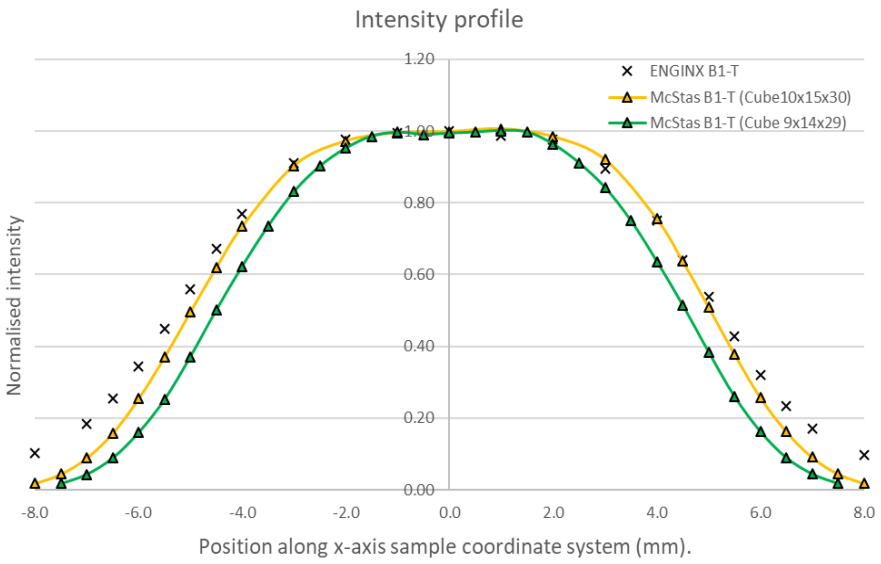

Figure 4.10: Normalised intensity profiles of iron powder cubes with dimensions 9x14x29mm and 10x15x30mm. Bank 1 is in transmission mode. The intensity profile of the cube with dimensions 10x15x30mm gives a better fit with the ENGINX intensity profile.

The simulations were repeated with all parameters consistent but with the iron powder replaced with nickel powder. The results for bank 1 in transmission mode are shown in Figure 4.11 and for bank 2 in reflection mode in Figure 4.11.

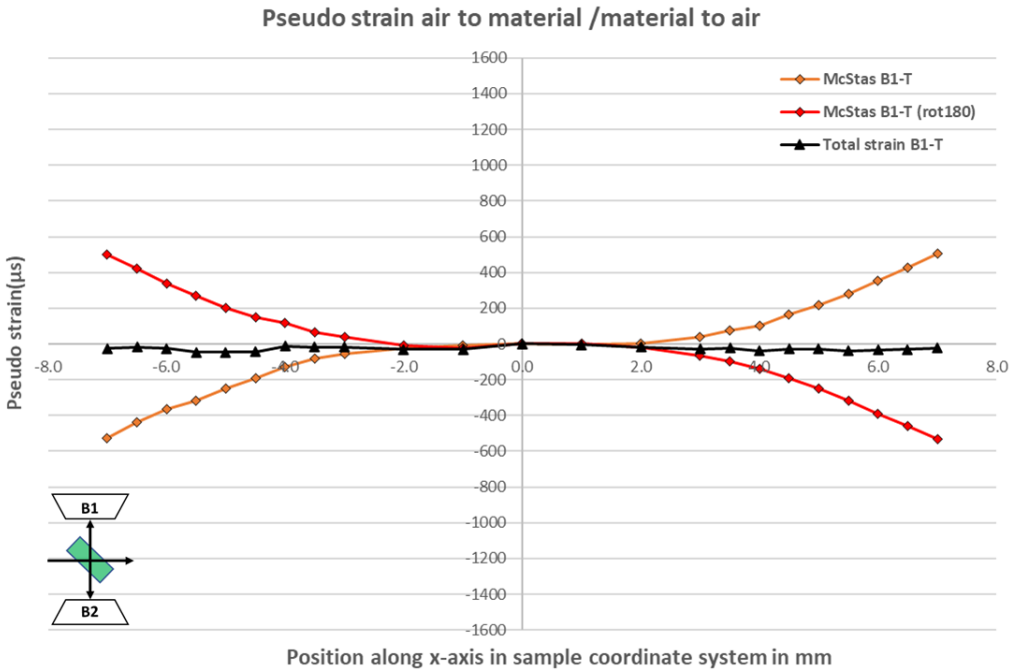

Figure 4.11: Pseudo strain results bank 1 for air to material/ material to air scan with sample orientation parallel to scan direction and rotated 180^{o}. Sample is a nickel powder cube (10x15x29mm) with density 41%. Bank 1 is in transmission mode. The total pseudo strain for both orientations adds up to zero.

As with Iron powder, in transmission mode the pseudo strain for both orientations cancel each other out as was the case with iron powder cube sample. In reflection mode this is not the case. In the case

for Nickel powder, the results for transmission mode are similar to iron in both shape and magnitude, in reflection mode however, the shape of the curves correspond with Iron powder but the magnitudes are somewhat larger with maxima of approximately 300 at positions of -6 and 6 in x.

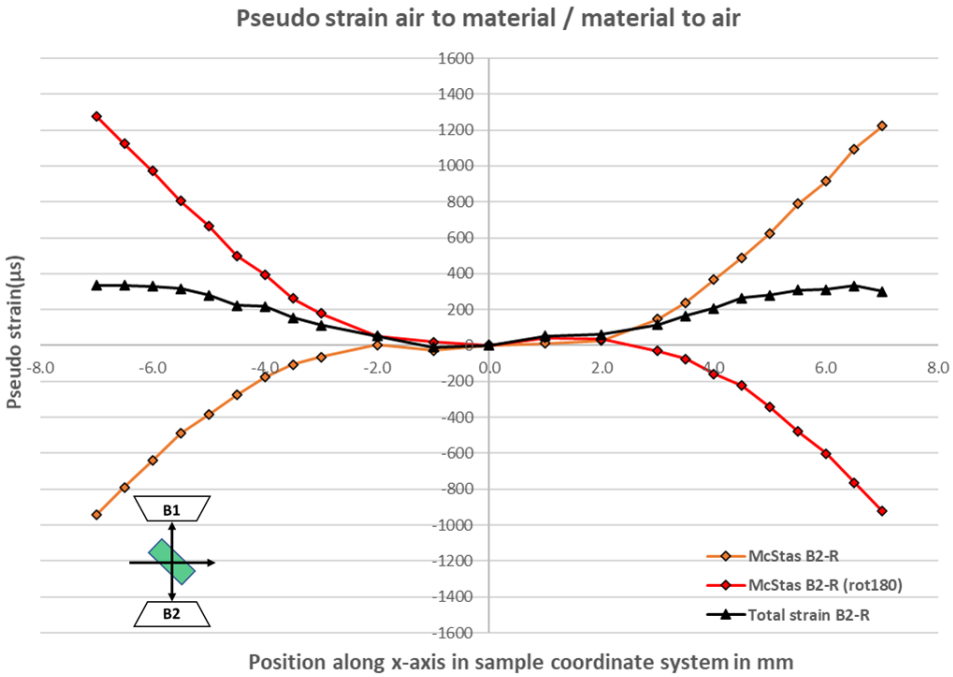

Figure 4.12: Pseudo strain results bank 2 in reflection mode for air to material/ material to air scan with sample orientation parallel to scan direction and rotated 180^{o}. Sample used is nickel powder cube (10x15x29mm) with density 41%. The total pseudo strain for both orientations is zero between -3 and 3 mm outside this range the total strain is significantly larger than zero reaching a maximum of ~ 335µε at ~-6.5 and +6.5mm.

The intensity profiles of bank 1 in transmission mode for the iron and nickel powder cube (15x15x29mm) with density 41% are shown in Figure 4.13 and for reflection mode in Figure 4.14. The shape and symmetry in transmission mode are similar the intensities for nickel are higher. In reflection mode the shape is not symmetrical.

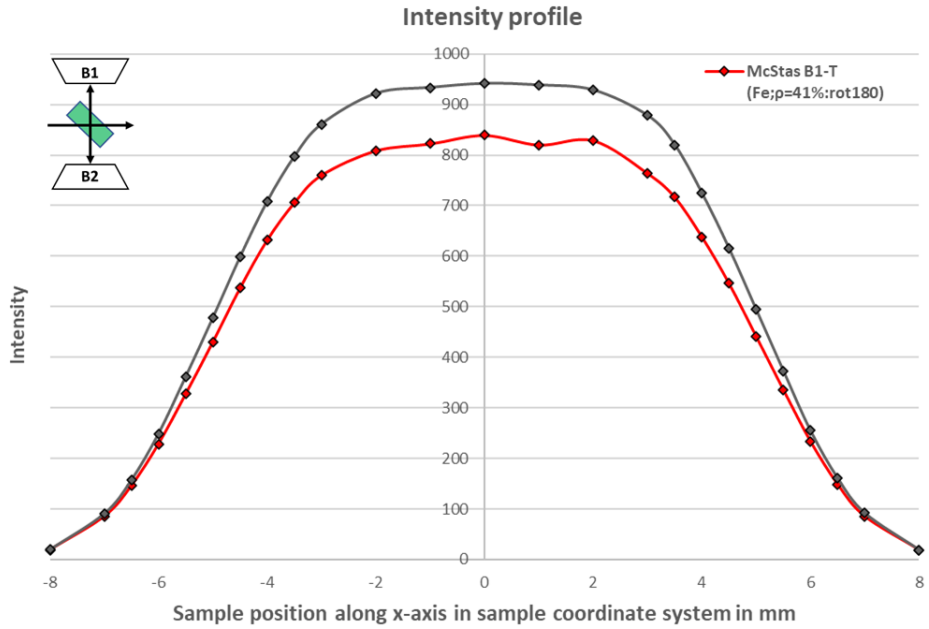

Figure 4.13: Intensities in transmission mode for iron and nickel powder cube (10x15x29mm). The shape of the intensity profile is symmetrical for both materials with the intensities of nickel higher than for iron.

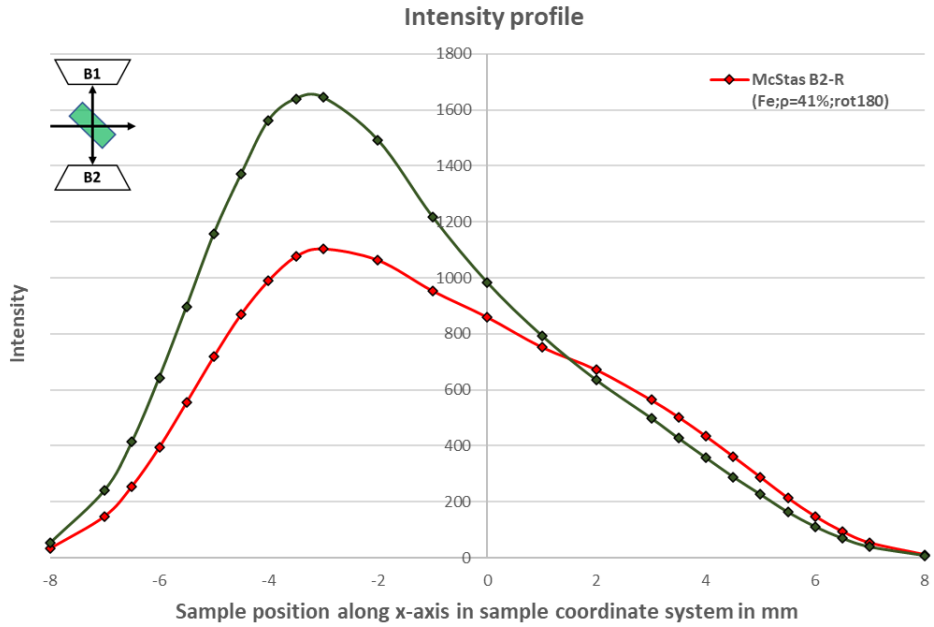

Figure 4.14: Intensities in reflection mode for iron and nickel powder cube (10x15x29mm). The shape of the intensity profile is not symmetrical for both materials with the nickel profile more pronounced in shape. The intensities of nickel are higher than for iron between -8 and 1.5mm while lower between 1.5 and 8mm.

Pseudo strain results for an air to material z-scan of an iron powder cube (10X15X29mm) with density 41% are shown in Figure 4.15. For a 4 mm GV and sample positions between 0 and 8mm the pseudo

strain fluctuates between -20 and +20με. For the 2mm GV this is similar between 0.5 and 8mm, but goes up to ~40με at position 0.

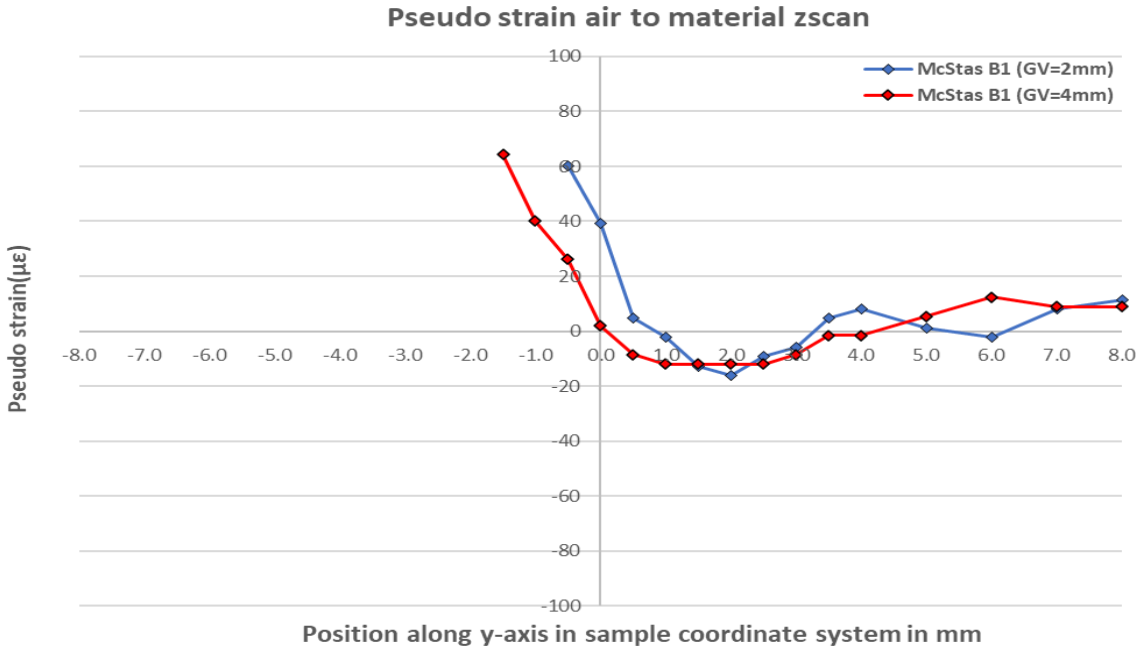

Figure 4.15: Pseudo strain results for a z-scan of an iron powder cube (10X15X29mm) with density 41%. For sample positions between 0 and 8mm with GV=4mm the pseudo strain fluctuates between -20 and 20 which indicates that there is no pseudo strain of any significance and can be considered zero for practical measurements as expected. For GV=2 this is the same between 0.5 and 8mm with larger value at 0.

The intensity profile of the air to material z-scan of the iron powder cube (10x15x29mm) for a 2mm and 4mm GV is shown in Figure 4.16. The intensity increases once the sample gauge volume is partially immersed to reach a value that remains constant once fully immersed which happens between 1.5 and 2mm for a 2mm GV and between 3 and 4mm for a 4mm GV.

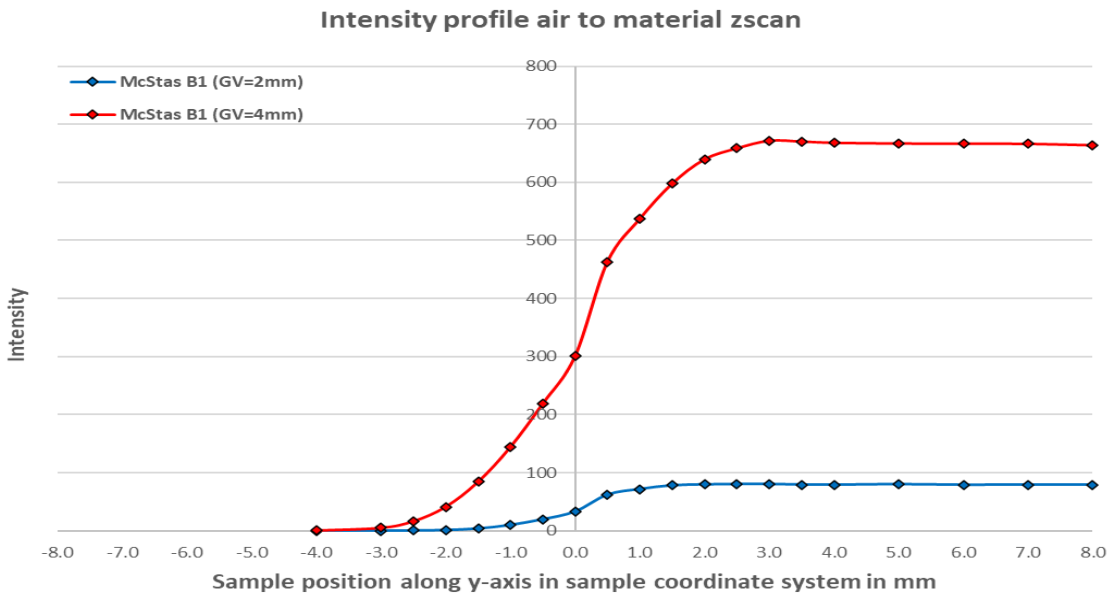

Figure 4.16: Intensity profile air to material z-scan for an iron powder cube (10x15x29mm) with density 41%, for a 2mm and 4mm GV. The intensity at position 0 is less than 50% of the intensity at position 4mm for 4mm GV and the intensity at position 0 is less than 50% of the intensity at position 2mm for 2mm GV.

4.4 Discussion

The virtual experiments performed using a cube demonstrate how the intensity and the pseudo strain are impacted by the dimensions of the cube and the physical properties of the material used especially the density and the cross sections for scattering and absorption. The simulation of a z-scan where the cube traverses the beam in a vertical direction under an angle confirms that using this method no pseudo strains occur. During a z-scan the geometric centre of the GV coincides with the NCOG for each sample position. Although the size of the GV reduces when approaching the material to air interface, the geometric centre of the GV and the NCOG still coincide. The smaller GV reduces the number of neutrons available for scattering increasing the fitting error. A 2mm GV contains ~1/8 of the neutrons in a 4mm GV and near the material to air interface this results in a very low number of neutrons available for fitting which results in large fitting errors in the order of 50% of the pseudo strain. For positions less than 0, this error becomes of a similar magnitude as the pseudo strain and can be discarded. The z-scan technique can be used to mitigate for pseudo strain but the size of the sample and geometry of the instrument may not always be suitable to use this method. The technique of rotating the sample 180^{o} and repeating the measurement as a way of mitigating for the pseudo strain occurring works when the detector bank is in transmission mode for both iron and nickel. Furthermore, the shape and magnitudes of the results for both materials are very similar. This indicated that the pseudo strain in transmission is largely due to a geometric effect with little

dependence on the type of material. When the bank is in reflection mode the pseudo strain no longer cancel out for all sample positions using this technique as illustrated in Figure 4.17. The magnitudes of the strains appear very different for the two materials with significantly larger pseudo strains observed for Nickle. This is interpreted as a result of attenuation, which nickel having significantly greater attenuation than Iron.

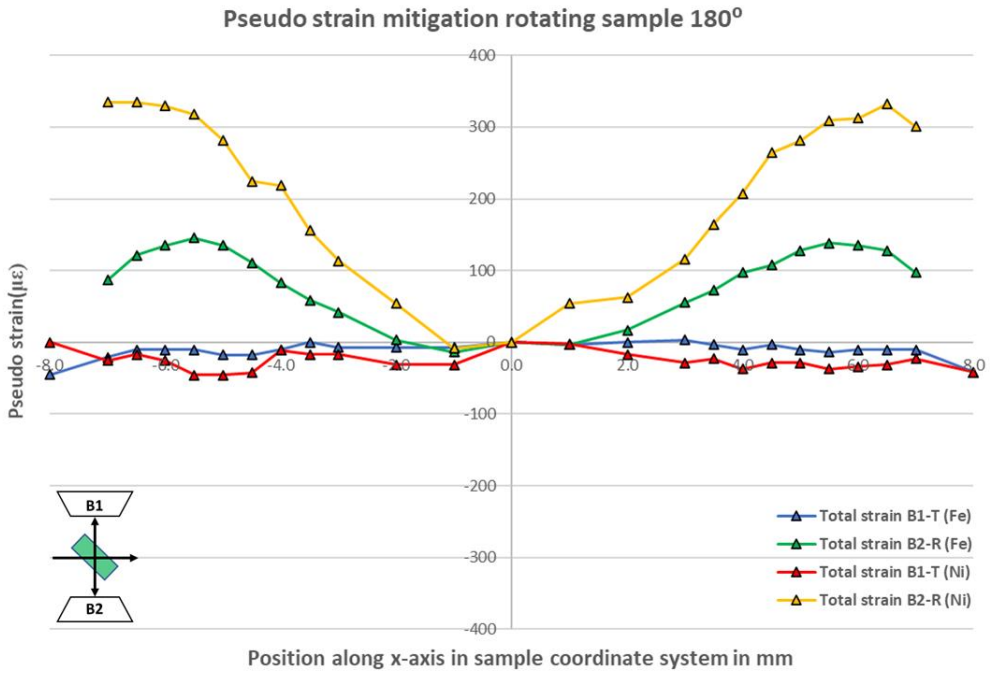

Figure 4.17: Mitigating for pseudo strain by performing two measurements with the sample rotated 180° in the second measurement works when bank is in transmission mode but less well in reflection mode with pseudo strain not cancelling out for sample positions less than -2mm or greater than 2 mm.

These results can be explained when taking into account the geometry of the experiment and the attenuation which is dependent on the material used. In transmission mode the average path length the neutrons travel through the sample does not vary by sample position whereas in reflection mode the pathlength the neutrons travel through the sample varies. This difference is clearly illustrated by the intensity profiles with lower intensities for longer path lengths due to higher probability of neutrons being absorbed. In transmission mode the path length remains the same for each sample position in both scan orientations hence the magnitude of the pseudo strain in both measurements is the same but with opposite sign. In reflection mode the pathlength varies for each sample position and can be significant longer than in transmission mode. This difference is illustrated in Figure 4.18 for two different sample positions.

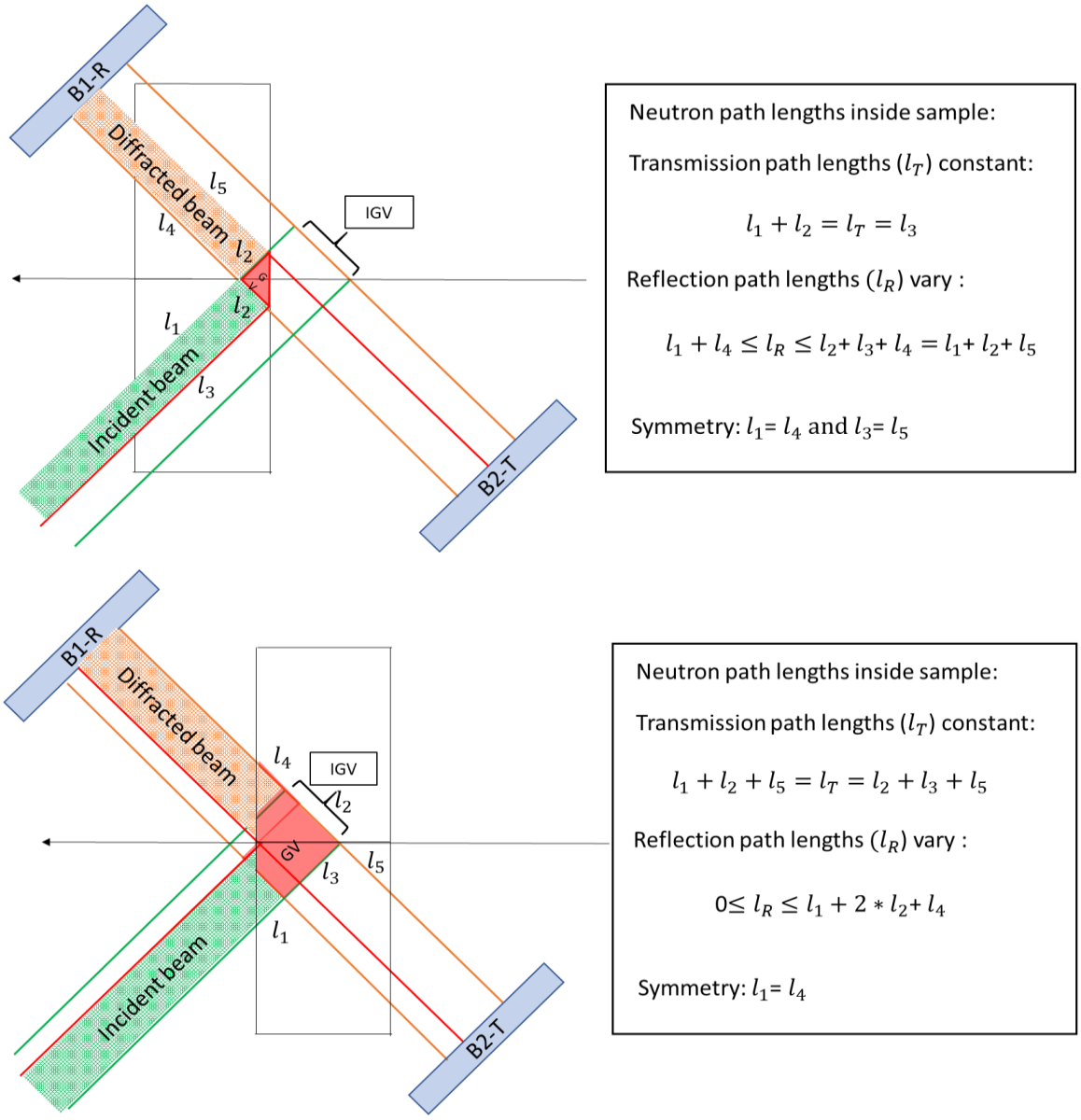

Figure 4.18:The diagrams show the neutron path lengths for two different sample positions. The sample is the vertical rectangular square moving from right to left. The path length of the neutrons in transmission mode stay constant, while in reflection they vary. This explains why the 180° rotation of the sample does not average out the pseudo strain. The above equations give the path lengths for the neutrons following the boundaries of the incident and diffracting beam, a more rigorous proof that is valid for all path lengths requires trigonometry and to make use of the specific symmetries in this sample set up.

This is the reason that the pseudo strain measured for the same sample position when rotating the sample 180° no longer cancels out. A longer path length increases the TOF, increases the chance of neutrons being attenuated and results in larger pseudo strains. This contribution to the pseudo strain cannot be solely attributed to the geometry. The attenuation is dependent on the density of the material and the scattering and absorption cross sections. This is clearly illustrated by comparing the results of the iron powder cube with the nickel powder cube. The absorption cross section of nickel is 4.49 barn which is significantly larger than that of iron 2.56 barn. Nickel has also a higher density of 8.91 g/cm^3 than iron 7.87 g/cm^3.

The impact on the pseudo strain for bank 1 in transmission due to the NCOG diverging from the geometric centre of the cube when traversing the beam is plotted in Figure 4.19. The square represents the GV used, the circle represents the NCOG, and the colour represents the pseudo strain measured. The diagram is obtained by calculating the weighted average of the data presented in Chapter 3.

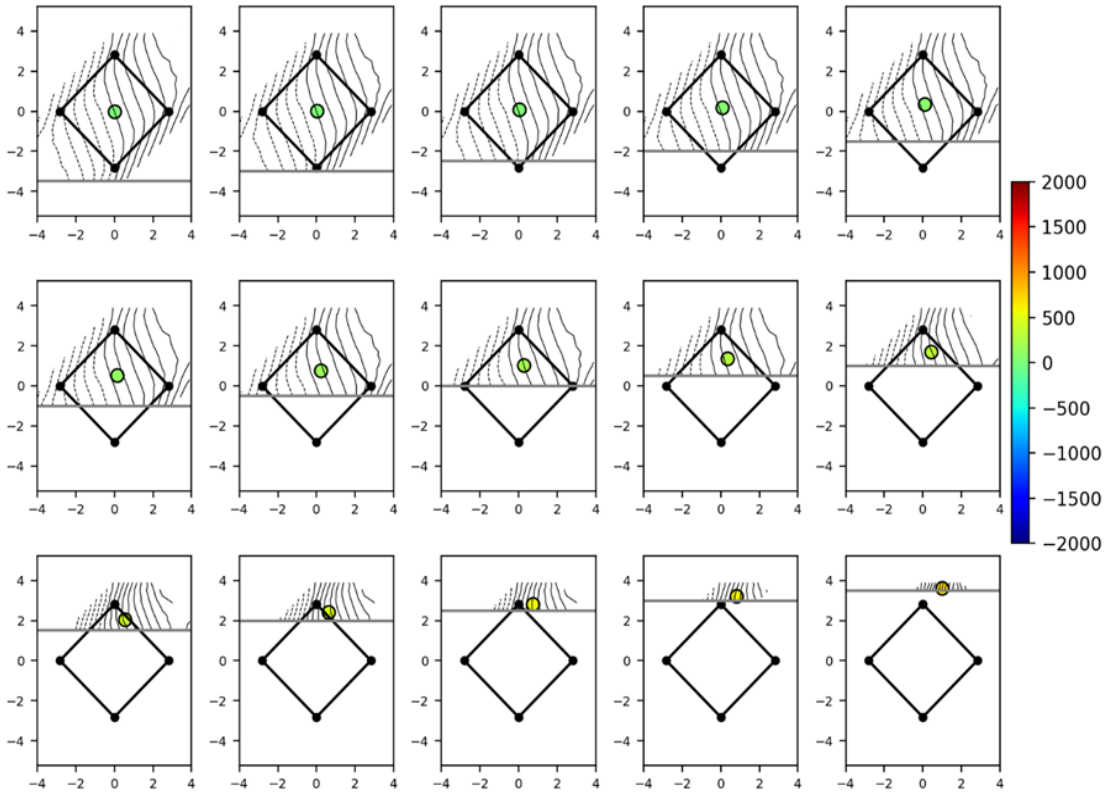

Figure 4.19: The square represents the quoted gauge volume, the circle represents the centre of mass, the colour of the circle represents the strain measured is. The diagram is obtained by calculating weighted average of the data presented in chapter 3. Beam comes from bottom left, bank 1 is in top left. The data represents a scan on B1 in transmission mode but because the centre of mass moves mainly perpendicular to the Q vector there is not much in the way of strain.

The impact on the pseudo strain for bank 1 in reflection due to the NCOG diverging from the geometric centre of the cube when traversing the beam is plotted in Figure 4.20. The square represents the GV used, the circle represents the NCOG, and the colour represents the pseudo strain measured. The calculation is the same as used for the transmission mode and using the data presented in Chapter 3. Now the NCOG moves parallel to the Q vector resulting this time in large pseudo strains.

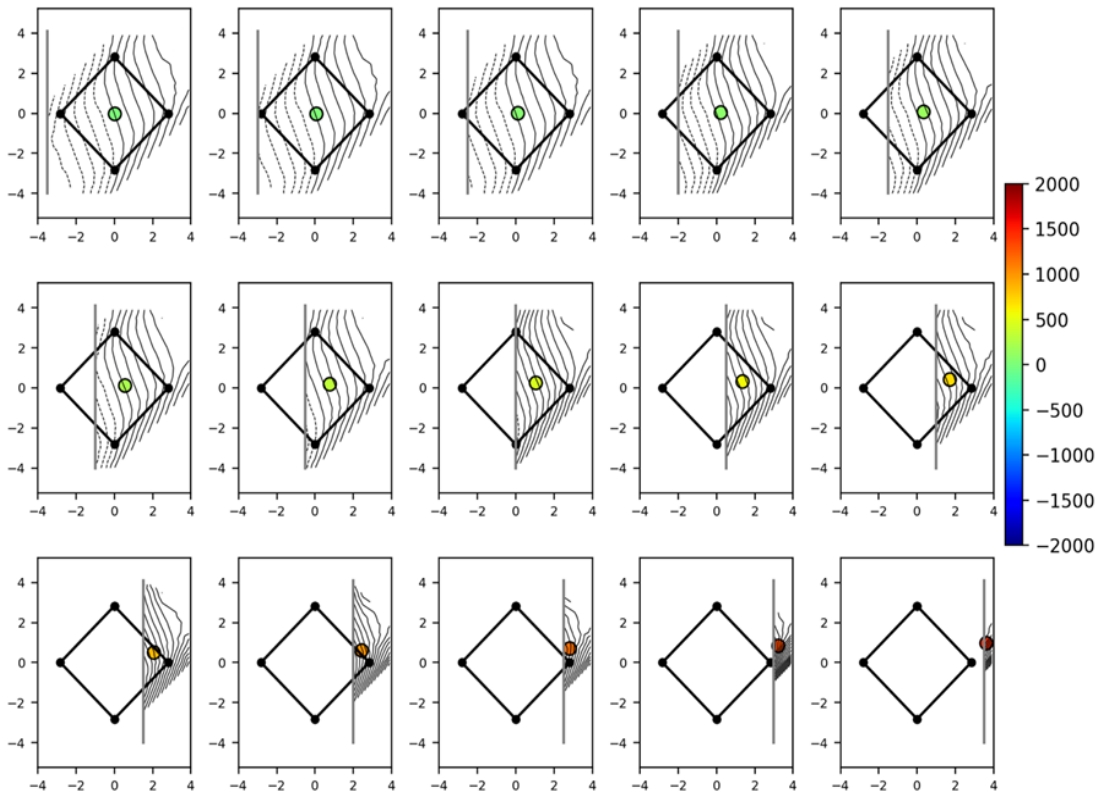

Figure 4.20: The square represents the quoted gauge volume, the circle represents the centre of mass, the colour of the circle represents the strain measured is. The diagram is obtained by calculating weighted average of the data presented in chapter 3. Beam comes from bottom left, bank 1 is in top left. The data represents a scan with B1 in reflection mode, now the NCOG however moves parallel to the Q vector, and this time there is a large amount of strain.

Comparing back to the 2 dimensional strain plots in chapter 2 it is clear that when the scan is in transmission mode (Figure 4.19) the NCOG moves in the plane which corresponds to the region of little pseudo strain in Figure 3.21. On the other hand, when the scan is in reflection mode (Figure 4.20) the NCOG moves in the opposite direction and forms a path into the region of largest pseudo strain. With flat interfaces like those modelled here, this is quite a trivial finding, however, if the interface was more complex, there is a potential to model the movement of the NCOG and predict the potential pseudo strain without the need to run time consuming McStas simulations. It must be remembered however, this data is collected from the pin scan so only takes into account the pseudo strain resulting from geometry and not attenuation.

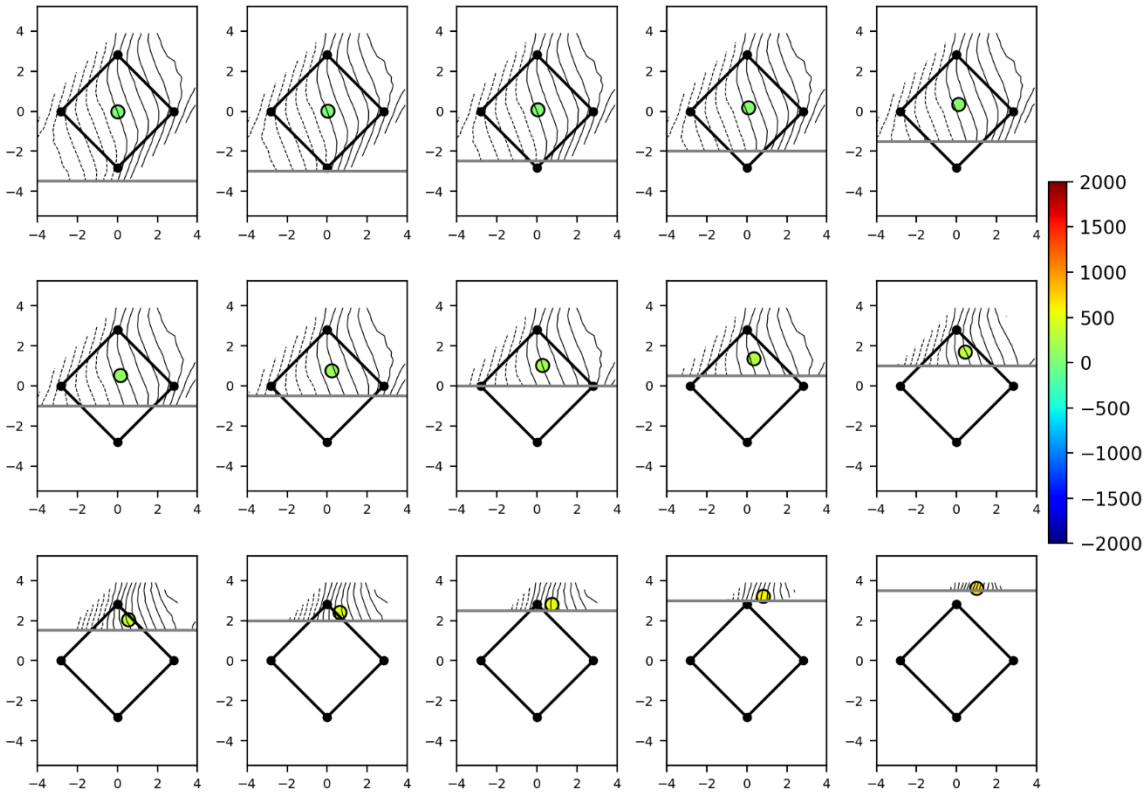

4.5 Conclusions

The comparison of ENGINX measurements and virtual experiments using a powder cube as a sample validates the assumption that McStas can be used to study pseudo strains and provide a quantitative evaluation of the magnitude of the strain and the following conclusions can be made:

- Intensity and pseudo strain can be simulated using McStas with validated sensitivity to diffraction geometry, material and sample design.
- The intensity profile is sensitive to the dimensions of the sample model.
- The intensity profile reproduced during air-material-air scans is sensitive to material properties (density and neutron cross section) in the reflection diffraction geometry but insensitive in transmission.
- The results show that measuring the strain in a sample in two orientations miss-orientated by 180^{o} can mitigate for pseudo strain when the diffraction orientation is in transmission mode but not when in reflection mode.

- In transmission mode pseudo strains and normalised intensities appear to be insensitive to material while in reflection mode both material and geometry have an influence.
- The union concept using the `Union_box` component type in McStas gives the same results for the pseudo strain as using the PowderN component type.
- A z-scan appears to be a useful way of making a pseudo strain free measurement during a surface entrance scan. However due to instrumental constraints this kind of measurement isn't always possible.
- The data obtained from the steel pin grid simulation were used to illustrate the shift of the NCOG versus the geometric centre and how this impacts the pseudo strain depending on whether the bank is in transmission or reflection mode.

5 A validated Monte Carlo simulation of geometric and attenuation aberrations in strain measurements at ENGINX traversing boundaries

5.1 Introduction and motivation

The key objective of this research is to determine to what extent McStas can be used to study pseudo strain such as that which occurs at the surface of a sample, essentially the interface between air and the sample material or that which occurs at the interface of two different materials in an assembly. This section reports the findings of several experiments that have been performed using the 2017 McStas model to characterise the pseudo strain in idealised samples designed to present the above pseudo strains without any other complications. A subset of the virtual experiments have been performed using the ENGINX instrument.

5.2 Methodology

When performing neutron diffraction strain measurements at the interface of air to material and material to material many different aspects need to be covered such as materials to use, the capabilities of McStas and peak fitting techniques. The approach taken is to design virtual experiments that allow the study of specific scenarios with the aim that the outcome of these experiments provide data that can be used to verify assumptions made. The virtual experiments described in this section aim to prove to what extent McStas can be used to study pseudo strain that arises when performing neutron diffraction strain measurement at the interface of different materials. For this chapter, all virtual experiments are performed using the union concept in McStas unless stated otherwise. In all the virtual experiments described and the validation experiments conducted at ENGINX, a gauge volume of 2x2x2mm has been used.

5.2.1 Validation of McStas for interfaces

Although the aim is to study interfaces of different materials the first virtual experiment involves a sample composed of two cubes of equal dimensions and made of the same material. The sample in this virtual experiment traverses the beam under an angle of -135^{o} and the scan points are chosen such that the gauge volume is fully immersed. When the scan reaches the interface the gauge volume will be partially filled with material from each cube. Because the material is identical the assumption is that there will be no pseudo strain. The material used for both cubes is Fe-α with a lattice parameter of 2.88Å and the cubes have dimensions (80x8x8mm) as shown in Figure 5.1.

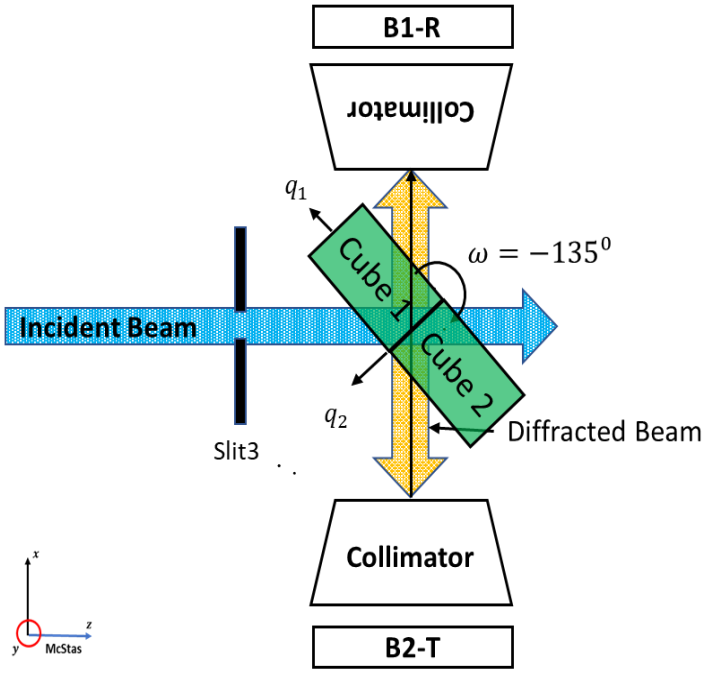

Figure 5.1: Sample model using two cubes each of dimension 80x8x8mm and made of the same material Fe alpha traversing the beam under an angle of 45^o. Two sample models were built, one using the PowderN component type and a second one using the Union_box component type. B1-R and B2-T denote bank 1 and bank 2 are in reflection and transmission with respect to the internal interface.

McStas offers two options to build this sample. The first option uses the component type `PowderN` to model each cube and uses the same McStas MC simulation as is used for all other components in the instrument. The second option is the union concept using the `Union_box` component type to model each cube but now the MC simulation of the sample is done using the MC simulation controlled by the `Union_master` component type. For each option a model was built in McStas.

5.2.2 Material to air

The sample used in this virtual experiment is made up of two cubes of identical dimensions (80x8x8 mm). To study the pseudo strain that arises near an air to material interface the union concept is used. Each cube is represented using the Union_box component type. The material used for cube 1 is Fe-γ and is defined in the materials section of the union concept using the reflection file `Fe_Gamma.laz` which holds the physical properties of the material and its crystallographic information. In the materials section the scattering processes to use are defined and the magnitude of the cross sections. To simulate 'air', the material of cube 2 is set to `Vacuum`. An illustration of the experiment set up is shown in Figure 5.2. From the interface perspective bank 1 is now in reflection mode and bank 2 in transmission mode. The same virtual experiment was repeated but now using as material for cube 2 Fe alpha and the material in cube 1 set to `Vacuum.` The reflections file used for Fe-α is `Fe.laz`. The lattice parameter used for Fe-γ is 3.64Å and the lattice parameter for Fe-α is 2.88 Å.

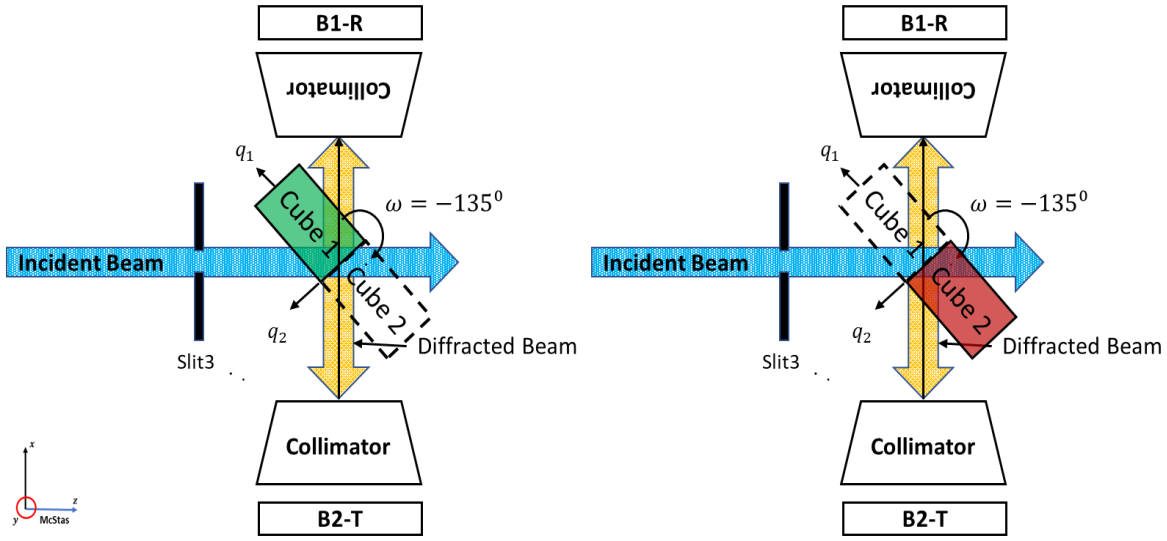

Figure 5.2: Sample model on LHS is used for material to air scan with material cube 1 Fe-γ and material cube 2 set to Vacuum. Sample model on RHS is similar but material cube 1 now set to Vacuum and material cube 2 Fe-α. Both samples traverse the beam under an angle of 45^o.

Different scenarios are simulated to investigate various aspects that may influence the magnitude of the pseudo strain like the impact of the detector banks, particularly how the results compare depending on the detector being in transmission or reflection mode. The different scenarios are summarized in Table 5.1.

Table 5.1: Experiments performed for air to material and material to air.

Description	Material	ω	Scan range, step size mm	#Scan points	Scope
Horizontal scan across beam	Vacuum/Fe-α	-135	$x[-8,8,0.5]$	25	Virtual/Exp
Horizontal scan across beam	Vacuum/Fe-α	45	$x[-8,8,0.5]$	25	Virtual/Exp
Horizontal scan across beam	Fe-γ/Vacuum	-135	$x[-8,8,0.5]$	25	Virtual/Exp
Horizontal scan across beam	Fe-γ/Vacuum	45	$\boldsymbol{x[-8,8,0.5]}$	25	Virtual/Exp

5.2.3 Material to material

The same sample model used to study pseudo strain in an air to material interface can also be used for a material to material interface. A virtual experiment was performed using for cube 1 as material Fe-γ with lattice parameter 3.64Å and for cube 2 Fe-α with a lattice parameter of 2.88 Å. Both cubes had the same dimensions (80x8x8mm) as illustrated in Figure 5.3.

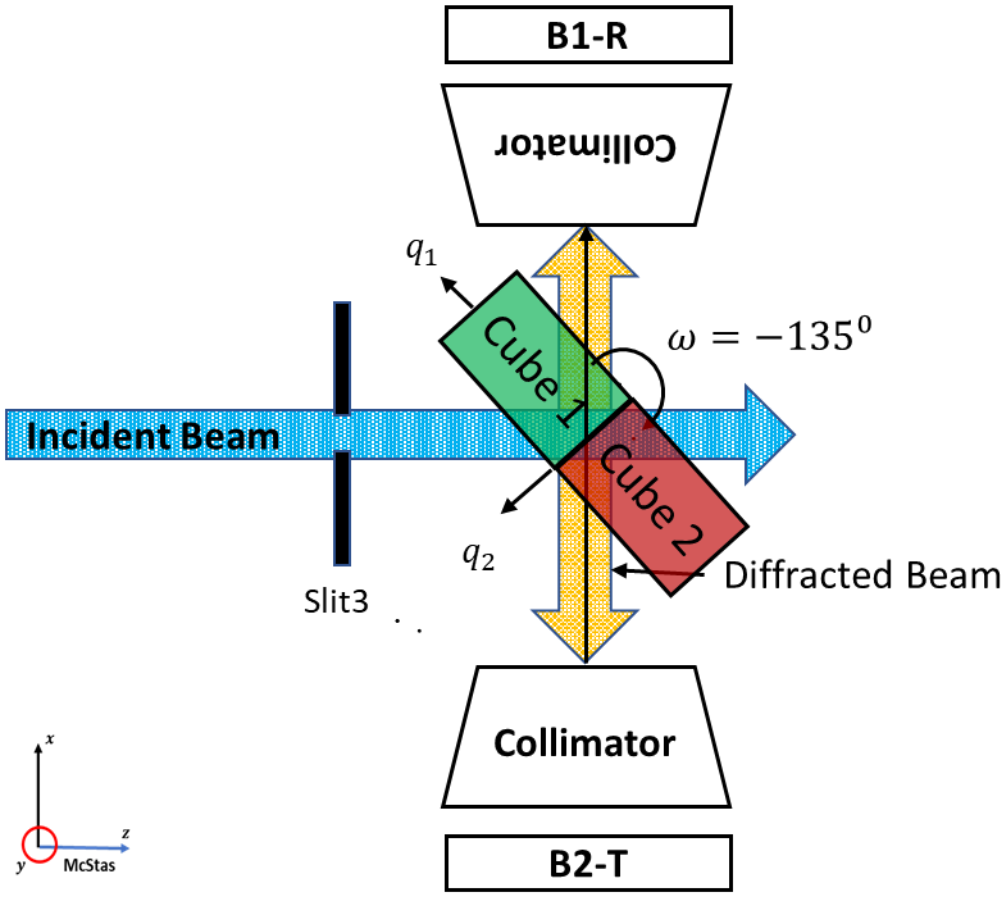

Figure 5.3: Sample model using two cubes of 80x8x8mm. Cube 1 is made of Fe-γ and cube 2 of Fe-α . The sample traversed the beam under an angle of 45^o and -135^o. The sample model was built using the Union_box component type.

The significant difference in lattice parameters and crystal structures reduces the problem of overlapping peaks which can be a challenge when performing the peak fitting. This set of materials was chosen to validate McStas can be used to study pseudo strain in material to material interface and predict the magnitude of the pseudo strain. This virtual experiment was also performed on the real ENGINX instrument. The simulations and experiments performed are summarised in Table 5.2.

Table 5.2: Experiments performed for material to material

Description	Material	ω	Scan range, step size mm	#Scan points	Scope
Horizontal scan across beam	Fe-γ / Fe-α	-135^o	$x[-8,8,0.5]$	25	Virtual/Exp
Horizontal scan across beam	Fe-γ / Fe-α	45^o	$\boldsymbol{x[-8,8,0.5]}$	25	Virtual/Exp

For the sample positions with overlapping peaks the multi-phase fitting in OpenGenie was used applying a weighting to each material. The weighting used was taken from the Fe-α to air and air to Fe-γ intensities at the same sample position.

5.3 Results

5.3.1 Validation of McStas for interfaces

The simulation done using the PowderN component type and the simulation conducted with the union concept are shown in Figure 5.4. The PowderN simulation shows a small but significant pseudo strain for sample position between -1.4 and +1.4mm with a maximum of 55 micro strain at the interface. By contrast, the simulations conducted using a sample constructed using the union concept simulation present an essentially flat response with variations well within the expected scatter.

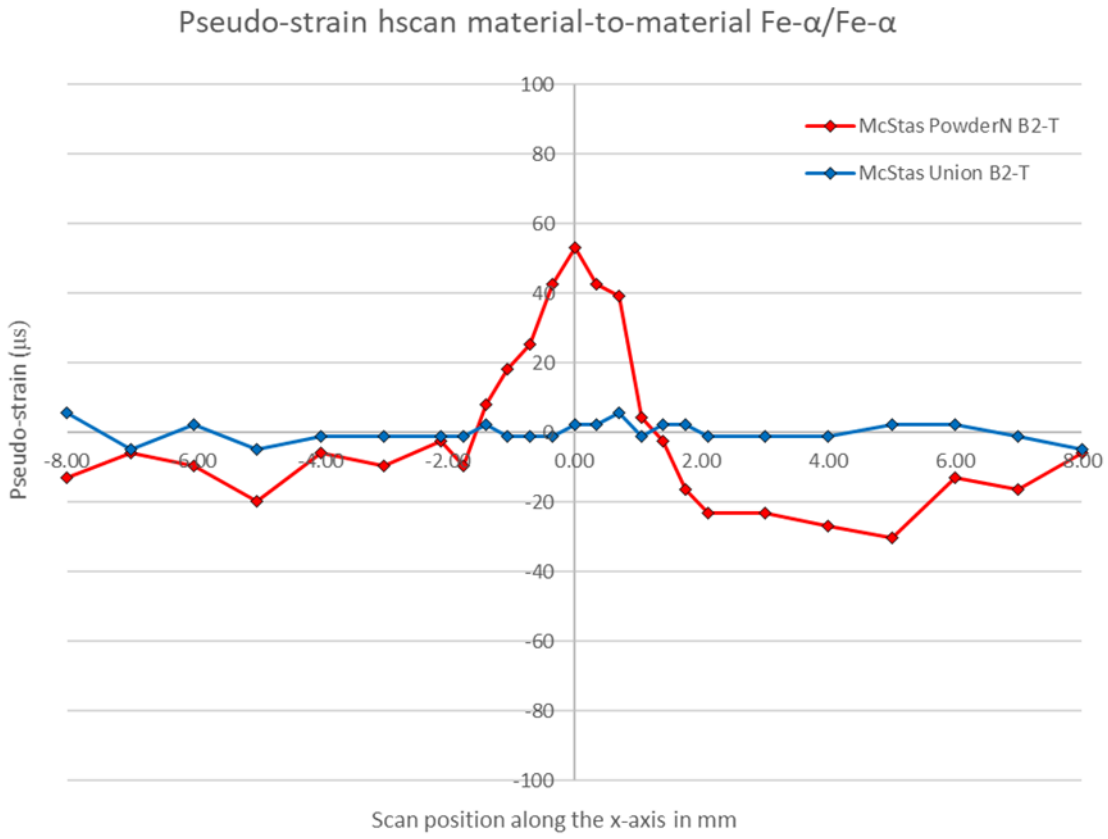

Figure 5.4: Pseudo strain bank 2 for interface consisting of two cubes (80x8x8mm) made of the same material Fe-α. One simulation used PowderN in McStas, the other used the union concept in McStas. The PowderN simulation shows a small but significant pseudo strain for sample position between -1.4 and +1.4mm with a maximum of 55με at the interface. The simulation results conducted using the union concept present an essentially flat response.

The intensity profile of detector bank 2 for both simulations is shown in Figure 5.5. The PowderN simulation is showing an intensity that is fluctuating starting with a lower intensity for points less than-2.8mm followed by an increase from this point until it passes the interface point from about 1mm

onwards the intensity stays the same. In contrast the intensity profile using the union concept stays essentially flat.

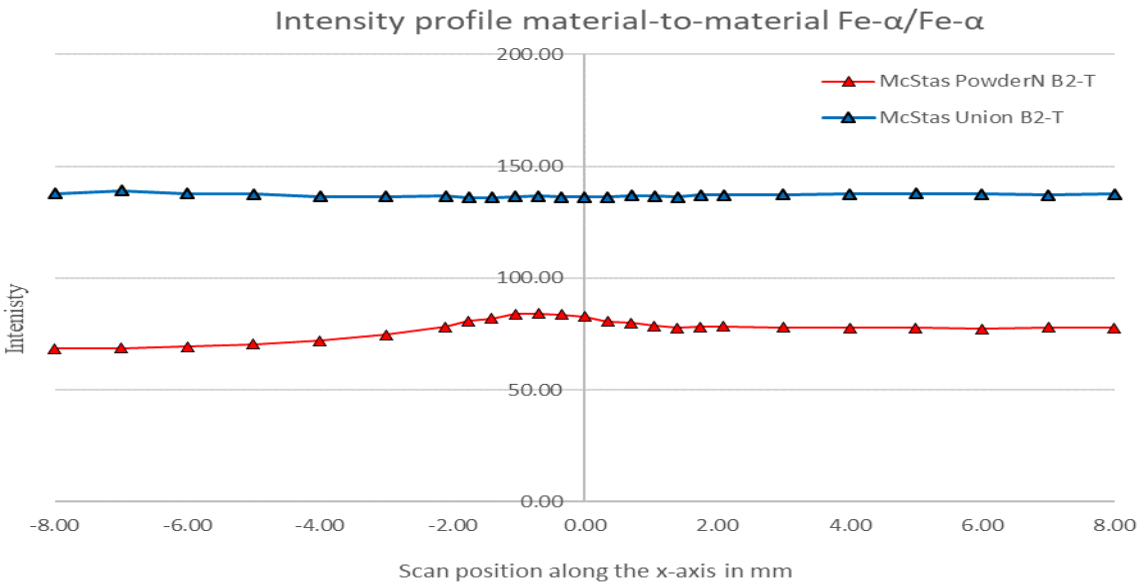

Figure 5.5: The intensity profile of the PowderN simulation fluctuates, starting from -8mm it gradually increases and reaches a maximum at -1 mm after which it gradually declines until it reaches 1mm from then on it remains flat. The intensity profile for the union concept simulation remains essentially flat.

5.3.2 Material to air

The pseudo strain results bank 1 for a material to air interface are shown in Figure 5.6. The material is an iron powder cube (8x8xx40mm) and made of Fe-α. For sample positions larger than -1mm the ENGINX pseudo strain values are larger than from the McStas simulation. The McStas simulation with the sample 180^{o} rotated are as expected.

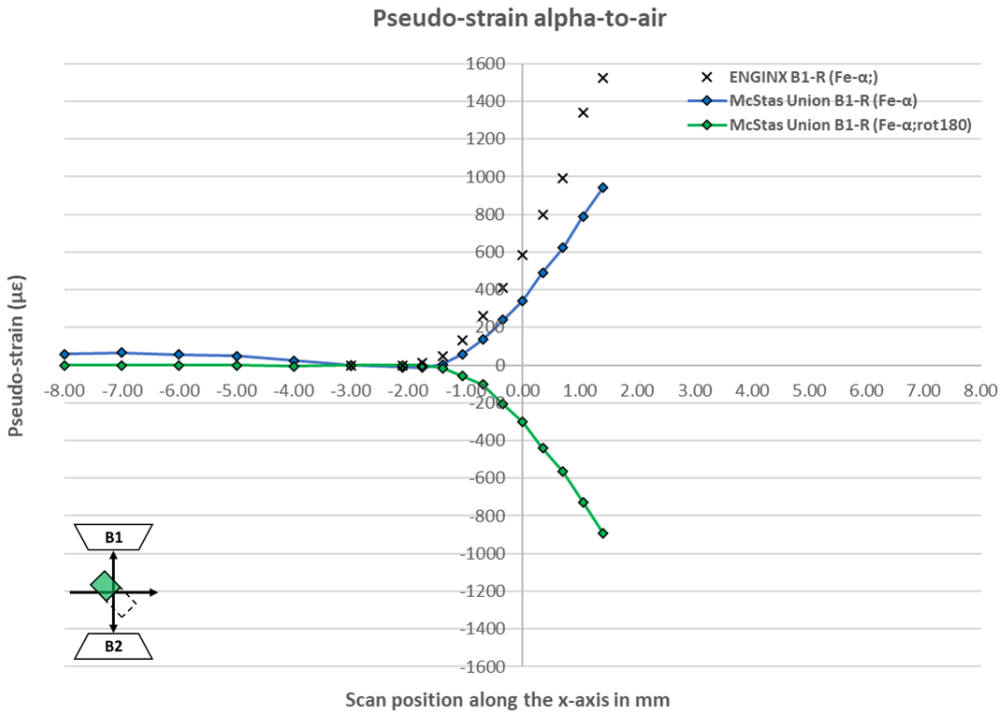

Figure 5.6: Pseudo strain bank 1 for an air to material interface using as material Fe-α. For sample positions larger than -1mm the ENGINX pseudo strain values are larger than from the McStas simulation. The McStas simulation with the sample 180° rotated are as expected.

The pseudo strain bank 2 results for a material to air interface are shown in Figure 5.7. The simulation results bank2 diverge significantly from those measured with ENGINX for sample positions larger than -0.7mm. Bank 2 is in in transmission mode.

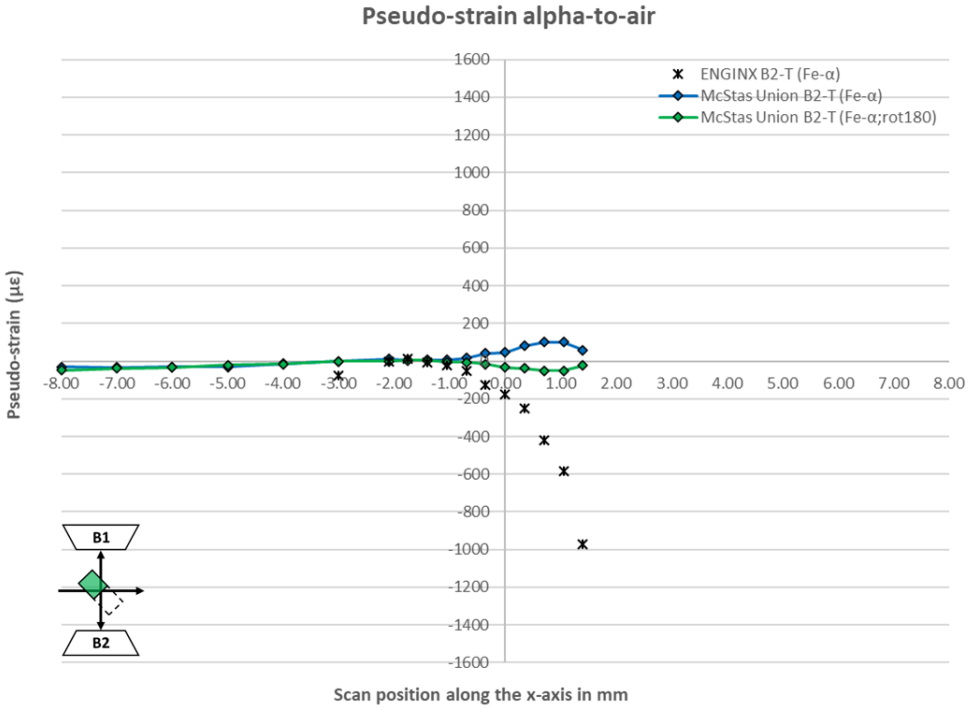

Figure 5.7: Pseudo strain bank 2 for an air to material interface using as material Fe alpha. For sample positions larger than -1mm the ENGINX pseudo strain values are much larger than from the McStas simulation. The McStas simulation with the sample 180^o rotated gives very small pseudo strains and or of the same order of magnitude as the fitting error.

Intensity profiles bank 1 and bank 2 for air to material interface with as material Fe-alpha are shown in Figure 5.8. The intensities for bank 1 when the sample is rotated 180^o are significantly smaller than for the non-rotated sample when the sample position is between -3 and 1mm. For bank 2 there is no difference in the intensities between the non-rotated sample and the 180^o rotated sample.

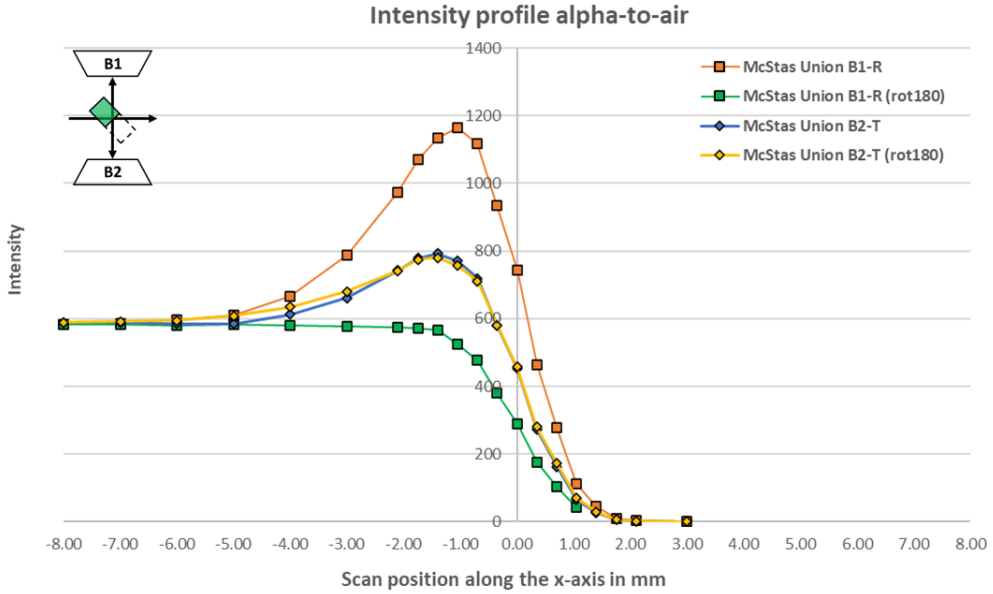

Figure 5.8: Intensity profile for bank 1 and bank 2 for air to material interface using as material Fe-α .

The results for the material to air scan for bank 1 with as material Fe-γ are shown in Figure 5.9. Bank 1 is in reflection mode. For sample positions smaller than 1mm the ENGINX pseudo strain values are more negative than from the McStas simulation. When the sample is rotated 180^{o} the results are as expected.

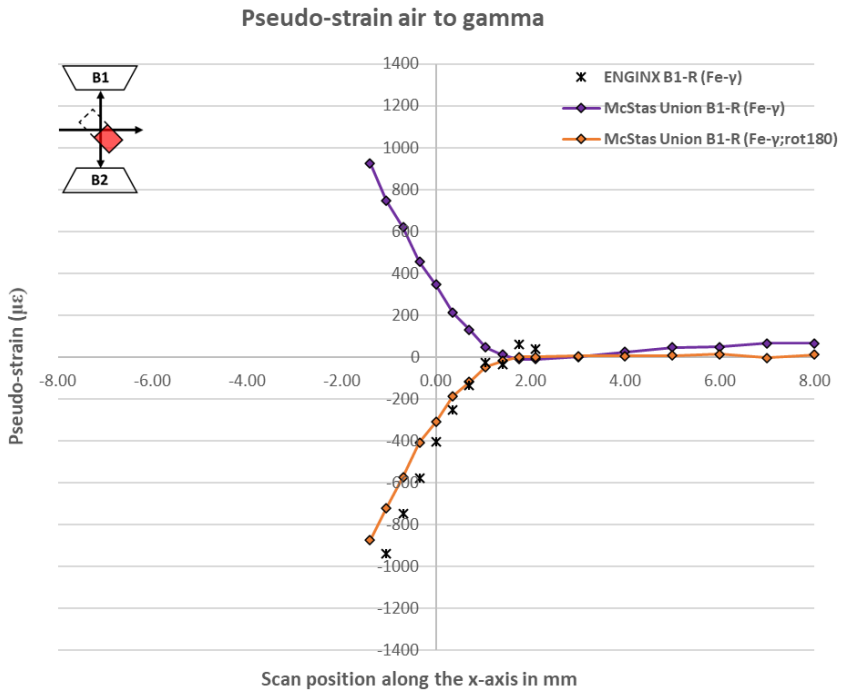

Figure 5.9: : Pseudo strain bank 1 for an air to material interface using as material Fe-γ. Bank 1 is in reflection mode. For sample positions smaller than 1mm the ENGINX pseudo strain values are more negative than the McStas simulation values. The pseudo strain values for the McStas simulation with the sample 180^{o} rotated are as expected.

The results for the material to air scan for bank 2 with as material Fe-γ are shown in Figure 5.10. Bank 2 is in transmission mode. For sample positions smaller than 1mm the ENGINX pseudo strain values are more negative than from the McStas simulation. When the sample is rotated 180^{o} the results are as expected.

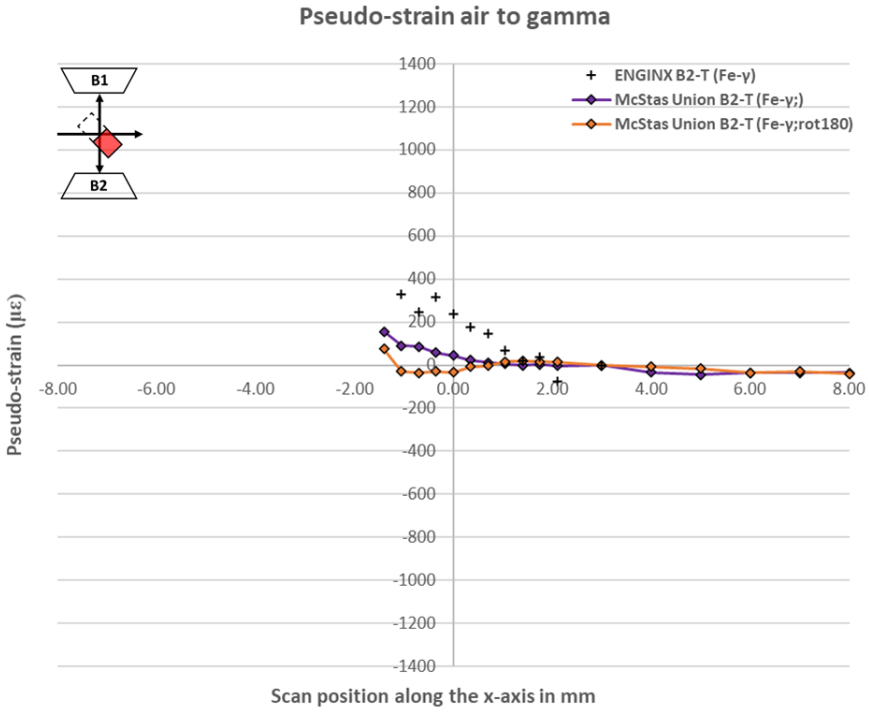

Figure 5.10: Pseudo strain bank 1 for an air to material interface using as material Fe-γ. Bank 1 is in reflection mode. For sample positions smaller than 1mm the ENGINX pseudo strain values are larger than the McStas simulation values. The pseudo strain values from the McStas simulation with the sample 180^{o} rotated are small and in the order of magnitude of the fitting error.

5.3.3 Material to material

The pseudo strain bank 1 results for a material to material interface are shown in Figure 5.11. Bank 1 is in reflection mode. The interface consisted of two iron powder cubes each of dimension (8x8x40mm) with one cube Fe-α and the other Fe-γ. For Fe-α the ENGINX results start at sample position -2.1mm and for McStas at -8mm. The ENGINX pseudo strains are larger than the McStas values for sample positions between -2.1 and -1.4mm and from 0.7mm onwards when the difference increases significantly, while between -1.05 and 0.35 mm it is the reverse. For Fe-γ the ENGINX results start at -1.4mm and the last sample position measured is 2.1mm, for McStas it starts at -1.75mm and the last sample position is 8mm. The pseudo-strains are larger for McStas between -1.75 and -0.35mm, and it is the reverse between 0 and 1.4mm. The shape of the McStas curves is similar to the ENGINX one. For the sample positions with overlapping peaks multi-phase fitting was used applying a weighting to each material. The weighting used was taken from the Fe-α to air and air to Fe-γ intensities at the same sample position. The peaks overlap for sample positions between -1.4 and +1.4mm, for the other sample positions the overlap is negligible and single-phase fitting was applied.

The results show strain profiles similar to those of the respective material-to-air profile. There are however some irregularities in the data which appear to result from the fitting procedures. It should

be pointed out that in most practical cases it would be assumed impossible to extract strains from two materials with an imbedded boundary. Therefore, these results are very pleasing despite the irregularities.

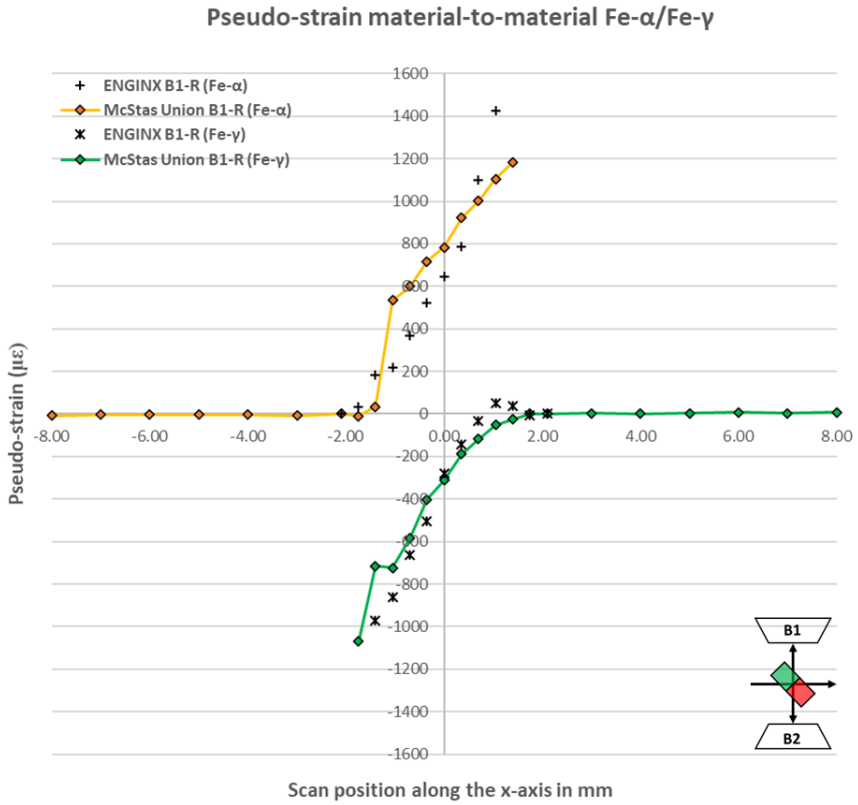

Figure 5.11: Pseudo strain bank 1 for a material to material interface. Bank 1 is in reflection mode. The interface is made up of two iron powder cubes both of dimensions (8x8x40mm) with one cube Fe-α and the other Fe-γ material

5.4 Discussions

The results of the material to material interface where both materials are the same shows that using the PowderN component type in McStas provides incorrect results as in this case there should not be any pseudo strain. The union concept shows the correct result. A possible explanation why the PowderN component type does not give the correct result may be that the calculation of the intersection of the neutron ray with material of cube 1 near the boundary is undetermined due to the closeness of the material of cube 2. The union solves this issue by having the cubes slightly overlapping at the interface and uses the priority parameter to indicate close to the interface which material should have precedence when calculating the intersection.

The air to material interface shows a divergence for both materials between the results obtained from the simulation with McStas and the equivalent experiment performed with ENGINX. This divergence can be attributed partially to the material definitions used in the simulation not exactly matching the

physical properties of the physical material like the density and the scattering and absorption cross sections. The results of the experiment show an irregular pattern that seems to indicate that the sample was not correctly aligned with the beam when the experiment was set up causing a possible systemic shift in the pseudo strain results.

The magnitude of the McStas pseudo strains for the air to Fe-α interface with bank 1 or bank 2 in reflection mode is significantly smaller than when they are in transmission mode. This is counter to the results shown for the single cube. The density of the single cube was 41%, while the materials used in the air to material interface are solid which results in a much larger attenuation which could go some way to explain the difference as the neutron path length in reflection mode on average is significantly longer than in transmission.

The results for the material to material interface show that using multi-phase fitting and a weighting based on intensity obtained from the air to material / material to air measurements can be used to do the fitting of overlapping peaks. More measurements and using materials where the lattice parameters are very close to each other need to be done to validate this method is robust enough.

5.5 Conclusions

The virtual experiments done show that McStas can be used to study the strain in air to material and material to material interfaces. The results obtained from the McStas provide useful insight and confirm what is known from other methods what causes the pseudo strain and provide a quantitative evaluation of the magnitude of the strain and the following conclusions can be made:

- To study material to material interfaces the union concept in McStas must be used
- The pseudo strain results of the air to material/ material to air simulations do not match the results of the experiments performed with ENGINX but the shape of the pseudo strain curves is similar between McStas and ENGINX.
- The intensities obtained with the air to material and material to air simulations can be used as a relative weighting in multi-phase peak fitting of the material to material interface. This method needs more validation particularly when using materials with lattice parameters that are very close to each other but has the potential to save beam time in real experiments by not having to perform air to material scans.
- The pseudo strain for the material to material interface are in line with ENGINX results and show that with a more accurate definition of the materials it may be possible to make predictions of the pseudo strain arising using McStas

6 Influence of metallurgical heterogeneity on neutron diffraction residual stress uncertainty

6.1 Introduction and motivation

Another feature present in many welds are small voids or pores and large grains. Small voids within the gauge volume act as a region not diffracting and therefore potentially cause the gauge volume centre of mass to differ from the one assumed[83]. A single grain on the other hand has the potential to have several effects. The first being a region, that for a specific reflection, does not diffract, and the second, for other reflections being a region that diffracts extremely strongly. Both could result in a similar misinterpretation of the gauge volume centre of mass. The virtual experiments described in this section focus on pseudo strain occurring due to the presence of small voids or pores in the material.

6.2 Methodology

To study the pseudo strain that may arise when measuring strain in welds of different materials several virtual experiments have been designed and modelled that aim to provide insight in the magnitude of these pseudo strains and what influences the magnitude. The aim of the experiments was to study the effect of individual grains and individual pores on pseudo strain which involves two aspects the size of the pore or grain and the material the grain is made of. The first virtual experiment was designed to verify the effect of the size of a region of non-diffracting and non-attenuating material on the pseudo strain. This was achieved by creating a sample consisting of a nickel powder cube (8x8x40mm) with a cylindrical hole in the centre of the cube. A second virtual experiment was performed using a nickel powder cube with a cylindrical hole positioned ex-centric. In this case the hole was positioned 1.5 mm of the centre of the cube. A picture of the real sample is shown in Figure 6.1.

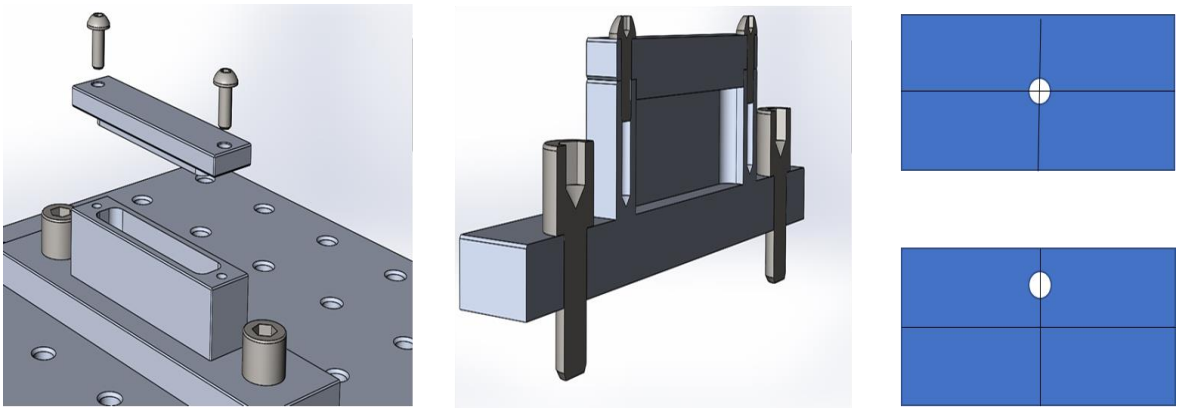

Figure 6.1: The model of the real sample used. The container was manually filled with nickel powder. In the lid covering the container two holes of 1mm diameter where drilled, one in the centre of the lid, the second 1.5mm of the centre as shown in the picture on the right. An Al-wire was pushed through the hole to create a hole in the nickel powder.

A schematic of the sample set up used to perform the experiments is shown in Figure 6.2.

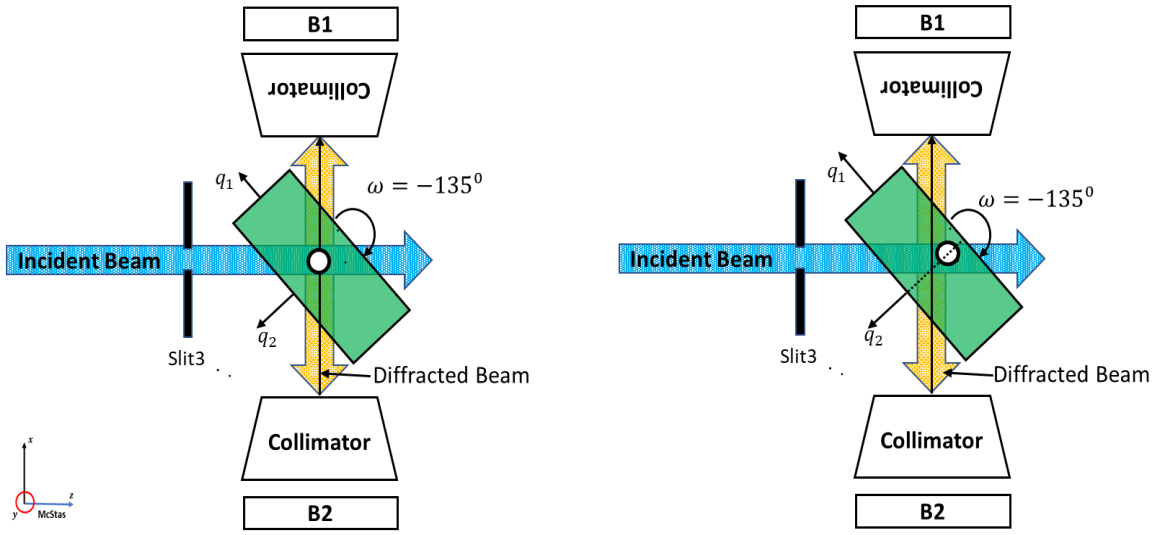

Figure 6.2: The sample set up for a nickel power cube (8x8x80mm) with a cylindrical hole. The hole in picture on the left is in the centre, the hole in the picture on the right is ex-centric and has been moved by 1.5mm from the centre of the cube along q_2 but in opposite direction. The radius in the real experiment was 500µm, for the virtual experiments the radius used was 75, 125, 250, 500 and 750µm. The hole in the real experiment was filled with an Al-wire, in the virtual experiment the hole was Vacuum in all simulations apart of one in which the hole was filled with Al powder.

The virtual sample model was designed such that the radius of the hole and the material of the hole could be varied. Using this capability simulations could be performed using different combinations of the radius of the hole and the GV. The ratio of the area of the hole and the area of the GV for a range of different radii and GV's are shown in Table 6.1.

Table 6.1: The ratio of the area of a cylindrical hole and the area of the GV.

Ratio area hole / GV (%)	Radius (µm)				
GV (mm)	75	125	250	500	750
2	0.4%	1.2%	4.9%	19.6%	44.2%
3	0.2%	0.5%	2.2%	8.7%	19.6%
4	0.1%	0.3%	1.2%	4.9%	11.0%

Unfortunately, it is physically impossible to place a region of vacuum within a cube of powder for the purpose of validation. Therefore, the real experiment with ENGINX used also a nickel powder cube but the vacuum hole was replaced with an Al-wire. This was also simulated using the virtual sample in McStas with the cylindrical hole filled with aluminium powder for the purpose of comparison. The neutron cross-section of aluminium is very low compared to Nickel, therefore was thought to be a reasonable compromise. The different experiments performed are summarised in Table 6.2 .

Table 6.2: Different experiments performed for a nickel powder cube (8x8x80mm) with a cylindrical hole. All experiments involved a horizontal scan under an angle across the beam with scan in steps of 0.5mm from -8 to +8mm.

Material hole	Radius hole µm	Hole position	IGV mm	ω	Scope
Vacuum	75,125,250,500	Centre	2	45	Virtual
Vacuum	125,250,500,750	Centre	3	45	Virtual
Vacuum	250,500,750	Centre	4	45	Virtual
Aluminium	500	Centre	4	45/-135	Virtual/Exp
Vacuum	500	Centre	4	45/-135	Virtual
Vacuum	500	Off-centre	4	45/-135	Virtual

6.3 Results

6.3.1 Effect of a concentric vacuum hole on pseudo strain

The effect of a vacuum hole in the centre of the cube on the pseudo strain when using a GV of 2 mm is shown in Figure 6.3. For a hole with a radius of 125µm the effect on the pseudo strain is negligible

evident by the almost continuous line plotted in Figure 6.1 not really exceeding the scatter. For hole with a radius of 250µm there is a visible effect on the pseudo strain with a minimum of -20µε and a maximum of 20µε, and for a hole with a radius of 500µm the effect is more pronounced with a minimum of -50µs and a maximum of 40µε. The shape of the pseudo strain curves between where the hole enters the gauge volume (x=-1.4mm) and where it leaves the gauge volume (x=1.4mm) are similar and symmetric versus the centre (x=0).

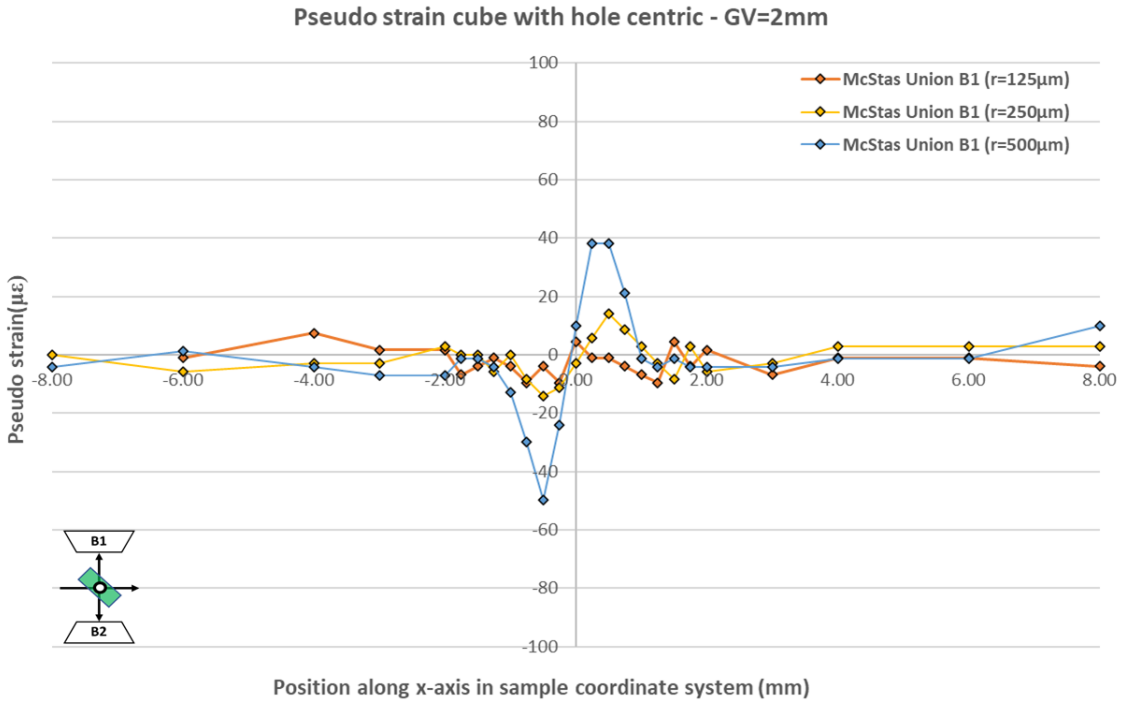

Figure 6.3: Pseudo strain results of a McStas simulation using a nickel powder cube (8x8xx80mm) with a vacuum hole in the centre using a GV of 2mm. Three different radii resp, 125, 250 and 500µm were simulated. The larger the ratio of the area of the hole vs the area of the GV the larger the pseudo strain is

The effect of a vacuum hole in the centre of the cube on the pseudo strain when using a gauge volume of 3mm becomes visible when the radius of the hole is 250µm or larger as shown in Figure 6.4. For a hole with a radius of 250 the pseudo strain reaches a minimum of ~-10µε and a maximum of ~10µε. For the holes with a larger radius the effect on the pseudo strain is larger. For the 500µm hole the minimum pseudo strain is -40µε and the maximum pseudo strain is 40µε. For the 750µm the minimum pseudo strain is -80µm and the maximum pseudo strain is 90µm. The minimum and maximum pseudo strain for all three holes is reached at positions, x=-1mm and x=1mm. The holes enter the gauge volume at x=-2.1mm and leaves at x=2.1mm.

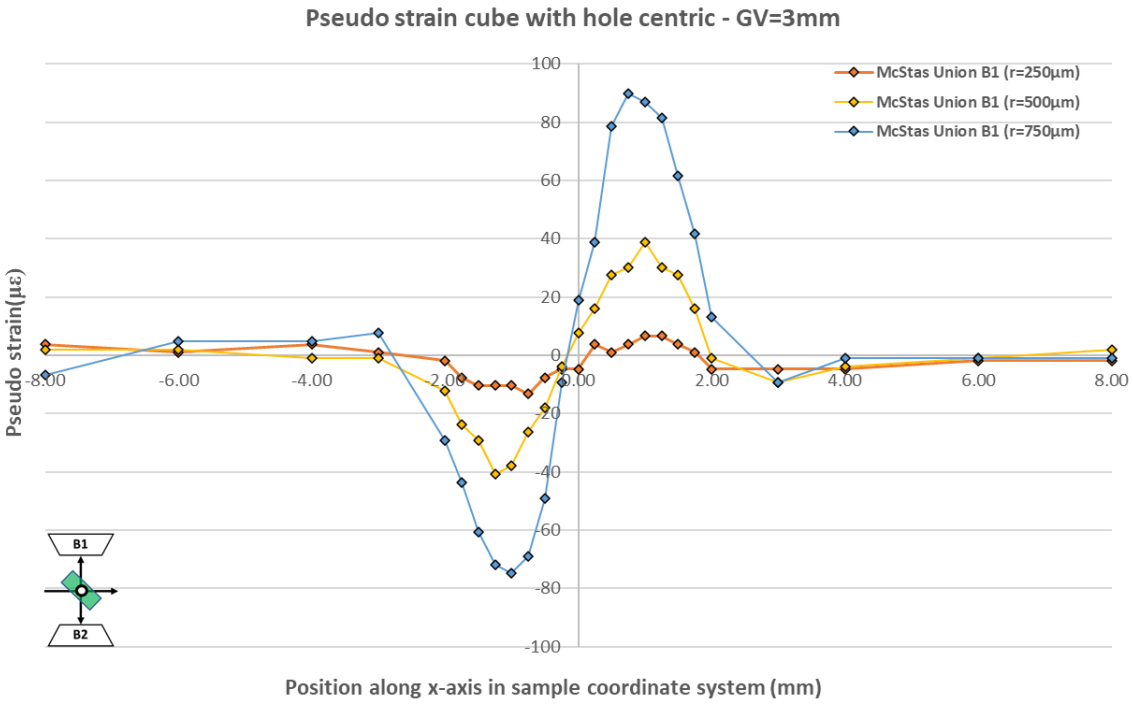

Figure 6.4: Pseudo strain results of a McStas simulation using a nickel powder cube (8x8x80) with a vacuum hole in the centre using a GV of 3mm. Three different radii resp, 250, 500 and 750µm were simulated. The larger the ratio of the area of the hole vs the area of the GV the larger the pseudo strain is.

The effect of a hole on the pseudo strain when using a gauge volume of 4mm becomes visible when the radius of the hole is 500µm or larger as shown in Figure 6.5. For a hole with a radius of 500 the pseudo strain reaches a minimum of ~-35µε and a maximum of ~30µε. For the 750µm hole the minimum pseudo strain is -40µε and the maximum pseudo strain is 40µε. For the 750µm the minimum pseudo strain is -60µε and the maximum pseudo strain is 70µε. The minimum and maximum pseudo strain for all three holes is reached at positions, x=-1mm and x=1mm. The holes enter the gauge volume at x=-2.8mm and leaves at x=2.8mm.

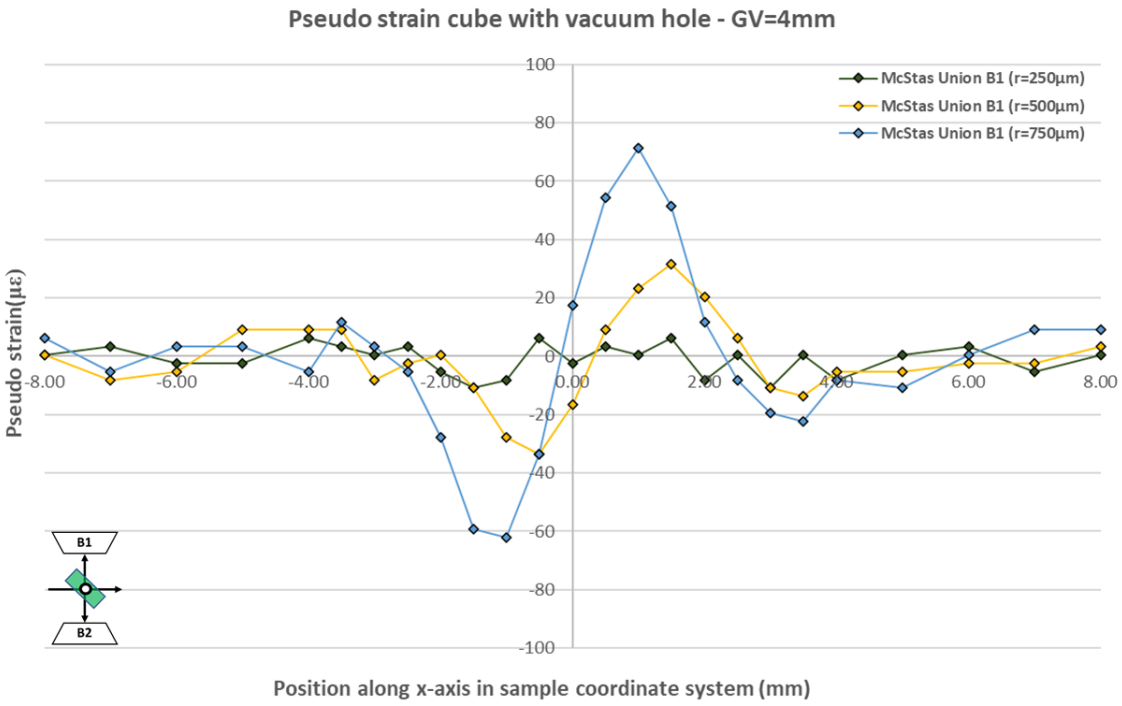

Figure 6.5: Pseudo strain results of a McStas simulation using a nickel powder cube (8x8xx80mm) with a vacuum hole in the centre using a GV of 4mm. Three different radii resp, 250, 500 and 750µm were simulated. The larger the ratio of the area of the hole vs the area of the GV the larger the pseudo strain is.

6.3.2 Pseudo strain vacuum hole versus Al-wire

In the real experiments the hole in the cube was represented by an aluminium wire of 500µm. The effect on the pseudo strain using an Al-wire to fill the hole in the centre of the cube is shown in Figure 6.6. The pseudo strain in the McStas simulation reaches a minimum for the Al-wire of -30µε at -1.5mm, and for a vacuum hole the minimum is close to -40µε at -0.5mm. The pseudo strain reaches a maximum for the Al-wire of 25µε at 1mm and for a vacuum hole the maximum is 30µε at 1.5mm. The pseudo strain using ENGINX reaches a minimum of -40µε at -1mm and a maximum of 80µε at 1mm.

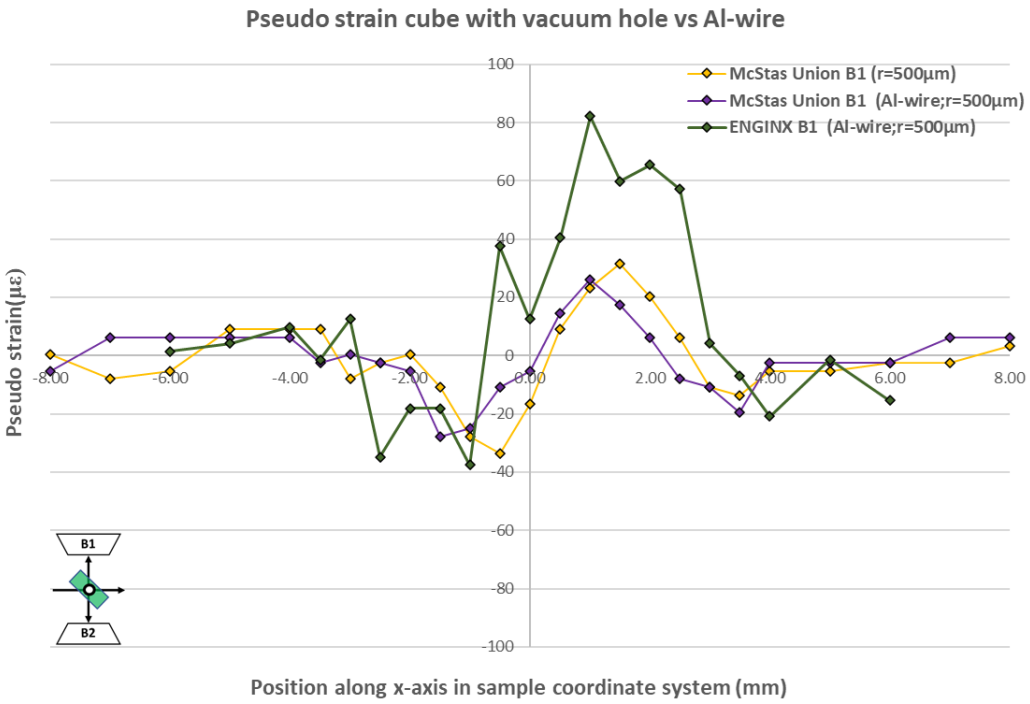

Figure 6.6: Pseudo strain arising from a cylindrical hole with a radius of 500µm in a nickel powder cube (8x8x80) using a 4mm GV. The McStas simulation of the Al-wire compared against the vacuum hole shows that the minimum pseudo strain for the Al-wire is -30µε at -1.5mm, and for vacuum hole this is close to -40µε at -0.5mm. The maximum pseudo strain for the Al-wire is 25µε at 1mm and for vacuum hole this is 30µε at 1.5mm. The pseudo strain using ENGINX reaches a minimum of -40µε at -1mm and a maximum of 80µε at 1mm.

6.3.3 Effect of vacuum hole off-centre on pseudo strain

The pseudo strain for a nickel powder cube (8x8x80mm) containing an off-centre cylindrical hole with a radius of 500µm are shown in Figure 6.7. The results of the off-centre hole are compared with the pseudo strain for a nickel powder cube with a cylindrical hole in the centre and with the results when the sample with the off-centre hole is rotated 180^{o}. For sample positions less than 0 the off-centre hole does not give rise to pseudo strain when the sample position is larger than 0 there is pseudo strain reaching a maximum of ~40µε between 1 and 1.5mm. The pseudo strain for the off-centre hole with sample positions between 0 and 3mm is about 10µε larger than for the hole in the centre. When the sample with off-centre hole is rotated 180^{o} the pseudo strain for positions less than 0 can beignored as it is of the same magnitude as the fitting error, for positions larger than zero there is negative pseudo strain reaching a minimum of -40µε at 1.5mm.

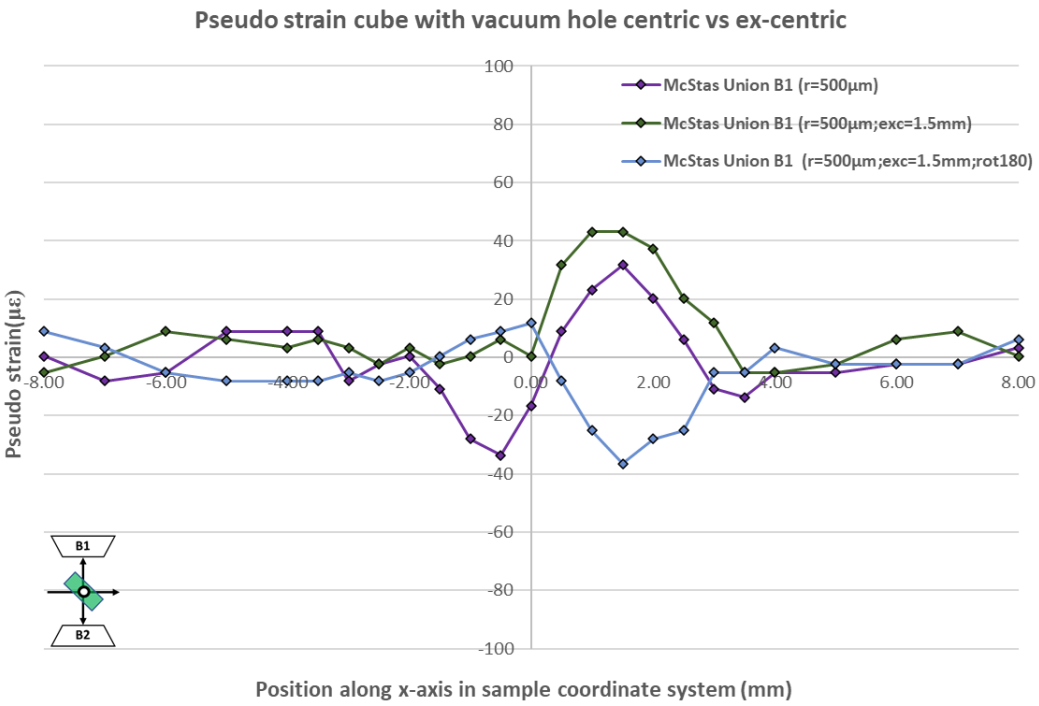

Figure 6.7: Pseudo strain for a nickel powder cube (8x8x80) with an off-centre cylindrical hole with a radius of 500µm and when rotated 180°. For comparison the pseudo strain for a hole in the centre is also shown. For the off-centre hole there is no pseudo strain for sample positions less than 0, for positions larger than 0 pseudo strain is present in both orientations but opposite in sign. The pseudo strain for the off-centre hole with sample position between 0 and 3 mm is about 10µslarger than for the hole in the centre at the same positions.

6.3.4 Pseudo strain rotating sample 180°

The pseudo strain bank 1 for a sample consisting of a nickel powder cube (8x8xx80) containing a vacuum hole with a radius of 500µm in the centre using a 4mm GV, and with the sample 180° rotated is shown in Figure 6.8**.** The pseudo strain for the non-rotated sample is negative between -2mm and 0.5mm reaching a minimum of ~-40µε at -0.5mm and is positive between 0.5mm and 2.5mm reaching a maximum of 35µε at 1.5mm. The sample rotated 180° has positive pseudo strain between -2mm and 0.5mm reaching a maximum of 35µε at -1.mm, and negative pseudo strain between 0.5mmm and 2.5mm reaching a minimum of -25µε at 1mm. For sample positions less than -2mm and larger than 2.5 mm the pseudo strain can be ignored being too small relative to the fitting error.

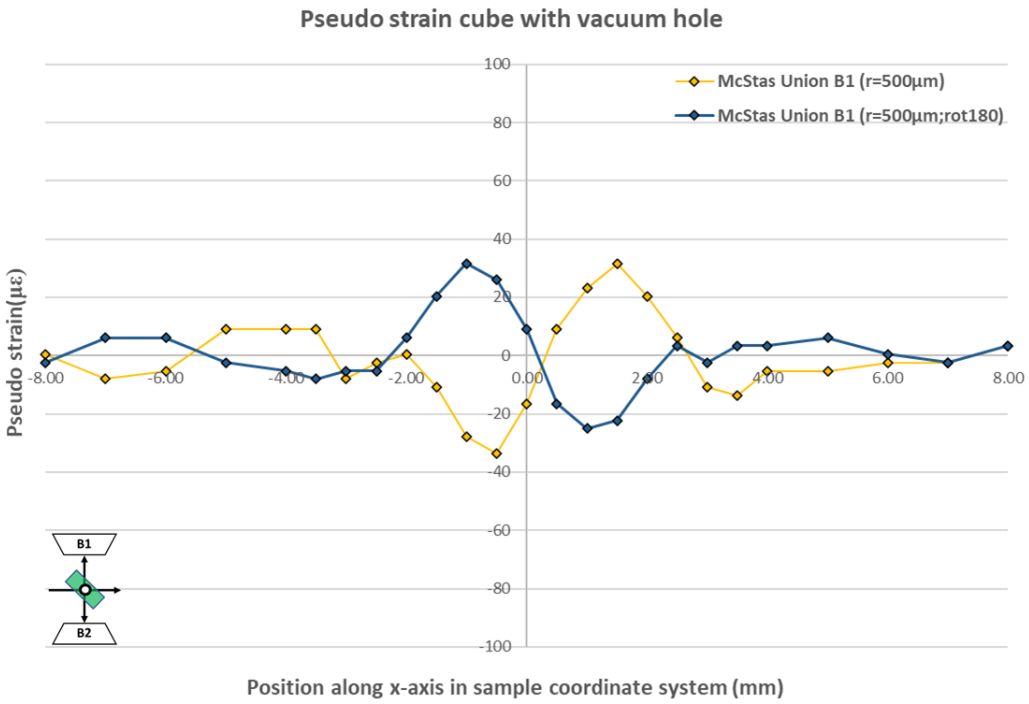

Figure 6.8: Pseudo strain results bank 1 for a nickel powder cube (8x8xx80) and a vacuum hole with a radius of 500µm in the centre using a 4mm GV and when the sample is rotated 180°. The pseudo strain for the non-rotated sample is negative between -2mm and 0.5mm reaching a minimum of ~40µε at -0.5mm and is positive between 0.5mm and 2.5mm reaching a maximum of 35µε at 1.5mm. The sample rotated 180° has positive pseudo strain between -2mm and 0.5mm reaching a maximum of 35µε at -1.mm, and negative pseudo strain between 0.5mmm and 2.5mm reaching a minimum of -25µε at 1mm.

The pseudo strain bank 1 and bank 2 for a sample consisting of a nickel powder cube (8x8xx80) containing a vacuum hole with a radius of 500µm off-centre(1.5mm) using a 4mm GV, and with the sample 180° rotated is shown in Figure 6.9. For sample positions less than -0.5mm the pseudo strain is of the same order of magnitude as the fitting error and can be ignored, similar for sample positions larger than 3mm. The pseudo strain bank 1 for the non-rotated sample is positive between -0.5 and 3mm reaching a maximum of ~40µε at 1.5mm. The sample rotated 180° has negative pseudo strain values for bank 1 between 0.5 and 3mm reaching a minimum of -40µε at 1.5mm. The pseudo strain bank 2 for the non-rotated sample is positive between -0.5 and 4mm reaching a maximum of ~55µε at 1mm. The sample rotated 180° has negative pseudo strain values for bank 2 between -0.5 and 4mm reaching a minimum of -20µε at 0mm.

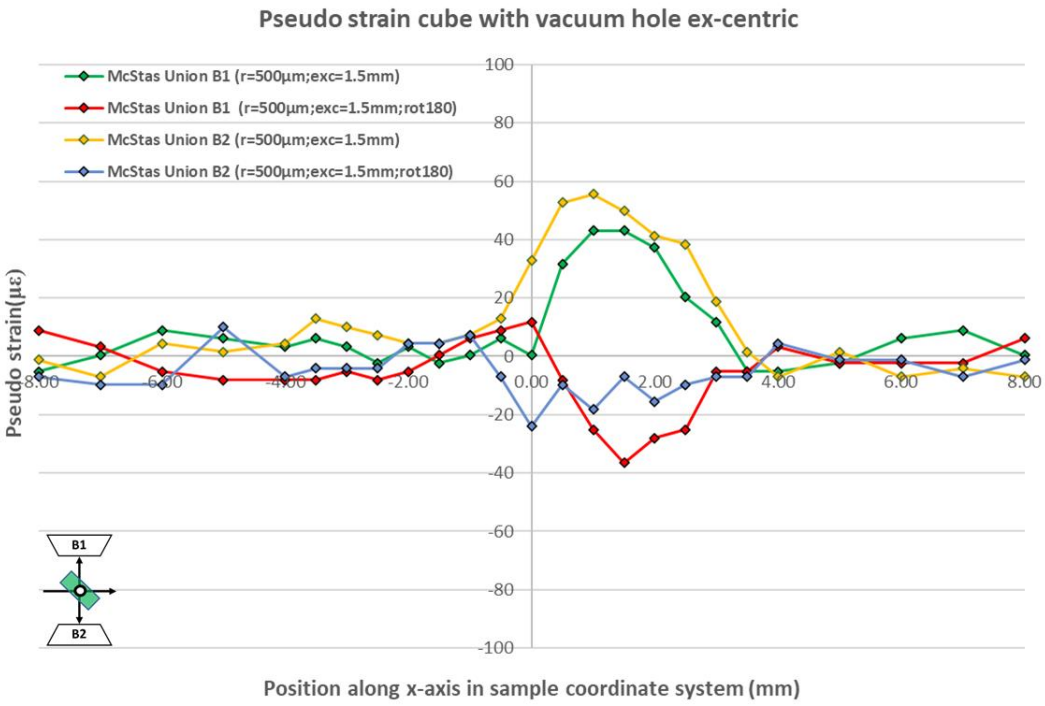

Figure 6.9; Pseudo strain results bank 1 and bank 2 for a nickel powder cube (8x8xx80) containing a vacuum hole off-centre(1.5mm) with a radius of 500µm using a 4mm GV and when the sample is rotated 180°. The pseudo strain bank 1 for the non-rotated sample is positive between -0.5 and 3mm reaching a maximum of ~40µε at 1.5mm. The sample rotated 180° has negative pseudo strain values for bank 1 between 0.5 and 3mm reaching a minimum of -40µε at 1.5mm. The pseudo strain bank 2 for the non-rotated sample is positive between -0.5 and 4mm reaching a maximum of ~55µε at 1mm. The sample rotated 180° has negative pseudo strain values for bank 2 between -0.5 and 4mm reaching a minimum of -20µε at 0mm.

6.4 Discussions

When looking at the results for the hole in the centre of the cube one observation is that the pseudo strain is negative when the hole is at one side of the GV and positive on the other. The off-centre hole shows only a positive pseudo strain on one side of the GV. The difference can be attributed to the symmetry in the case of the hole in the centre. The results show also that a hole in a cube can have a significant effect on the pseudo strain. The size of this effect depends on the ratio of the area of the hole and the area of the gauge volume. This relation can be visualised by plotting for each gauge volume the difference between the minimum and maximum pseudo strain versus the ratio of area hole and area gauge volume as shown in Figure 6.10. Each line in this diagram corresponds with a gauge volume. If the hole presents a grain of similar size then this plot could be used when performing neutron strain measurements of welds to assess the possible impact of the grain size on the pseudo strain for a given gauge volume. For a given GV and ratio the plot provides an indication of the possible effect on the pseudo strain, so for GV of 4mm grains that have a ratio exceeding 5% could generate a pseudo strain effect between 20µε and 90µε.

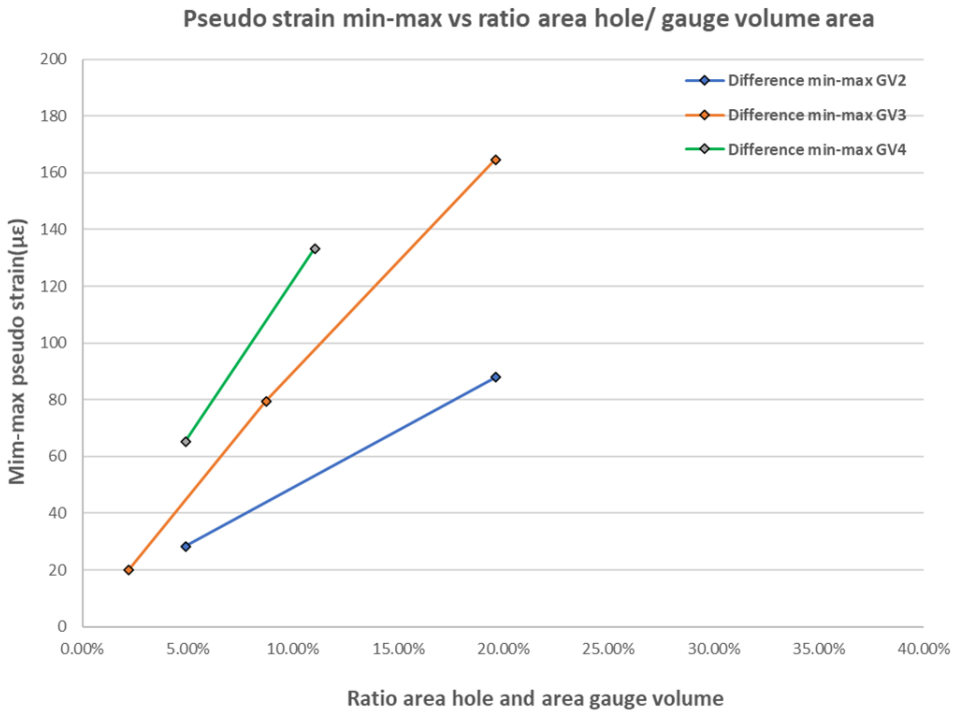

Figure 6.10: Minimum and maximum pseudo strain as a function of the ratio area hole / area gauge volume. This plot could be used to determine for a given neutron diffraction strain measurement what the impact of grains maybe if their size relative to the gauge volume is exceeding a certain value. If a 4mm GV is used then grains that have a ratio exceeding 5% could generate a pseudo strain effect between 20με and 90με.

The comparison between a vacuum hole in the centre of the cube and an Al wire indicates that for modelling purposes using a vacuum to fill the hole is acceptable. This was expected as aluminium has small scattering and absorption cross sections which mean that most neutrons will pass through the wire without interacting with Al nuclei. For a vacuum hole in the centre the pseudo strain is negative for one side of the GV and positive for the other. Rotating the sample 180^{o} the opposite happens. The total strain for bank 1 has been plotted in Figure 6.11.

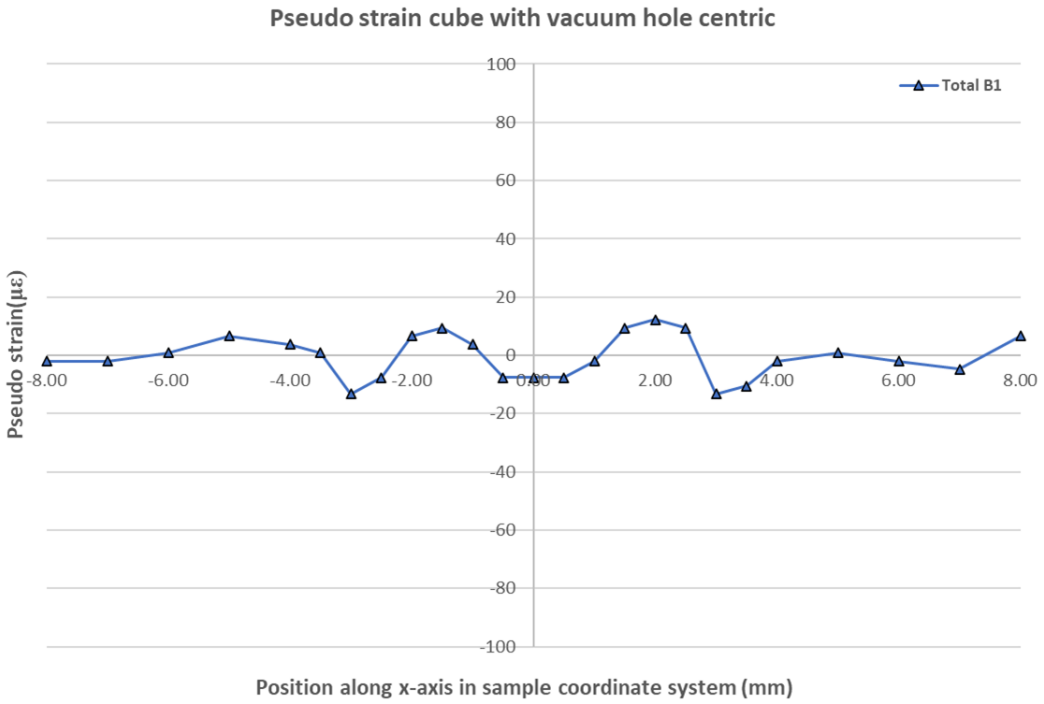

Figure 6.11: The total pseudo strain bank 1 for a nickel powder cube(8x8x80mm)) containing a vacuum hole with a radius of 500μm in the centre using a 4mm GV. The pseudo strains for the two orientations cancel each other out for bank 1 taking the size of the fitting error of ~6-8με into account.

The pseudo strains for the two orientations cancel each other out for bank 1 taking the size of the fitting error of ~6-8με into account. This is caused by the symmetry of the sample. For an off centre(1.5mm) hole the total strain for both banks is plotted in Figure 6.12. The pseudo strain of the two different sample orientations in this case do not entirely cancel out with a residual of ~20με for bank 1 between -0.5 and 1mm and ~20-40με for bank 2 between 0 and 3mm. By putting the hole off-centre the centre of gravity of the neutrons in the GV moves away from the geometric centre of the GV resulting in a pseudo strain, when rotating the sample 180^{o} the same happens with the NCOG now moving away in the opposite direction from the geometric centre of the GV. The neutron path lengths for the same scan point is not the same resulting in a residual pseudo strain when totalling the pseudo strain for both orientations.

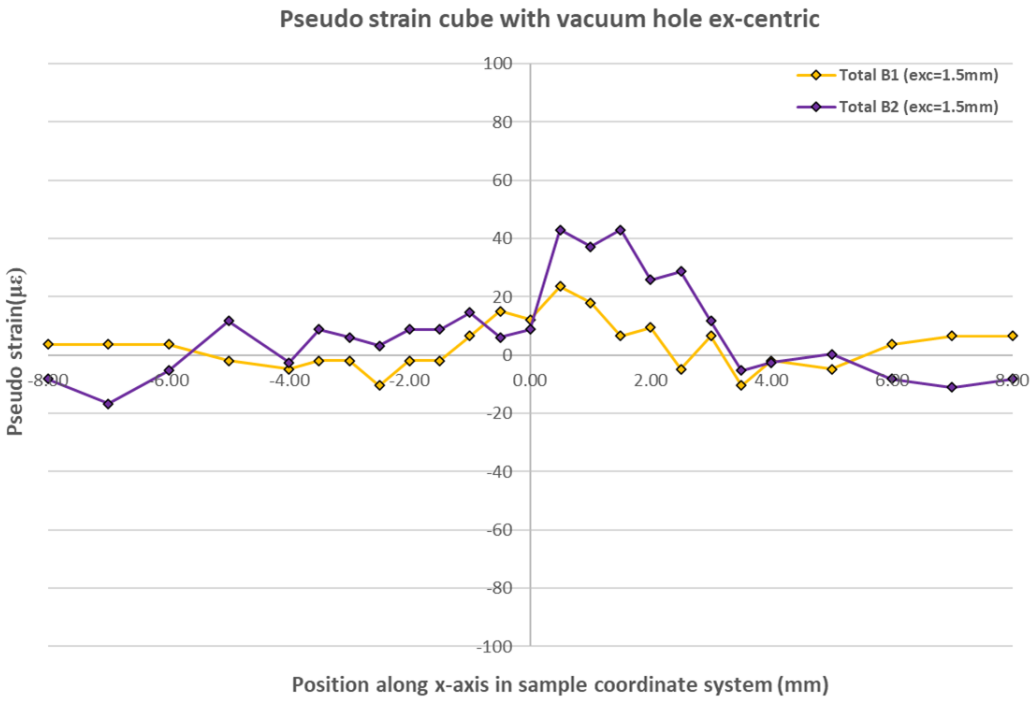

Figure 6.12: The total pseudo strain for bank 1 and bank 2 for a nickel powder cube containing a vacuum hole off-centre(1.5mm) using a 4mm GV. The pseudo strain of the two different sample orientations do not entirely cancel out with a residual of ~20με for bank 1 between -0.5 and 1mm and ~20-40με for bank 2 between 0 and 3mm .

So if you have a material with a hole in, and you make a d0 out of it, measuring the d0 and the stressed region at different orientations (ie 0 or 180 degree rotation) would cause an error. Hence in materials with potential voids, that or greater than 2% of GV you need to make sure the d0 is obtained from the same material and measured in exactly the same orientation.

6.5 Conclusions

The virtual experiments to study the effect of pores or voids as present in welds on strain show that McStas can be used to model these effects and provide a quantitative evaluation of the magnitude of the strain and the following conclusions can be made:

- The experiments in this chapter investigate the effect of a hole, smaller than the gauge volume on the measured strain
- The effect of hole size on the magnitude pseudo strain when a hole is present is investigated. The pseudo strain becomes large enough to be detected when the ratio of the size of the hole and the gauge volume used is larger than 2 %.
- The pseudo strain generated when using holes of various diameters and gauge volumes provide an indication of the possible effect on pseudo strain when the holes are replaced with grains of similar size as occur in a real weld. Translating across the pseudo strain effect of a hole to a grain suggest that an individual grain within the vicinity of the weld can generate a

significant pseudo strain if the ratio of the grain size and the gauge volume is larger than 2%. This means that when measuring strain in welds using neutron diffraction this effect should be taken into account when looking at the strain measured. One pragmatic approach could be to increase the error bars of results based on the amount of pseudo strain experienced with the gauge volume used and the reasonable maximum defect size predicted.

- Scanning the sample twice with the sample rotated 180^{o} in the second scan and adding up the resulting pseudo strains averages out the pseudo strain if the hole is in the centre of the sample for bank 1. For an off-centre hole this is not the case leaving a residual pseudo strain for both banks.
- In the simulation the hole was vacuum while in the real experiment the hole was filled with an aluminium wire. A simulation using an aluminium wire showed that it is acceptable to use a vacuum hole.

7 Discussion

The overarching long term aim of this project was to improve the characterisation of welded components present in a nuclear plant using neutron diffraction. Welds can have many kinds of imperfections that can impact the use of neutron diffraction. Firstly, there is normally some kind of material boundary formed as a result of the join. There may also be groups of large grains or even holes. All these features when present in the diffracting gauge volume of a beam line like ENGINX give rise to a nonuniformly filled gauge volume. Here the use of a neutron diffraction simulation tool, McStas is proposed and evaluated for predicting the error or “pseudo strains” that can occur because of the above features. To achieve this, firstly a new model was created and then several idealised scenarios were simulated and compared with real ENGINX measurements.

The new instrument model built for ENGINX in McStas using architectural drawings replacing the existing McStas model from 2006 has been tested. The reasons for building a new model from scratch were: The 2006 model did not have the correct beam profile due to parts of the guide system missing or unsatisfactorily simplified and inappropriate settings of the moderator and beam focussing window. This led to discrepancies between the results from the steel pin scan done on ENGINX and the data from the equivalent virtual experiment using McStas. Despite the new instrument model there is still some difference between the experiment and the virtual experiment although a close fit has been achieved. Several scenarios focussing at the settings of slit3 in terms of opening and position have been simulated to study how the pseudo strain is impacted when changing the beam. This has not led to any conclusive evidence for a particular root cause. Because the steel pin size is very small compared with other samples it is more sensitive to any beam deficiencies and as result may

exacerbate the differences found. The new instrument model, the new shell script to run the simulation and the modifications made to the data analysis software OpenGenie makes it possible to run much more realistic simulations of which the grid scan of the steel pin is a first example. It was therefore deemed reasonable to progress with the new instrument and perform subsequent virtual experiments to study pseudo strain occurring in air-to-material, material to material and due to pores in the vicinity of welds.

The virtual experiment simulating an iron powder cube traversing a beam provided the first opportunity to validate if McStas can be used to obtain quantitative information on pseudo strain and intensity. It also enabled the validation of some of the mitigation techniques used. A subset of the results of the simulations were compared with equivalent experiments on ENGINX. This showed a good match for bank 2 in reflection mode across all sample positions, while for bank 1 in transmission there was some deviation on a number of sample positions. The mitigation technique whereby the sample is rotated 180^{o} and the diffraction data summed does work for a bank in transmission mode but not in reflection mode with some residual pseudo strain present. Although the sample positions where this happens most strongly, those positions farthest away from the centre of the GV, may not always be relevant it is important that users performing measurements are aware of this. This issue becomes more important when materials are used with high attenuation. The simulations also demonstrate the importance of having the correct dimensions of the sample and the physical properties of the material. The simulations done with different densities highlight the impact this has on the intensity profile and the pseudo strain. The data obtained from the steel pin grid simulation were used to illustrate the shift of the NCOG versus the geometric centre and how this impacts the pseudo strain depending on whether the bank is in transmission or reflection mode.

The results of the virtual experiments designed to measure pseudo strain occurring in air-to-material and material-to-material interfaces show that McStas can provide useful quantitative data both for the intensity and the pseudo strain. McStas offers two options to simulate these type of sample models, one using the PowderN component type, and one using the union concept with the Union_box component type. By using the same material for both interface components it was proven that the PowderN gives incorrect results and that for interface type scans the union concept needs to be used. This has been done for the remainder of the simulations described in this dissertation.

Using the union concept and two different materials the air-to-material and material-to-material virtual experiments were performed. A subset of the simulation results were compared with equivalent experiments performed with ENGINX and show a good match, taking into account the exact physical properties of the material used in the experiment were not known with likely overstating or

understating the density and cross sections. The challenge with the peak fitting for a material-to-material interface due to overlapping peaks was overcome by using the intensities of the air-to-material intensity profiles for the same sample positions as a weighting for each material in the multi-phase fitting procedure of OpenGenie. The pseudo strain of the simulation showed a good match with the experimental data. This method for peak fitting when there is more than one material present looks promising but needs further testing for its robustness as well as with materials representative for welds.

In the final virtual experiment a cube was used with a cylindrical hole in it. To investigate the effect of a hole on the pseudo strain a number of scenarios were simulated with the hole in the centre of the cube whereby different diameters of the hole and GV dimensions were used. This showed that if the ratio of the hole area vs the GV area exceeds 2% a noticeable pseudo strain occurs. The data from these simulations were used to make a plot that shows the difference between the minimum pseudo strain and maximum pseudo strain arising dependent on the ratio. One way to use this information for real experiments is to adjust error bars. The simulation showed further that the pseudo strains are negative on one side of the GV and positive on the other. This can be explained in terms of the NCOG moving towards or away from the cylindrical hole as a function of the sample position. The simulations were repeated with the cube 180^{o} rotated and show that the pseudo strains average out. To investigate this further a simulation was performed in which the hole was put off-centre (1.5mm) using a hole diameter of 1mm and a 4mm GV. The results showed that there was no noticeable pseudo strain on one side of the GV but a significant one on the other. The simulation was repeated with the sample rotated 180^{o}. This showed no noticeable pseudo strain on the same side of the GV as before but a significant one on the other but with opposite sign. The pseudo strain does not average out using this approach and users performing experiments to measure strain should be aware of this.

The results of these experiments show that McStas is a useful way of simulating pseudo strain. However, there is a long way to go before and “correction” could be made to actual measurements and it must be emphasised that the simulations were all carried out on the HPC of ISIS and would not have been possible to run them in practical manner timewise on a PC. If a welded plate is measured that contains a boundary and some pores, the model created in this dissertation could reliably inform the user of the regions which are affected by pseudo strains, and the magnitude this error might be and at best inform the use of more appropriate error bars. At present, the ideal outcome of this work would be a better informed user base on the effect metallurgical and structural irregularities could have on results.

8 Conclusion

The objective of the research presented in this dissertation is to demonstrate that virtual experiments using McStas can be used to study pseudo strain and provide quantitative information that can be used to assist with preparation of experiments on real instruments reducing potential beam time lost as a result of making bad decision. Before virtual experiments can be designed and simulated to study pseudo strain it is necessary to build a virtual model of the instrument and to validate that the beam and the gauge volume characteristics are in line with the equivalent real instrument. If a model already exists, as was the case with ENGINX, it is strongly recommended that this validation is also done and corrections made if needed as was the case in this project.

Building a correct virtual model of the instrument in McStas is only one aspect needed to be able to run virtual experiments. The virtual experiments described in this dissertation involve many simulations with large numbers of parameters that vary. McStas provides a standard scan facility to perform these simulations but has severe limitations in that it can do only 1-dimensional scans, the scan step size is fixed and the number of neutrons simulated is for all scan points the same. Running different combinations of instrument settings can lead to the need for new copies of the original instrument with slight modifications such as swapping a collimator. To avoid this, a data driven approach has been coded and implemented where possible into the McStas code. Examples include code added to the instrument to replicate the traverse on ENGINX and a new shell script has been written that can read a script file similar to the real ENGINX instrument but has the capability to process extra parameters to enable a range of different simulations to be run in one go. The shell script can be used on a PC running Linux as well as on an HPC. The simulations done as part of this research project are extremely computing intensive and could not have been done on a PC. Similarly, OpenGenie the software used to do the peak fitting has been modified to allow data generated with McStas to be processed in the same fashion as data generated with ENGINX. All these changes have also a significant positive impact on the efficiency of running the simulations and analysing the output. This leads to the first major output from the project:-

> *A validated model of ENGINX that is capable of modelling intensity and lattice parameters changes resulting from non-uniform gauge volume filling*

In the subsequent phase of the project the emphasis shifted to modelling samples in McStas using the model mentioned above. The first sample modelled was an iron powder cube in an aluminium hull. This sample was built using the PowderN component type in McStas and used to validate McStas can

be used for making quantitative predictions of the pseudo strain arising in a air to material interface scan. The results of the simulations done with this sample show that:-

> *McStas can be used to measure pseudo strain as was proven by comparing the simulation results with the data from equivalent experiment done on ENGINX.*

Further simulations done with the cube illustrate how the geometry of the experiment and the attenuation of the material greatly impact the pseudo strain modelled highlighting the importance of accurately representing any sample in McStas and not compromising with standard material definitions. A further important finding shows that:-

> *The mitigation technique in which the sample is scanned twice with omega rotated by 180^o in the second scan works in transmission mode but not for reflection mode on ENGINX.*

The material-to-material interface experiments using two cubes made of the same material showed that using the `PowderN` component type to model the cubes gives incorrect pseudo strain values. To mitigate this problem the sample was modelled again using the union concept and `Union_box` component type. The simulations using this model gave the correct pseudo strain values. So a significant finding is that:-

> *In samples with more than one material or component being illuminated at one time the union concept with the Union_box component type must be used.*

The material-to-material interface experiment was repeated using a different material for each cube. The simulations covered air-to-material, material-to-air and material-to-material. The results from a subset of these simulations were compared against data from equivalent experiments performed on ENGINX which showed a largely good match in terms of shape but a general underestimation by McStas in terms of magnitude. To perform the fitting of the material-to-material interface data generated with McStas, the intensities of the same sample positions of the air-to-material interface scans were used as scaling factors in the multi-phase procedure of OpenGenie. The results were then compared against those from a real experiment on ENGIN-X and showed to a large extend a match.

In the final virtual experiment a powder cube containing a cylindrical hole was used. The purpose of this experiment was to study the effect of a pore or welding defect on pseudo strain. Various simulations were performed using different hole diameters, gauge volumes and position of the hole to determine the ratio of the hole vs gauge volume at which a noticeable pseudo strain appears. The results from these simulations indicate that:-

When this ratio or hole to gauge volume size is larger than 2% the pseudo strain becomes significant and should be considered.

A subset of the simulated results was compared against the data from an equivalent experiment on ENGINX and confirmed the appearance of a pseudo strain when the ratio is above 2%. In analogy to the material-to-air interface experiment the simulations were repeated with the sample rotated 180^{o}. When the hole is in the centre of the cube the pseudo strains average out, but when the hole is placed off-centre this is no longer the case. The conclusion of this last experiment is that users need to be aware of this when doing real experiments and take it into account when interpreting their results. One pragmatic approach could be to increase the error bars of results based on the amount of pseudo strain experienced with the gauge volume used and the reasonable maximum defect size predicted.

The virtual experiments performed as part of this research project and the results from them provides ample evidence that McStas and the Monte Carlo method embedded in it can be used to study pseudo strain. The results confirm and support the findings on pseudo strain obtained by other methods. The data generated with McStas particularly the intensity data could be used to assist with the fitting of diffraction patterns with overlapping peaks. The advantage of using McStas comes from being able to run virtual experiments using a wide range of scenarios and parameter settings were users most likely would not get beam time allocated for. These 'what-if' type scenarios could be used prior to doing a real experiment as it may provide useful information on how best to run the experiment and get the best out of the beam time allocated. The sample models designed in this research project will not only work for ENGINX but can be used in other instruments as well provided an instrument model exists in McStas.

The code developed and used in this thesis will be made available on Github site, url to be confirmed.

9 Further work

9.1 Interface materials

The virtual sample model used to study interfaces can be used with other materials and a natural next phase would be to use materials that are widely used in the nuclear and general engineering community like INCONEL718 and SS304. The challenge here is to identify ways that can be used to perform peak fitting when the lattice parameters of both materials are very close in magnitude resulting in overlapping peaks. In McStas it is possible to isolate neutrons scattered dependent on the sample component they are scattered from. By running two scans were both materials are present but only the neutrons of one of them reach the detector one can separate out the contribution of each material to the pseudo strain at the interface. For a real experiment this separation cannot be done but the McStas results may provide an insight in the pseudo strains occurring in the real experiment.

9.2 Poly crystalline samples

To simulate a polycrystalline sample, code has been developed in McStas (Alberto Cereser Thesis DTU Copenhagen) which uses the single crystal component and the powder component together. The powder component acts in this case as a container in which single crystal components are placed. The single crystals can be grouped together to represent a grain with a specific orientation. The grouping and orientations are passed on to McStas as two separate files. To generate these files one can either write code using Voronoi libraries or use Dream3D[84] software. In Dream3D samples can be created from EBSD files or entirely synthetic by specifying crystal structure and other physical properties and applying statistics to generate orientations and groupings of voxels to represent grains. Utilities have been written to export the material information like grain shape and orientation from Dream3D and convert this into a format that can be used directly in McStas. This capability would be needed to perform a more realistic simulation of what happens in real welds of different materials.

9.3 Preparing experiments and predicting pseudo strains

When users have been allocated beamtime on ENGIN-X they will prepare their samples and proposed experiments without the opportunity to verify it will work when doing the real experiment. The simulation techniques developed in this research project could be used by the users of ENGIN-X to run simulations of their experiments ahead of the real experiment. This could highlight any issues with the experiment envisaged and prevent losing beamtime when running the real experiment. In addition the simulation could be used to vary parameters like gauge volume, instrument settings, choice of

material(s) and geometry to perform what if scenarios which with the real instrument would require more beamtime which is expensive and often not available. The simulations in this research project were done on a High Performance Computer cluster requiring knowledge of computers that not all users have. This could be mitigated by porting the software code to a PC running a Linux operating system using GPU processors that are able to perform the required number of calculations in a practical timeframe.

10 References

[1] "Electricity generated with nuclear power in UK." [Online]. Available: https://www.world-nuclear.org/information-library/country-profiles/countries-t-z/united-kingdom.aspx.

[2] "UK National Energy and Climate Plan (NECP) 2019." [Online]. Available: https://www.gov.uk/government/publications/uk-national-energy-and-climate-plan-necp.

[3] "Contracts for the Hinkley Point C." [Online]. Available: https://www.gov.uk/government/collections/hinkley-point-c.

[4] G. Sengler, F. Forêt, G. Schlosser, R. Lisdat, and S. Stelletta, "EPR core design," *Nucl. Eng. Des.*, vol. 187, no. 1, pp. 79–119, 1999.

[5] M. Fischer, "The severe accident mitigation concept and the design measures for core melt retention of the European Pressurized Reactor (EPR)," *Nucl. Eng. Des.*, vol. 230, no. 1–3, pp. 169–180, May 2004.

[6] M. Fischer, O. Herbst, and H. Schmidt, "Demonstration of the heat removing capabilities of the EPR core catcher," *Nucl. Eng. Des.*, vol. 235, no. 10, pp. 1189–1200, 2005.

[7] G. Locatelli, M. Mancini, and N. Todeschini, "Generation IV nuclear reactors: Current status and future prospects," *Energy Policy*, vol. 61, pp. 1503–1520, 2013.

[8] K. L. Murty and I. Charit, "Structural materials for Gen-IV nuclear reactors: Challenges and opportunities," *J. Nucl. Mater.*, vol. 383, no. 1, pp. 189–195, 2008.

[9] J. G. Marques, "Evolution of nuclear fission reactors: Third generation and beyond," *Energy Convers. Manag.*, vol. 51, no. 9, pp. 1774–1780, 2010.

[10] K. Lefmann and K. Nielsen, "McStas, a general software package for neutron ray-tracing simulations," *Neutron News*, vol. 10, no. 3, pp. 20–23, 2007.

[11] K. Lefmann *et al.*, "Virtual experiments: The ultimate aim of neutron ray-tracing simulations," *J. Neutron Res.*, vol. 16, no. 3–4, pp. 97–111, 2008.

[12] *T357 Structural Integrity: designing against failure*. Open University.

[13] P. J. Withers and H. K. D. H. Bhadeshia, "Residual stress. Part 1 – Measurement techniques," *Mater. Sci. Technol.*, vol. 17, no. 4, pp. 355–365, 2001.

[14] P. J. Withers and H. K. D. H. Bhadeshia, "Residual stress. Part 2 – Nature and origins," *Mater. Sci. Technol.*, vol. 17, no. 4, pp. 366–375, 2001.

[15] A. De and T. DebRoy, “A perspective on residual stresses in welding,” *Sci. Technol. Weld. Join.*, vol. 16, no. 3, pp. 204–208, 2011.

[16] A. Lambert-Perlade, A. F. Gourgues, and A. Pineau, “Austenite to bainite phase transformation in the heat-affected zone of a high strength low alloy steel,” *Acta Mater.*, vol. 52, no. 8, pp. 2337–2348, 2004.

[17] D. Deng, “FEM prediction of welding residual stress and distortion in carbon steel considering phase transformation effects,” *Mater. Des.*, vol. 30, no. 2, pp. 359–366, Feb. 2009.

[18] S. Fricke, E. Keim, and J. Schmidt, “Numerical weld modeling - A method for calculating weld-induced residual stresses,” *Nucl. Eng. Des.*, vol. 206, no. 2–3, pp. 139–150, 2001.

[19] B. Q. Chen, M. Hashemzadeh, Y. Garbatov, and C. Guedes Soares, “Numerical and parametric modeling and analysis of weld-induced residual stresses,” *Int. J. Mech. Mater. Des.*, vol. 11, no. 4, pp. 439–453, 2015.

[20] R. G. Thiessen, I. M. Richardson, and J. Sietsma, “Physically based modelling of phase transformations during welding of low-carbon steel,” *Mater. Sci. Eng. A*, vol. 427, no. 1–2, pp. 223–231, 2006.

[21] C. H. Lee and K. H. Chang, “Prediction of residual stresses in welds of similar and dissimilar steel weldments,” *J. Mater. Sci.*, vol. 42, no. 16, pp. 6607–6613, 2007.

[22] J. J. Daly, “Problems related to stress corrosion cracking reduced by controlled shot peening,” *Ind. Heat.*, vol. 65, no. 5, pp. 65–70, 1998.

[23] E. Macherauch and K. H. Kloss, “Proceedings of the International Conference on residual Stresses,” *Garmisch-Partenkirchen, FRG*, pp. 167–174, 1986.

[24] M. E. Fitzpatrick and A. Lodini, *Analysis of Residual Stress by Synchrotron Radiation*. 2003.

[25] N. S. Rossini, M. Dassisti, K. Y. Benyounis, and A. G. Olabi, “Methods of measuring residual stresses in components,” *Mater. Des.*, vol. 35, pp. 572–588, Mar. 2012.

[26] P. J. Webster, G. Mills, X. D. Wang, W. P. Kang, and T. M. Holden, “Neutron strain scanning of a small welded austenitic stainless steel plate,” *J. Strain Anal. Eng. Des.*, vol. 30, no. 1, pp. 35–43, 1995.

[27] T. Neeraj, T. Gnäupel-Herold, H. J. Prask, and R. Ayer, “Residual stresses in girth welds of carbon steel pipes: Neutron diffraction analysis,” *Sci. Technol. Weld. Join.*, vol. 16, no. 3, pp. 249–253, 2011.

[28] J. W. H. Price, A. Ziara-Paradowska, S. Joshi, T. Finlayson, C. Semetay, and H. Nied, “Comparison of experimental and theoretical residual stresses in welds: The issue of gauge volume,” *Int. J. Mech. Sci.*, vol. 50, no. 3, pp. 513–521, 2008.

[29] C. Huygens, *Traité de la lumière: où sont expliquées les causes de ce qui luy arrive dans la reflexion, & dans la refraction, et particulierement dans l’etrange refraction du cistal d’Islande*. A Leide: chez Pierre vander Aa ..., 1690.

[30] A. Smith, “Ouevres completes Fresnel,” *Oxford Univ.*, vol. XXX, p. 60, 1986.

[31] T. Q. Postulate and R. Development, “580 Supplement to ‘ Nature,’ April 14, 1928 The Quantum Postulate and the Recent Development of Atomic Theory. 1,” pp. 580–590, 1928.

[32] “Lecture 20 : Scattering theory,” in *Bulletin of Materials Science*, vol. 21, no. 2, 1998, pp. 127–131.

[33] “ISIS - Neutron diffraction.” [Online]. Available: http://www.isis.stfc.ac.uk/instruments/neutron-diffraction2593.html.

[34] S. Ganguly, L. Edwards, and M. E. Fitzpatrick, “Problems in using a comb sample as a stress-free reference for the determination of welding residual stress by diffraction,” *Mater. Sci. Eng. A*, vol. 528, no. 3, pp. 1226–1232, Jan. 2011.

[35] Z. Feng, X.-L. Wang, W. Woo, Z. Feng, X.-L. Wang, and S. A. David, “Neutron diffraction measurements of residual stresses in friction stir welding: A review,” *Artic. Sci. Technol. Weld. Join.*, 2011.

[36] J. W. H. Price *et al.*, “Residual stress distribution in steel butt welds measured using neutron and synchrotron diffraction Residual stress distribution in steel butt welds measured using neutron and synchrotron diffraction Residual stress distribution in steel butt welds measured using neutron and synchrotron diffraction,” *Artic. J. Phys. Condens. Matter*, vol. 21, p. 8, 2009.

[37] S. R. Creek, J. R. Santisteban, and L. Edwards, “Modelling pseudo-strain effects induced in strain measurement using time-of-flight neutron diffraction,” Citeseer, 2005.

[38] J. D. Jorgensen *et al.*, “ELECTRONICALLY FOCUSED TIME-OF-FLIGHT POWDER DIFFRACTOMETERS AT THE INTENSE PULSED NEUTRON SOURCE,” *J. Appl. Crystallogr.*, vol. 22, pp. 321–333, 1989.

[39] H. M. M. Rietveld, “A profile refinement method for nuclear and magnetic structures,” *J. Appl. Crystallogr.*, vol. 2, no. 2, pp. 65–71, 1969.

[40] R. A. Young, *Rietveld Method, The*. Oxford: Oxford: Oxford University Press, 1995.

[41] R. A. Young and D. B. Wiles, "Application of the Rietveld Method for Structure Refinement with Powder Diffraction Data," *Adv. X-ray Anal.*, vol. 24, pp. 1–23, 1980.

[42] T. Pirling, G. Bruno, and P. J. Withers, "SALSA-A new instrument for strain imaging in engineering materials and components," *Mater. Sci. Eng. A*, vol. 437, no. 1, pp. 139–144, 2006.

[43] T. Pirling, "Precise analysis of near surface Neutron Strain Imaging measurements," *Procedia Eng.*, vol. 10, pp. 2147–2152, 2011.

[44] Michael T Hutchinson, *Introduction to the characterization of residual stress by neutron diffraction*. 2005.

[45] A. Kankanala, J. James, J. Bouchard, S. Northover, and M. Yescas, "Measurement of residual stresses in a dissimilar metal welded pipe." 2011.

[46] R. J. Moat *et al.*, "Residual stresses in inertia-friction-welded dissimilar high-strength steels," *Metall. Mater. Trans. A Phys. Metall. Mater. Sci.*, vol. 40, no. 9, pp. 2098–2108, 2009.

[47] J. A. Francis, H. K. D. H. Bhadeshia, and P. J. Withers, "Welding residual stresses in ferritic power plant steels," *Materials Science and Technology*, vol. 23, no. 9. pp. 1009–1020, 2007.

[48] T. I. Ramjaun *et al.*, "Surface residual stresses in multipass welds produced using low transformationtemperature filler alloys," *Sci. Technol. Weld. Join.*, vol. 19, no. 7, pp. 623–630, 2014.

[49] Y. Traoré, "Reliable Residual Stress Measurement by Neutron Diffraction," no. 1, pp. 21–23, 2014.

[50] M. Sireesha, V. Shankar, S. K. Albert, and S. Sundaresan, "Microstructural features of dissimilar welds between 316LN austenitic stainless steel and alloy 800," *Mater. Sci. Eng. A*, vol. 292, no. 1, pp. 74–82, 2000.

[51] M. K. Samal, M. Seidenfuss, E. Roos, and K. Balani, "Investigation of failure behavior of ferritic-austenitic type of dissimilar steel welded joints," *Eng. Fail. Anal.*, vol. 18, no. 3, pp. 999–1008, 2011.

[52] J. Cao, Y. Gong, K. Zhu, Z. G. Yang, X. M. Luo, and F. M. Gu, "Microstructure and mechanical properties of dissimilar materials joints between T92 martensitic and S304H austenitic steels," *Mater. Des.*, vol. 32, no. 5, pp. 2763–2770, 2011.

[53] H. T. Wang, G. Z. Wang, F. Z. Xuan, and S. T. Tu, “Fracture mechanism of a dissimilar metal welded joint in nuclear power plant,” *Eng. Fail. Anal.*, vol. 28, pp. 134–148, 2013.

[54] D. W. Rathod, P. K. Singh, S. Pandey, and S. Aravindan, “Effect of buffer-layered buttering on microstructure and mechanical properties of dissimilar metal weld joints for nuclear plant application,” *Mater. Sci. Eng. A*, vol. 666, pp. 100–113, 2016.

[55] D. J. Hughes, E. Koukovini-Platia, and E. L. Heeley, “Residual stress in a laser welded EUROFER blanket module assembly using non-destructive neutron diffraction techniques,” *Fusion Eng. Des.*, vol. 89, no. 2, pp. 104–108, 2014.

[56] A. Paradowska, T. R. Finlayson, J. W. H. Price, R. Ibrahim, A. Steuwer, and M. Ripley, “Investigation of reference samples for residual strain measurements in a welded specimen by neutron and synchrotron X-ray diffraction,” *Phys. B Condens. Matter*, vol. 385–386, pp. 904–907, 2006.

[57] V. Stelmukh, L. Edwards, J. R. Santisteban, S. Ganguly, and M. E. Fitzpatrick, “Weld Stress Mapping Using Neutron and Synchrotron X-Ray Diffraction,” *Mater. Sci. Forum*, vol. 404–407, pp. 599–604, Aug. 2002.

[58] D. George and P. J. Bouchard, “Measurement and Modelling of Residual Stresses in Thick Section Type 316 Stainless Steel Welds Residual stress on nuclear plant thick welds View project Improving the Accuracy of Elevated Temperature Design and Life Assessment Procedures. View project,” 2000.

[59] A. Steuwer, M. Dumont, M. Peel, M. Preuss, and P. J. Withers, “The variation of the unstrained lattice parameter in an AA7010 friction stir weld,” 2007.

[60] S. Spooner and X. L. Wang, “Diffraction peak displacement in residual stress samples due to partial burial of the sampling volume,” *J. Appl. Crystallogr.*, vol. 30, pp. 449–455, 1997.

[61] H. Suzuki, S. Harjo, J. Abe, P. Xu, K. Aizawa, and K. Akita, “Effects of gauge volume on pseudo-strain induced in strain measurement using time-of-flight neutron diffraction,” *Nucl. Instruments Methods Phys. Res. Sect. A Accel. Spectrometers, Detect. Assoc. Equip.*, vol. 715, pp. 28–38, 2013.

[62] D. Q. Wang, J. R. Santisteban, and L. Edwards, “Effect of wavelength-dependent attenuation on strain measurement using pulsed neutron diffraction,” *Nucl. Instruments Methods Phys. Res. Sect. A Accel. Spectrometers, Detect. Assoc. Equip.*, vol. 460, no. 2–3, pp. 381–390, 2001.

[63] Y. V. Taran and A. M. Balagurov, “Correction of a neutron diffraction peak shift due to a partial

immersion of a gauge volume in an unstressed sample," *Nucl. Instruments Methods Phys. Res. Sect. A Accel. Spectrometers, Detect. Assoc. Equip.*, vol. 679, pp. 19–24, 2012.

[64] P. Willendrup, E. Farhi, E. Knudsen, U. Filges, and K. Lefmann, "McStas: Past, present and future," *J. Neutron Res.*, vol. 17, no. 1, pp. 35–43, 2014.

[65] D. Wechsler, G. Zsigmond, F. Streffer, and F. Mezei, "VITESS: Virtual instrumentation tool for pulsed and continuous sources," *Neutron News*, vol. 11, no. 4, pp. 25–28, 2007.

[66] J. Y. Y. Lin *et al.*, "MCViNE - An object oriented Monte Carlo neutron ray tracing simulation package," *Nucl. Instruments Methods Phys. Res. Sect. A Accel. Spectrometers, Detect. Assoc. Equip.*, vol. 810, pp. 86–99, 2016.

[67] C. Andrieu, "Monte Carlo Methods for Absolute Beginners Motivation and Basic Principles of the Monte Carlo," *Mach. Learn.*, pp. 113–145, 2004.

[68] F. James, "Monte Carlo theory and practice," *Reports Prog. Phys.*, vol. 43, no. 9, p. 1145, 1980.

[69] J. H. Halton, "A retrospective and prospective survey of the Monte Carlo method," *SIAM Rev.*, vol. 12, no. 1, pp. 1–63, 2009.

[70] "McStas Component Manual." .

[71] G. Ehlers, A. A. Podlesnyak, J. L. Niedziela, E. B. Iverson, and P. E. Sokol, "The new Cold Neutron Chopper Spectrometer at the Spallation Neutron Source-Design and Performance," 2011.

[72] G. E. Granroth *et al.*, "SEQUOIA: A newly operating chopper spectrometer at the SNS," *J. Phys. Conf. Ser.*, vol. 251, no. 1, 2010.

[73] S. Jaksch *et al.*, "Concept for a Time---of---Flight Small Angle Neutron Scattering Instrument at the European Spallation Source."

[74] J. A. Rodriguez *et al.*, "MACS - A new high intensity cold neutron spectrometer at NIST," *Meas. Sci. Technol.*, vol. 19, no. 3, pp. 1–7, 2008.

[75] L. C. Chapon *et al.*, "Neutron News Wish: The New Powder and Single Crystal Magnetic Diffractometer on the Second Target Station," vol. 22, no. 2, pp. 22–25, 2011.

[76] K. Kanaki *et al.*, "Simulation tools for detector and instrument design," *Phys. B Condens. Matter*, vol. 551, no. August 2017, pp. 386–389, 2018.

[77] A. Moriai *et al.*, "Development of engineering diffractometer at J-PARC," *Phys. B Condens. Matter*, vol. 385–386, pp. 1043–1045, 2006.

[78] W. Kockelmann *et al.*, “Status of the Neutron Imaging and Diffraction Instrument IMAT,” in *Physics Procedia*, 2015.

[79] L. Udby *et al.*, “Analysing neutron scattering data using McStas virtual experiments,” *Nucl. Instruments Methods Phys. Res. Sect. A Accel. Spectrometers, Detect. Assoc. Equip.*, vol. 634, no. 1, Supplement, pp. S138–S143, 2011.

[80] S. Torii and A. Moriai, “The design of the radial collimator for residual stress analysis diffractometer of J-PARC,” *Phys. B Condens. Matter*, vol. 385–386, pp. 1287–1289, 2006.

[81] J. R. Taylor, “The Chi-Squared Test for a Distribution,” *An Introduction To Error Analysis: The Study of Uncertainties in Physical Measurements*. pp. 261–278, 1997.

[82] E. Farhi, T. Hansen, A. Wildes, R. Ghosh, and K. Lefmann, “Designing new guides and instruments using McStas,” *Appl. Phys. A Mater. Sci. Process.*, vol. 74, no. SUPPL.II, pp. 1471–1473, 2002.

[83] T. M. Holden, Y. Traore, J. James, J. Kelleher, and P. J. Bouchard, “Determination and mitigation of the uncertainty of neutron diffraction measurements of residual strain in large-grained polycrystalline material,” *J. Appl. Crystallogr.*, vol. 48, no. 2, pp. 582–584, 2015.

[84] M. Groeber A. and M. Jackson A., “DREAM.3D: A Digital Representation Environment for the Analysis of Microstructure in 3D,” *Integr. Mater. Manuf. Innov.*, vol. 3, no. 1, p. 5, 2014.